UCRL-53452
Distribution Category UC-4

UCRL--53452

DE84 008871

A Fully Automated Radiochemical Preparation System for Gamma-Spectroscopy on Fission Products and the Study of the Intruder and Vibrational Levels in ^{83}Se

Oliver Gordon Lien, III

(Ph.D. Thesis)

Manuscript date: October 1983

LAWRENCE LIVERMORE NATIONAL LABORATORY
University of California • Livermore, California • 94550

Available from: National Technical Information Service • U.S. Department of Commerce
5285 Port Royal Road • Springfield, VA 22161 • $11.50 per copy • (Microfiche $4.50)

A Fully Automated Radiochemical Preparation System for Gamma-Spectroscopy on Fission Products and the Study of the Intruder and Vibrational Levels in ^{83}Se

By

Oliver Gordon Lien, III
BA (San Jose State University) 1970
BS (San Jose State University) 1976
MS (University of California, Davis) 1978

DISSERTATION

Submitted in partial satisfaction of the requirements for the degree of

DOCTOR OF PHILOSOPHY

in

Engineering – Applied Science

in the

GRADUATE DIVISION

of the

UNIVERSITY OF CALIFORNIA

DAVIS

Approved:

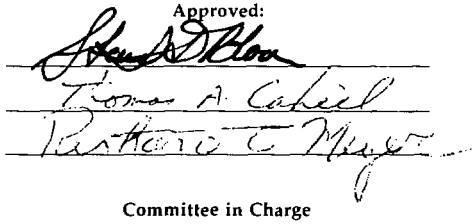

Committee in Charge

Deposited in the University Library _____
Date *Librarian*

Table of Contents

List of Figures

List of Tables

A Fully Automated Radiochemical Preparation System for Gamma-Spectroscopy on Fission Products and the Study of the Intruder and Vibrational Levels in ^{83}Se

Abstract

AUTOBATCH was developed to provide a usable source of short-lived neutron-rich nuclides through chemical preparation of the sample from fission products for detailed gamma-ray spectroscopy, which would complement the output of on-line isotope separators. With AUTOBATCH the gamma rays following the β^- decay of $^{83}_{33}As_{50}$ were studied to determine:

- the ground state spin and parity of ^{83}As to be $5/2^-$;
- the absolute intensity of the β^- branch from ^{83}As to $^{83}Se^m$ to be 0.3%;
- the absolute intensity of the ground state β^- branch from $^{83}Se^m$ to ^{83}Br to be 39%;
- the halflife of the $5/2_1^+$ level to be 3.2 ns;
- the structure of $^{83}_{34}Se_{49}$.

The results are used to show that the intruder structure which had been previously observed in the odd mass $_{49}In$ isotopes could be observed in the N=49 isotones. The observed structure is discussed in terms of the unified model calculations of Heyde which has been used to describe the intruder structure in the indium nuclei. The intruder structure is most strongly developed, not at core mid-shell, $^{89}_{40}Zr_{49}$, but rather at core mid-sub-shell ^{83}Se. This difference is qualitatively understood to be due to the blocking of collectivity by the Z=40 subshell closure which prevents the intruder structure from occurring in $^{87}Sr_{49}$ and $^{89}Zr_{49}$.

I. Introduction

The only available source for neutron-rich nuclides from $_{31}Ga$ to $_{71}Dy$ is the fission process. Lighter neutron-rich nuclides can be produced through spallation (GUS81) and fragmentation (SYM81). I designed and built AUTOBATCH to provide a usable source of the nuclides through chemical preparation of the sample from fission products for detailed gamma-ray spectroscopy.

I also used AUTOBATCH to perform detailed studies of $^{83}Se_{49}$. The structure in this nucleus was expected to be similar to the intruder structure seen in $^{113-121}_{49}In$. I used the unified model calculations of Heyde (HEY78, HEY80), which describe the indium nuclei, to describe the N=49 isotones with particular attention to ^{83}Se.

This thesis readily separates into three major sections. Chapter II, AUTOBATCH, describes the concept and design of the computer controlled nuclear-chemical sample preparation facility. In chapters III and IV, the experimental measurements and the development of the decay scheme

for ^{83}As are described. In chapters V, VI, and VII I discuss the results obtained for ^{83}Se and the N=49 isotones in light of the unified model developed by K. Heyde (HEY78, HEY80) and the results for the indium nuclei.

II. AUTOBATCH: The LLNL Fast Chemistry System

One of the few sources of neutron-rich, far-from-stability nuclei with atomic numbers (Z) between 32 and 60 and with mass numbers (A) between 80 and 160 is the fission process. To study any one of these nuclides, techniques must be devised that provide the best possible isolation of that nuclide from all other fission products. Radiochemical techniques offered the first widely used means of isolating nuclides in this neutron-rich region and, as interest shifted to nuclei progressively farther from stability with progressively shorter half-lives, faster chemical techniques were developed. Isotope separation techniques also were developed to provide an even faster isolation of many fission products. However, for a number of elements, the isotope separator gives an unusably low yield due to ion source problems (Fig. II.1) and rapid radiochemical separation is the only means of isolating these elements for study.

Basically there are two methods that can be used to chemically isolate a radioactive sample, batch and continuous. Batch systems irradiate, purify and then count a discrete sample, while continuous systems irradiate, purify and count incremental quantities of sample. This difference gives each system definite advantages and limitations. The advantages of a batch method are significant. Most important is the fact that data from a batch processor can be manipulated to retain half-life dependent information, which is more difficult with the equilibrium sample produced by a continuous separation process. The time dependence of the gamma activity due to the decay of nuclides A and B in the following sequence of decays

$$A \xrightarrow{\beta} B \xrightarrow{\beta} C \qquad \text{(II.1)}$$

is significantly different in batch separation. Further, if there are several "A" components, their signatures will be half-life dependent. By breaking the data acquisition period on a batch processor into discrete time periods and accumulating data in each time period (multichannel-multiscaling), it is easy to distinguish between the various components of the sample activity (short-lived, long-lived, daughter products). Acquiring sequential spectra further enhances the quality of the data for a short-lived isotope by placing most of these desired counts into the first time spectra and most of the counts from long-lived and daughter products into the later time spectra. Furthermore, the useful chemical separation reactions suitable for a batch processor, particularly those in aqueous solution, are much better known than those required for a continuous separation.

The major advantage of a continuous chemistry is that it offers shorter separation times through the use of instream chemistry. Continuous chemistry systems have been used for half-lives down to 0.4 s (MAS80, ZEN78), while batch chemistries have been used for half-lives as short as 0.8 s.

A secondary advantage of a continuous separation is that data can be acquired at a maximum rate at all times. Because a batch system processes discrete sample quantities, data cannot be acquired while the sample is being separated and the activity decreases as the sample decays while data is being accumulated; thus data can be acquired at the maximum rate only at the beginning of the acquisition period. I will compare the gross average count rates for these two systems. I will equate decay rate and count rate to make the analysis as general as possible.

To compare average count rate obtained from each system as a function of the half-life of the sample, I use a simple model based on the Bateman equations (FRI65) to determine the half-lives and recycle times for which a batch chemistry system would be competitive with a continuous chemistry system. Here, the pertinent factor is the overall average decay rate obtained with each

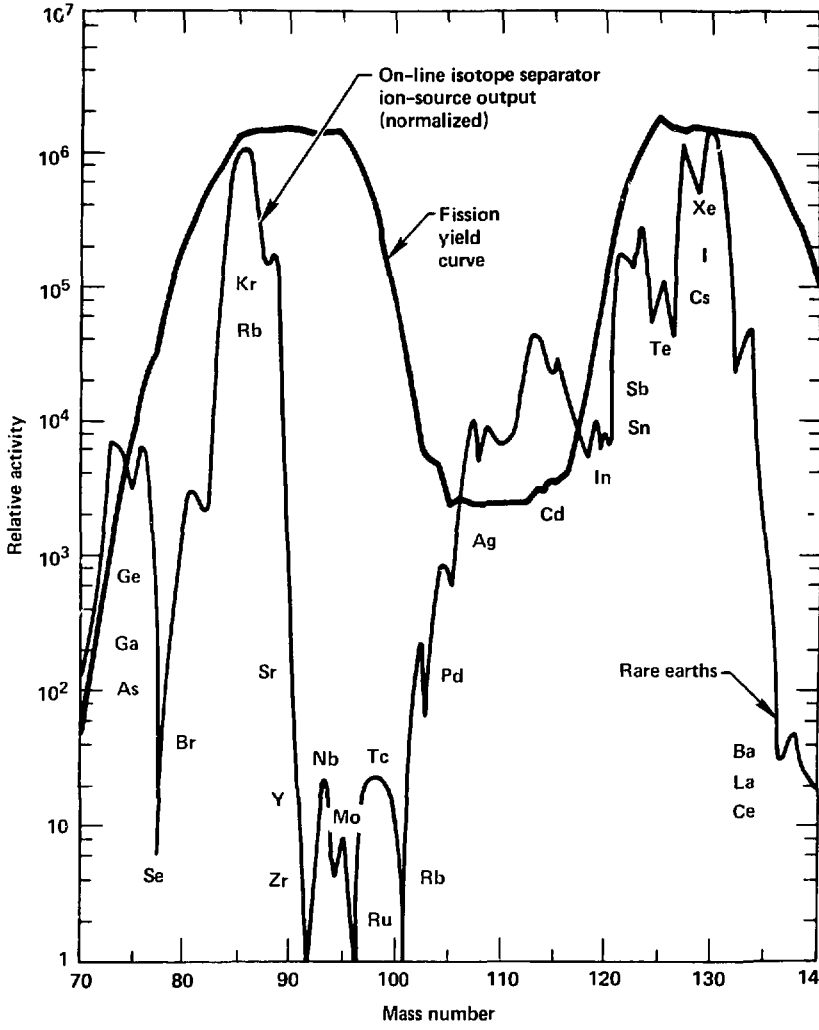

Fig. II.1. Comparison of the fission yield curve for the thermal neutron fissioning of ^{235}U with the output of a typical on-line isotope separator. (LIE80)

system. I consider a detector system which could be operated at a maximum count rate of A_m; the nuclide of interest has a half-life of t_i and a decay constant of λ_i (= ln 2/t_i). I assume that the continuous system operates at a constant count rate of A_m (the maximum rate).

For the batch processor, two times are required to characterize the system, the time the detector is on, T_c , and the time the detector is off, T_n. Thus the average count rate of the batch system, C_b, is

$$C_b = A_m \frac{1 - \exp(-\lambda_i T_c)}{\lambda_i (T_c + T_n)} \qquad \text{(II.2)}$$

For the batch process, if T_c and T_n are both twice t_i, the efficiency (C_b/A_m) is 27%; if T_c is 2.5 half-lives and T_n is 4 half-lives, the relative efficiency drops to 18%. In Eq. (II.2) there is a value of T_c which maximizes C_b for a given T_n. In Fig. II.2 this maximum value of C_b is plotted against T_n. This plot shows that if T_n is held to two or three half-lives, then an efficiency of 25% relative to the continuous method can be achieved.

This 25% efficiency is sufficient as a practical example illustrates. Antimony-134 has been studied with the LLNL AUTOBATCH system and with the Mainz batch and continuous chemistry systems. The experiments at Mainz took 4 weeks and 1 week respectively to obtain data of approximately equal quality. The experiment on the LLNL AUTOBATCH took 5 days to acquire significantly better data; indeed, only 2 h were required to identify the four known lines of ^{134}Sb and confirm the intensities observed at Mainz (LIE80).

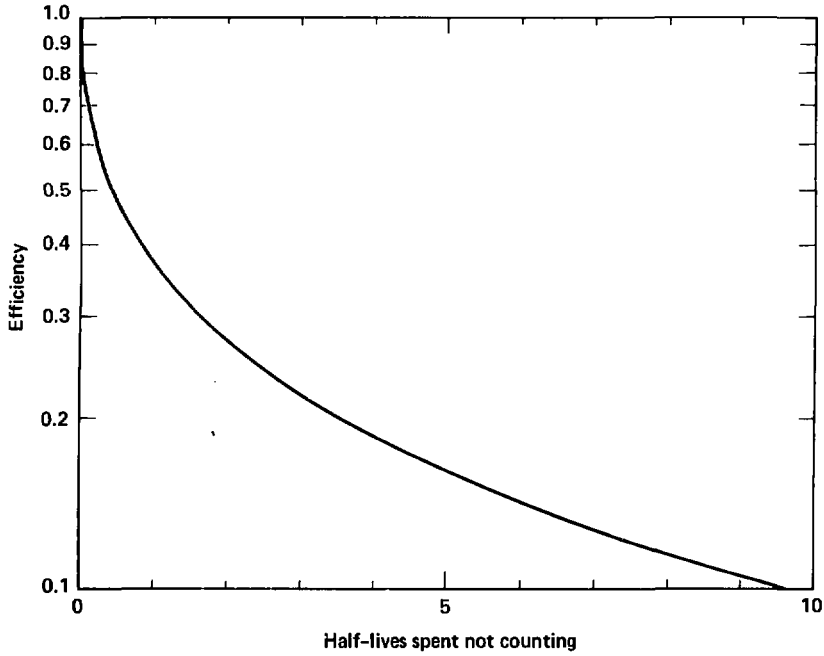

Fig. II.2. Efficiency of a batch processor as a function of T_n, the time spent not counting. For each value of T_n the maximum value of eff(T_c) is plotted.

However, samples chemically separated from fission products rarely have only a single-component activity. Reasonable analysis of a multi$_i$ le-component sample requires consideration of both direct (parent) and daughter product activities of varying half-lives in addition to the desired activity. To understand the advantages and limitations of each type of system the production of various isotopes, desired and undesired, must be treated on an equal footing. For both types of systems I assumed that any isotope with a half-life shorter than that of the isotope of interest can be ignored. (In practice, sample counting begins only after most of the shorter-lived species have decayed away.) The activity from a nuclide i at time t_1 during irradiation is

$$A_i(t_1) = \lambda_i N_i(t_1) = Y_i R_f \exp(-\lambda_i t_s)\left[1 - \exp(-\lambda_i t_1)\right] \quad , \tag{II.3}$$

where Y_i is the yield of the nuclide i, R_f is the fission (or other production) rate, and t_s is the time between production of the activity and the beginning of counting. The yield can usually be taken as the fractional cumulative yield, however detailed consideration may require a more complex analysis.

In the batch system the value $\lambda_i T_1$ is small so that the initial source activity becomes

$$A_i(T_1) = R_f Y_i \lambda_i T_1 \exp(-\lambda_i t_s) \quad , \tag{II.4}$$

where $A_i(T_1)$ indicates the activity after an irradiation of duration T_1 and separation time t_s. The decay rate of the directly produced activity is given by

$$A_i(t_c) = R_f Y_i \lambda_i T_1 \exp(-\lambda_i t_s)\exp(-\lambda_i t_c) \quad , \tag{II.5}$$

and the number of decays observed during the counting period of duration T_c is

$$N_i(T_c) = R_f Y_i T_1 \exp(-\lambda_i t_s)\left[1 - \exp(-\lambda_i T_c)\right] \quad . \tag{II.6}$$

For the daughter products, j, of this activity, i, the decay rate is given by

$$A_j(t_c) = \frac{R_f Y_i \lambda_i \lambda_j T_1 \exp(-\lambda_i t_s)}{\lambda_j - \lambda_i}\left(\exp(-\lambda_i t_c) - \exp(-\lambda_j t_c)\right) \quad , \tag{II.7}$$

and the number of daughter decays observed is

$$N_j(T_c) = \frac{R_f Y_i \lambda_i \lambda_j T_1 \exp(-\lambda_i t_s)}{\lambda_j - \lambda_i} \times \left[\frac{1 - \exp(-\lambda_i T_c)}{\lambda_i} - \frac{1 - \exp(-\lambda_j T_c)}{\lambda_j}\right] \quad . \tag{II.8}$$

For the continuous system only the activity equations are necessary. The intent of the continuous system is that it be operated for t_1 much longer than any of the half-lives involved, thus the activity equation (Eq. (II.3)) becomes for the direct activities

$$A_i(t_1) = R_f Y_i \exp(-\lambda_i t_s) \quad . \tag{II.9}$$

For the daughter products of the continuous processor the activity is given by

$$A_j(t_1) = \frac{R_f Y_i \exp(-\lambda_i t_s)}{\lambda_j - \lambda_i}\left[\lambda_i - \lambda_j - \lambda_i \exp(-\lambda_j t_c) + \lambda_j \exp(-\lambda_i t_c)\right] = R_f Y_i \exp(-\lambda_i t_s) \quad . \tag{II.10}$$

In Fig. II.3, I present the ratio N_j/N_i as a function of the half-life ratio τ_j/τ_i for a batch processor. The sample is to be counted for a period $2\tau_i$. For a continuous processor the ratio N_j/N_i equals one.

With these equations I can consider a three component system: the desired isotope, i, its daughter, j, and a longer lived isotope, k. The most important information is the relative rate at which decays of the desired isotope are observed. For the batch processor the limiting activity is the activity at zero time from these isotopes.

$$A_m = R_i T_i [Y_i \lambda_i \exp(-\lambda_i t_s) + Y_k \lambda_k \exp(-\lambda_k t_s)] \quad . \tag{II.11}$$

This relationship determines $R_i T_i$ in Eqs. (II.6) and (II.8) giving the average usable decay rate for the desired nuclide

$$C_b = A_m \frac{(1 - \exp(-\lambda_i T_c))}{\lambda_i (T_c + T_n)} \left[1 + \frac{\lambda_k Y_k}{\lambda_i Y_i} \exp((\lambda_i - \lambda_k) t_s) \right]^{-1} \quad . \tag{II.12}$$

For the continuous processor the limiting activity is

$$A_{in} = R_i [2 Y_i \exp(-\lambda_i t_s) - Y_k \exp(-\lambda_k t_s)] \tag{II.13}$$

which determines the value R_i in Eqs. (II.8) and (II.9), yielding an average observed decay rate for the desired nuclide, i,

$$C_c = A_m \left[2 + \frac{Y_k}{Y_i} \exp((\lambda_i - \lambda_k) t_s) \right]^{-1} \quad . \tag{II.14}$$

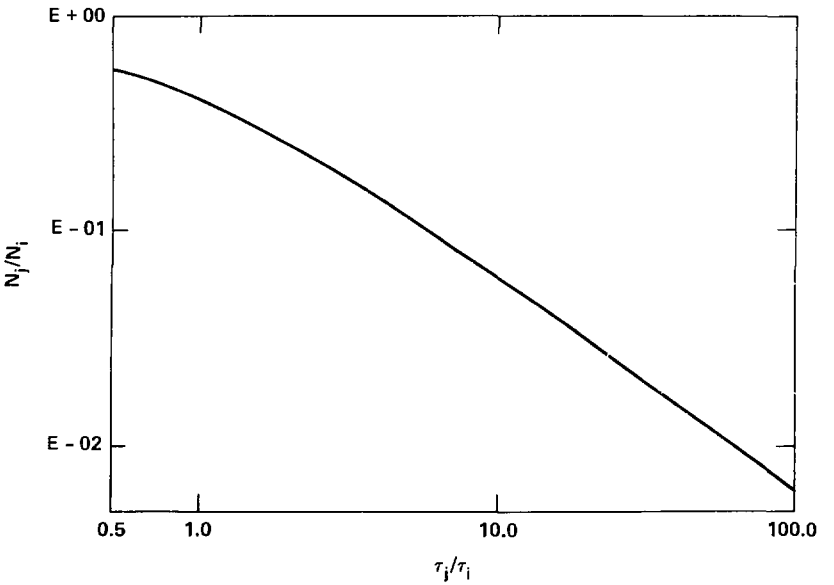

Fig. II.3. Plot of the ratio of the number of daughter counts to the number of parent counts, N_j/N_i (from Eqs. II.6 and II.8), against the half-life ratio τ_j/τ_i. This plot shows that the batch processor has considerably less daughter contamination than the continuous processor. For the continuous system (Eqs. II.9 and II.10) N_j/N_i equals one.

As an example, assume that $\lambda_j = \lambda_k = 0.2\lambda_i$, $t_s = 0.2T_c$, $\lambda_i T_n = \lambda_i T_c = 2 \ln 2$, and $Y_j = Y_k$. With these conditions the average decay rate for the desired nuclide for the batch process is 70% of that average for the continuous process. Further the half-life of the daughter, j, has no effect on this ratio and the fraction of desired decays are substantially higher for the batch process than for the continuous process, 64% to 30%, respectively.

Breaking the total acquisition period into shorter periods with the data recorded into different spectra in each period further improved the data acquired on the batch system. Equations (II.6) and (II.8) show that this results in the desired data being concentrated in the early spectra and the undesired data being placed into later spectra. This procedure has no effect on the continuous process as the activities are time independent. For the continuous system the value of t_s can be varied to differentiate between direct activities of differing half-lives, but will not differentiate between daughter and parent as the daughter decay constant does not enter into the activity in Eq. (II.10).

The sample produced by the continuous separation is effectively an equilibrium sample. The equations show that the contribution to the continuous process from daughter products is nearly equivalent to the contribution from the desired isotope and the contribution of longer lived species differs only by the ratio Y_i/Y_j.

From the above analysis, I conclude that the batch process is competitive with the continuous method for isotopes with half-lives down to approximately 5 s. For isotopes with half-lives shorter than this it is unlikely that a batch separation system could recycle within two to three half-lives of the desired nuclide which is required to keep the average count rate competitive with a continuous system.

Making the Batch Separation Process Competitive with Continuous Separation Process

There are many batch process chemistries available for isolating a radioactive sample from fission products. (See HER69, MEY79a, and TRA78 for reviews of fast chemistry.) Here I discuss two batch chemistry systems that use these processes for studying short-lived fission products. Both of these systems had their good points, but neither could meet the criteria established in the previous section for an efficient system for nuclides with half-lives less than 1 min. Trautmann and Hermann (see TRA78) at the Institüt für Kernchemie der Universitat Mainz pioneered fast batch chemistries with separations as fast as 1 s. However, their recycle time was 20 min. Another batch system was developed at LLNL by Meyer and Landrum. This system made use of slower chemistries with separations of 45 s, but had a recycle time 3 min. One of the aims of my thesis project was to construct a batch-process chemistry system suitable for studying short-lived species which combined the fast separations similar to those used in Mainz with the rapid recycling developed at LLNL.

The Original LLNL System

The batch processor at LLNL was used for detailed nuclear spectroscopic measurements. The source of fission products was uranium samples irradiated in a 3-MW pool-type reactor as fast as the separation system could process them. Although this system was largely automated, the individual components were slow and not integrated. Each uranium sample had to be manually loaded into the irradiation and transport system. When the irradiated sample arrived at the chemistry station, the program controlling the automatic separation process had to be manually started via a command entered at a teletypewriter. After the signal was given, it took more than a second to extract the sample from the transport capsule. Valves that controlled the reagent flow took tenths of seconds to respond. Reaction vessels were very large, up to 200 ml, requiring excessive amounts of time to transfer solutions. The sample separation was automated, but once the sample was separated, it had to be transferred manually to the detector location. After the sample was taken to the detectors, the chemistry system was automatically cleaned, reconditioned, and refilled; only a new container for the final sample had be to inserted manually before the next cycle.

Thus, although the LLNL system was slow, the components were basically amenable to automation.

One other drawback to the original LLNL batch processor was that the failure rate was high. Parts failed frequently: valves stuck, the irradiation and transport subsystem jammed, etc., resulting in considerable lost time. Thus, the reliability and durability had to be improved for the system to run efficiently for short-lived samples. With a goal of 20 chemically separated samples per hour, a 10% failure rate at 5 min down time per failure, the actual number of samples processed is 86% of the goal. As the number of samples processed per hour increases, the penalty for failure becomes increasingly severe. When the target rate is 60 samples per hour, the 10% failure rate drops production to 67%; at 120 samples per hour, production drops further to 50%. Thus, reliability and durability become increasingly crucial features as the sample half-life decreases.

The Mainz System

The Mainz batch system was used to measure the half-lives and major transitions for ^{84}As (5 s), ^{85}As (2 s), and ^{104}Nb (0.8 s). (See TRA78 for a complete list of their chemistries.) The source of fission products was uranium sample irradiated in a TRIGA reactor which could only be pulsed every 20 min. At this pace, there was sufficient time to clean, recondition, refill, and reassemble the chemistry apparatus by hand. Thus the Mainz chemistry system shown in Fig. II.4 incorporated many strictly manual features. Stopcocks were used for valves, syringes injected measured quantities of chemicals, and zinc metal powder was used for a reagent, none of which were suitable for automation. The earlier efficiency analysis shows that for ^{84}As this system was 0.6% efficient relative to a continuous system.

The AUTOBATCH System

A new automated batch chemistry system AUTOBATCH was built taking advantage of some of the existing components of the LLNL batch processor, as well as the fast separation chemistries developed at Mainz. The goals of this system were: fast sample preparation of approximately 1 s, rapid recycle time of about 15 s, and high reliability and durability with about 1000 cycles in 8 h.

To achieve these goals, I elected to use standard commercially available components wherever possible. For example, many solenoid valves were used in the system and the commercially available ones were found to be faster, more reliable, and easier to replace than custom-designed valves. It was also obvious that moving parts had to be minimized. Where possible, the moving part was eliminated. If this was not possible, the extent of the required motion was minimized and the component redesigned in such a way that the action was not time-critical.

Most importantly, the system had to be fully automated and integrated. All steps, from irradiation, through separation, to data acquisition and recycling, were computer-controlled. Thus I eliminated all manually controlled components. Hands-on steps (e.g., changing drying tubes and refilling reagent reservoirs) could be required no more frequently than every 15 min, not for every sample. Such complete automation required that all components be completely integrated. The sample transport, chemistry, and data acquisiton subsystems had to communicate in such a way that changes in one subsystem did not require changes in all the others.

AUTOBATCH System Design

The AUTOBATCH system (Fig. II.5) was designed with total automation as a major design criterion. The system was conceived as a central controller with three major subsystems: sample transport and irradiation, chemistry, and data acquisition. These three subsystems would be linked through the controller but otherwise independent.

The sample cycle was designed to proceed as follows. The controller would initiate the sample cycle by starting the irradiation and transport cycle and simultaneously signalling the chemistry system that sample irradiation had begun. When the irradiated sample arrived at the

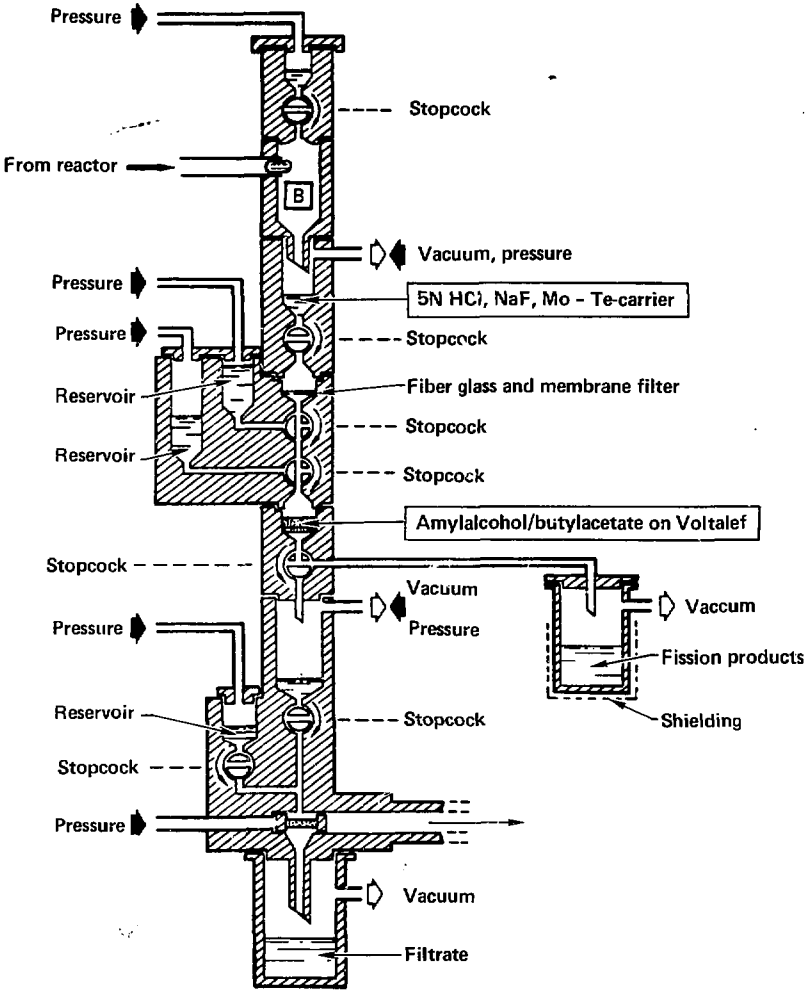

Fig. II.4. Schematic drawing of Mainz "building block" batch processor. The pieces require considerable machining. The stopcocks must be manually reset and the reservoirs manually refilled after processing each sample. (Adapted from TIT77.)

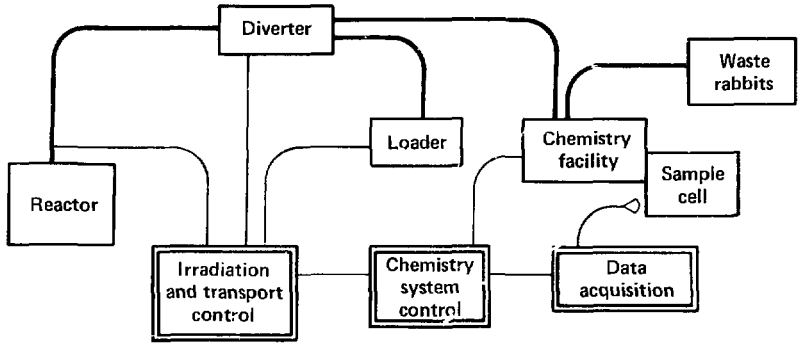

Fig. II.5. Block diagram of AUTOBATCH. Sample transport lines are shown in heavy lines, computer control and data lines are shown in light lines.

receiver, the raw fission product sample was extracted from the transport capsule and the chemistry sequence began. Sample separation and processing was completed when the finished sample arrived at the detector location. The chemistry subsystem then signalled the data acquisition system via the controller to start counting the sample. While the sample was being counted, the chemistry apparatus was automatically cleaned and reconditioned, the used sample transport capsule was ejected, and the next capsule was loaded. The chemistry subsystem was signalled by the controller when the data acquisition sequence was completed and the sample cell was then cleaned and reconditioned. At this point, AUTOBATCH was ready to process the next sample.

The entire irradiation, separation, and data acquisition sequence would take place without interruption and without intervention. The only required manual steps were to refill the sample hopper at the loader-launcher every 35 samples, which did not interrupt the sample processing, and to refill the reagent reservoirs (every 30 to 60 min), which required less than 5 min of down time.

The Transport and Irradiation Subsystem

The transport and irradiation subsystem consisted of four major components all under computer control: the loader-launcher, the diverter, the irradiation station, and the receiver (see Fig. II.6). The loader-launcher hopper held 38 sample capsules; capsules were loaded via a pneumatically activated breech mechanism. Microswitches detected the breech position (open, closed, or in between) and a photosensor confirmed the loaded/not loaded status. The actual loading sequence required 5 s. A second photosensor monitored the number of capsules in the hopper and triggered an audible alarm when there were only three capsules left. To save time the load sequence was executed during the cleanup sequence of the chemistry subsystem.

The diverter directed the sample capsule to its proper destination. It was moved by pneumatic cylinders and its proper positioning was confirmed by microswitches. Positioning required 0.3 s.

The irradiation station was located adjacent to the reactor core. The sample capsule was sent pneumatically to a stop at the bottom of the transport tube and remained there during the preprogrammed irradiation period. The irradiated capsule was then pneumatically ejected from core and sent to the chemistry facility.

The receiver was located at the chemistry facility. The irradiated sample capsule was sent to the receiver where it was impaled by its own momentum on the extraction needle. The gas pressure in the pneumatic tube behind the capsule prevented it from rebounding off the needle.

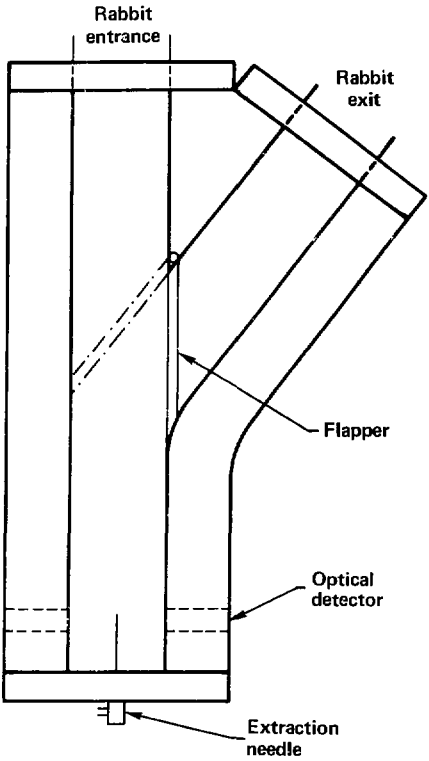

Fig. II.6. The receiver for AUTOBATCH. The rabbit enters the vertical channel and is ejected out the right channel as shown by arrows. The eject path is controlled by the flapper, which is moved to the position shown in dashed lines for ejection. The photo cell near the bottom of the receiver detects the presence of the rabbit. The extraction needle is shown in the bottom of the receiver.

The empty capsule was pneumatically ejected at the end of the chemistry sequence, with a flapper directing the capsule into the waste container (see Fig. II.6).

The major design consideration of these components was reliability without loss of speed. Because parts that must move rapidly often lack durability, I maintained a high overall cycle speed by allowing some of the transport functions to take place concurrently with other steps. For example, in the loader, this was achieved by loading the sample capsule while the previous sample was being processed at the chemistry station. In the receiver, the flapper moved and the empty capsule was ejected while the data acquisition was in progress. Only the diverter and the sample capsule itself had to move quickly. In Appendix 1, I give a detailed description of the components and compare the original components to the AUTOBATCH versions.

The Chemistry Subsystem

To demonstrate the efficiency of the AUTOBATCH system, I selected a hydride chemistry to isolate the 5A and 6A elements. These regions have previously been inaccessible for detailed spectroscopic study. Both of these regions give very low yields with on-line isotope separators as shown in Fig. II.1, precluding their study by this technique. Trautmann et al., have measured half-lives and major transitions of neutron rich As and Se isotopes (KRA75, KRA70) but their batch system is not suited for detailed spectroscopic examination of the short-lived isotopes required for nuclear structure studies (see the discussion on the Mainz batch system above).

The first step in my hydride chemistry is to produce the hydride gases of the elements by creating nascent hydrogen in aqueous solution. The hydride gases are then sequentially stripped from the gas stream with the desired element depositing in the sample cell. Elements which would also deposit are stripped out prior to the cell. Those which will not deposit in the sample cell are allowed to pass through.

The hydride reaction is achieved by a strong reducing agent, sufficiently strong to reduce the hydrogen ion to nascent hydrogen. The elements of interest are also reduced from the positive valence states to the neutral state. Hydride gas formation dominates over element formation for two reasons:

1. The conditions used form a large excess of nascent hydrogen compared to the element of interest, which statistically favors formation of the hydride gas.
2. The metal atoms are surrounded by a sphere of water molecules causing them to move slowly. The nascent hydrogen is not hydrated and can move very quickly.

The hydride gases can be produced by treating an acid solution of fission products with one of the following: (1) direct electrochemical production, (2) zinc metal powder, or (3) sodium borohydride solution. Electrochemical production of the hydride gases was ruled out since it required approximately 1000 A of current for 0.1 s, beyond the capacity of available power supplies. Zinc metal powder, as used in the system at Mainz (FOL69), is traditionally considered the reagent of choice for this reaction. However, zinc metal is difficult to handle with automated equipment. The desire to automate the system dictated the choice of the sodium borohydride reaction. Sodium borohydride solution is easy to inject and easy to clean up in an automated system and gives sufficient yield of the desired hydrides to preserve sample purity.

In my hydride chemistry, the noble gases are first removed from the sample by sparging. The sample is acidified and thoroughly mixed and then the sodium borohydride is added and mixed. The gas phase containing the elements of interest and liquid phase containing the remaining fission products must then be separated. In a standard hydride distillation reaction, the slow step is separating the gas and liquid phases. Therefore, to use the hydride chemistry in the required time frame (less than a second), I had to devise some means of rapidly separating the two phases. Trautmann (TRA78) has noted that many standard chemical reactions, when performed in a standard way, are too slow for the purposes of on-line chemistry. These reactions can, however, be used if they are performed in nonstandard ways that speed the reaction. To accomplish these steps very rapidly, I designed the still and cyclone separator shown in Fig. II.7.

The sample and reagents are introduced into the still through ports that are tangential to the walls of the still. The tangential entry creates rapid rotational motion of the solutions, forcing them to remain on the walls of the still. This gives the large surface area required for good sparging and, at the same time, provides rapid and complete mixing of the reagents.

The gas and liquid phases are separated in a similar manner. The pressure created by the formation of the hydrogen gas (created in the still) drives the gas-liquid mixture into the cyclone separator. The tangential entry into the separator generates rapid rotational motion and the centrifugal force holds the liquid on the circular walls of the cyclone allowing the gas to escape out the center exit. In this manner, I achieved a very rapid gas-liquid separation.

I have made a film study of the cyclone separator (LIE79) showing that the cyclone performs as anticipated. The study made use of the high speed motion picture camera developed at LLNL, which was used at 2000 frames per second. At this speed the motion was slowed a factor of 100 times. This study showed that cyclonic motion was present in both the still and the separator. In

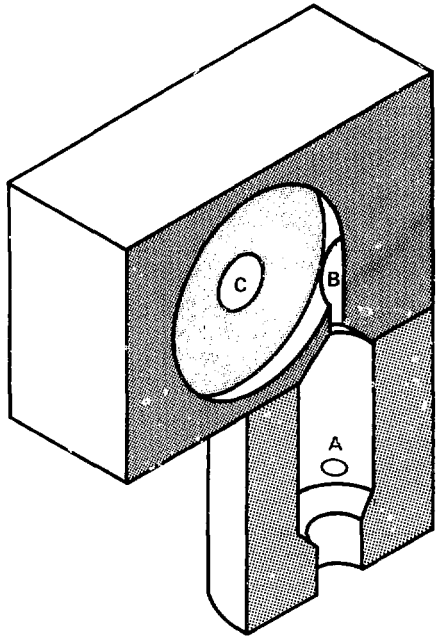

Fig. II.7. The still and cyclone separator used in AUTOBATCH hydride chemistry. The still is the lower chamber, with a typical inlet port shown (A). The gas-liquid mixture is forced through orifice B into the cyclone where the gas and liquid are separated. The gases exit through orifice C.

the still the motion produced effective mixing of the reagents. In the cyclone it effectively separated the gas and liquid phases.

In the standard hydride reaction, the gas and liquid phases are separated simply by gravity; this requires a large still and a gentle reaction. As a result, this step is very slow. An estimate of the separation enhancement possible with the cyclone separator is obtained from the flow rate of the gas-liquid mixture entering the cyclone:

$$v_l = \frac{\text{volume}}{\text{area} \times \text{time}} \tag{II.15}$$

$$140 \text{ cm/s} = \frac{2 \text{ ml}}{\pi \times 0.15^2 \text{ cm}^2 \times 0.2 \text{ s}} ,$$

where the sample volume is divided by the cross-sectional area of the orifice and the time required for the transfer. I ignore the effects of the expanding gas volume that actually serve to increase the velocity. The centrifugal acceleration is then

$$a = \frac{v_l^2}{r} = \frac{(140 \text{ cm/s})^2}{2 \text{ cm} \times 980 \text{ cm/s}^2} = 10 \text{ g} \quad . \tag{II.16}$$

Thus I achieved a tenfold increase in the gas-liquid separation forces over that possible with the simple gravitational method.

This procedure generates the hydride homologues indicated previously. The next step is to isolate the desired elements from among these homologues.

The remaining chemical separation steps are carried out in the gas phase. The element of interest is collected in the sample cell on a glass-wool plug wetted with the appropriate reagent. Those elements that would also collect on the glass wool were removed from the gas stream before they reached the plug; the elements that would not collect were allowed to pass through.

Fast Arsenic Chemistry

Following the general chemistry procedure discussed above, the hydride chemistry specific for arsenic is as follows:

- A raw sample consisting of 1.0 mg ^{235}U dissolved in 0.7 ml of 0.14 N sulfuric acid was irradiated for 150 ms.
- The irradiated sample is extracted and sparged for 500 ms to remove the noble gases.
- The sparged sample is then acidified with 1 ml of 9 *M* HCl containing 2 mg/ml Sn^{2+} as a hold-back carrier, to reduce the tin contamination.
- 2 ml of sodium borohydride solution (125 g/l $NaBH_4$) is added.
- The hydride gases are passed through a trap to remove entrained water, SbH_3, H_2Se, H_2Te, and SnH_4. This trap is clear plastic tube 1.8 cm in diameter and is filled, in the direction of gas flow, with 15 cm of anhydrous $CaSO_4$ (Drierite), 40 cm of anhydrous sodium hydroxide (Ascarite) followed by 5 cm of anhydrous $CaSO_4$ (Drierite).
- The arsenic is collected on a glass-wool plug wetted with 9 *M* HCl containing 5 ml/l liquid bromine.

Table II.1 gives the computer-controlled timing sequence for the chemistry to separate ^{84}As. Figure II.8 shows the chemistry subsystem and its control valves. Figure II.9 shows the flow of the elements through the system.

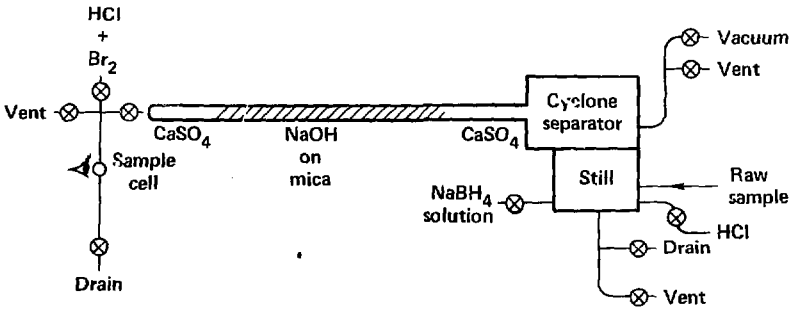

Fig II.8. The AUTOBATCH chemistry system is shown schematically. The ⊗ are computer controlled solenoid valves. A gamma ray detector is shown to the left of the sample cell. Flow direction is indicated by arrows except for the vents which are bi-directional.

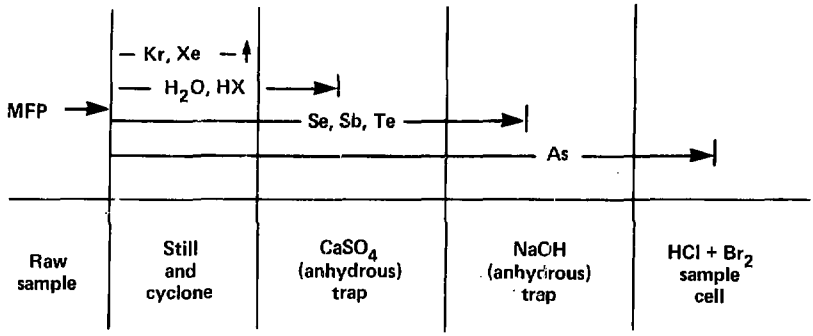

Fig. II.9. The flow of various compounds in the hydride chemistry. Indicated compounds go to the end of the bar except for Kr and Xe which are removed before reaching the $CaSO_4$ trap. MFP means mixed fission products and HX means HCl, HBr and HI.

Table II.1. Computer-controlled timing sequence for ^{84}As (5-s half-life).

Operation[a]	Step time, s	Elapsed time, s
Return sample from reactor core	1.0	1.00
Extract sample from capsule and purge noble-gas fission products	0.5	1.50
Acidify sample with HCl + Sn (1 ml)[b]	0.09	1.59
Inject $NaBH_4$ solution into still (2 ml)	0.1	1.69
Inject gas-liquid mixture into cyclone and pass hydride gas through trap	0.25	1.94
Start detectors counting	–	1.94
Drain still and cyclone	1.6	3.54
Wash still and cylone with water	0.6	4.14
Drain still and cyclone	1.0	5.14
Purge $NaBH_4$ line	0.9	6.04
Rinse still with water	1.2	7.24
Drain still	1.2	8.44
Recondition still with HCl + Sn	0.24	8.68
Drain still	2.4	11.08
Wait for end of data-acquisition step[c]	T	11.08 + T
Wash sample cell with HCl + Br	3.1	14.18 + T
Remove excess HCl + Br from sample cell	2.4	16.58 + T
Total chemistry time		16.59 + T

[a] All volumes measured by time valve were open; volumes given are estimates.

[b] A 10-s delay was added here for $^{82,83}As$ studies.

[c] Additional time may be required for data aquisition.

III. Experimental Measurements

With the fast chemistry system described in the previous section, I made detailed gamma-ray spectroscopic measurements following the β decay of fission product (FP) arsenic, with emphasis on the decay of ^{83}As to study the nuclear structure of ^{83}Se. This work allowed me to make the first identification of the intruder vibrational band structure in a 49-neutron nucleus. In the process, I deduced that ^{83}As has a ground state spin and parity of $5/2^-$ and redetermined the absolute ground state β branch from ^{83}Se^m to be 38%.

I carried out four separate experiments on the FP arsenic decay. These experiments studied ^{84}As decay and $^{82, 83}$As decay, determined the energy calibration, and investigated growth and decay of daughter species. The growth and decay experiment was done to establish the β branches from ^{84}As ground state to ^{84}Se the ground state and from the ^{83}As ground state to the ^{83}Se isomeric state. The parameters pertinent to these measurements are given in Tables III.1a and III.1b. For the ^{82,83}As decay studies, I added a 10-s delay before separating the arsenic from the fission products to allow the 5-s ^{84}As to decay, thus greatly reducing both the ^{84}As and ^{84}Se activities in the counted samples (see Table II.1).

Spectroscopy Apparatus

Since the sample counting cell was an integral part of the chemistry system, the detectors were immediately adjacent to the chemistry facility. This, in turn, necessitated that the detectors be heavily shielded from the residual fission-product activity. To maximize use of each sample, simultaneous single-parameter gamma-ray and three-parameter gamma-gamma-time coincidence measurements were made. The detector-sample cell arrangement is shown in Fig. III.1. The shielding consisted of 15 to 25 cm of lead between the detectors' active volumes and external sources of activity. The arrangement shown was used for the coincidence detectors at 180°. The sample cell was 0.5 cm in diameter and placed between two 0.5-cm-thick lead shields with columnating holes between the detectors and the sample cell. The shields reduced detector-to-detector backscattering of photons, which would give intense false coincidences. The shields were carefully arranged so that they did not partially screen the singles detector. The remainder of the data acquisition system was located in a separate room 12 m distant from the detectors.

The details of the spectroscopy are given in Ref. LAN79. Here, I give a brief description of the spectroscopy apparatus emphasizing the improvements made since that report.

Gamma-Ray Singles Measurements

Single-parameter MCMS data were acquired to establish correct energies and intensities. Most of the singles data were acquired using a Data General Inc., NOVA 1200 minicomputer as a 4096-channel analyzer which was capable of holding six 4096 channel spectra. For the ^{84}As experiment, some of the singles data were taken on a Canberra 80 analyzer using 8192 channels and two MCMS spectra to obtain good energy resolution over an 8-MeV range.

The data for the growth and decay experiment were acquired using a real-time clock. Dead time was monitored with the 392-keV gamma ray from a ^{113}Sn radioactive source. The observed count rate for this photopeak measured the relative dead time of the counting system. Tin-113 was chosen because it emits gamma rays only at an energy below that of the gamma rays of interest.

An ORTEC high-purity germanium (HPGe) detector was used for all single-parameter data. Its efficiency was calibrated from 0.1 to 10 MeV (LIN80). This calibration included the cadmium-copper cap (each 0.7 mm thick) on the detector, which was used to absorb the fluorescent lead x-rays. This detector had a FWHM of 2.2 keV at the ^{60}Co 1332-keV gamma ray. The FWHM observed in the data was 3.0 keV at 1331 keV due to count rate variation during the data acquisition period.

Table III.1a. Details of the gamma-ray spectroscopy experiments for ^{82,83,84}As β^- decay, giving timing, energy range, gain, and peak to background ratios for sample transitions. The two ^{84}As experiments differ in the timing and energy ranges used.

	SINGLES EXPERIMENT			
	^{82,83}As	^{84}As-Hi	^{84}As	Calibration
Timing (s)				
Start separation	11	1	1	1
Count time	12.0-26.7	2-7	2.0-4.1	2.0-8.6
	26.7-40.6	9-13	4.1-6.2	8.6-16.1
	40.6-54.2		6.2-8.3	
			8.3-15.4	
Gross counts	7.4E8	1.0E8	4.1E7	9.3E7
in spectrum	3.8E8	4.6E7	3.2E7	6.4E7
	2.3E8		2.6E7	
			4.7E7	
Energy range (MeV)	0-4.1	0.54-8.5	0-4.1	0-4.1
Gain (keV/chan.)	1.0	1.08	1.0	1.0
Peak/background				
Peak	734-keV	1454-keV	1454-keV	
Counts	2.2E6/2.1E5	2.1E6/1.6E5	3.1E5/2.5E4	

Table III.1b. Details of the coincidence gamma-ray spectroscopy experiments following the decay of ^{82,83,84}As. Information is the same as in Table III.a.

	COINCIDENCE EXPERIMENTS		
	^{82,83}As	^{82,83}As angular correlation	^{84}As
Timing (s)			
Start separation	11	11	1
Start count	12	12	2
End count	55	55	15
Detector configuration	180°	90° & 180°	180°
Energy range (MeV)	0-6.4	0-6.4	0-8.2
Gain (keV/chan.)	0.83	0.83	1.0
Peak/Background			
Slice	734-keV	654-keV	1454-keV
Peak	1113-keV	755-keV	667-keV
Counts	24400/1000	1450/300 at 90°	12500/1400
Peak	2729-keV	755-keV	5151-keV
Counts	295/50	2750/450 at 180°	110/40

For the energy calibration, I used ^{133}Ba, ^{134}Cs, and ^{56}Co as standards (MEY78) to span the energy region from 0 to 3.5 MeV. Above 3.5 MeV, I used the gamma rays from the Cd(n,g) reaction for energy calibration (GRO68). The source of neutrons was beta-delayed neutrons from fission products. These standards gave a reliable energy calibration over the energy range from 0.2 to 7.0 MeV.

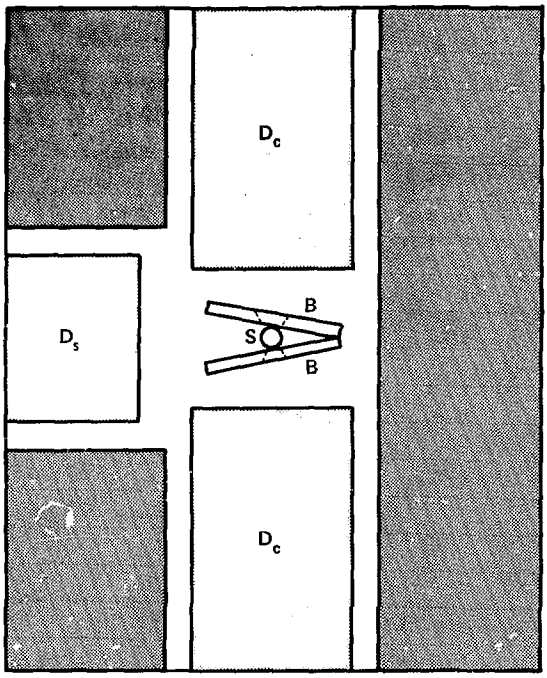

Fig. III.1. *Top view of the detector arrangement.* The coincidence detectors, D_c, are 180° apart. The singles detector is labeled D_s, the sample cell is labeled S. The backscatter shielding, B, is shown with the collimating holes drawn in dotted lines.

Gamma-Ray Coincidence Measurements

The coincidence measurements recorded the energy of two gamma rays and the time separating them, provided the time separating them was less than 350 ns. This defined a coincidence event. The detector charge collection time and other electronic noise produced a time-to-amplitude conversion (TAC) resolution of 10 ns FWHM. The detectors used to acquire the coincidence data were high-resolution ORTEC Ge(Li) detectors. The energy resolution of the detector was 2.2 keV FWHM for the ^{60}Co 1332-keV gamma ray.

All excited levels can decay by gamma-ray emission with half-lives ranging upward from less than 1 fs. The Ge(Li) detector system allows measurement of isomeric half-lives down to approximately 2 ns. To retain this resolution, I set the TAC gain to 1.39 ns per channel. Over the 512 channels available, this gave 350 ns over which a delay could be measured. Experimentally, the limits on observable level half-lives could be crudely determined in that I could not observe the half-life of either the 654-keV level in ^{88}Se (13.4 ps) or the 1225-keV level in ^{131}Sn (150 μs), although there was sufficient singles intensity of the pertinent gamma rays to easily see the half-lives if they were not outside my experimental limits.

The TAC data was used also to correct for chance coincidence events. A chance event occurred when the two gamma rays causing the coincidence event did not originate in the same

atom. I assumed that the TAC profile spectrum consisted of a Gaussian peak of true coincidence events on a flat background of chance events. I then accepted all events with a TAC value within the FWTM of the true coincidence peak and subtracted the events in an equal number of channels well removed from the true coincidence peak.

Two different energy ranges were used to cover the different possible ranges of excitation energy in the selenium nuclei. These ranges were set to observe the most energetic gamma ray possible in the nuclei of interest, which is limited by the Q_{β^-} value for the beta decays of the different arsenic species. The Q_{β^-} values are 6.4 MeV for ^{82}As, 5.6 MeV for ^{83}As, and 9.8 MeV for ^{84}As. However, the upper limit for ^{84}As is further reduced to the neutron binding energy in ^{84}Se, 8.4 MeV. Levels populated above the neutron binding energy decay primarily by neutron emission and do not contribute significantly to the gamma-ray spectrum. With the upper energy limit set, the lower energy limit is set by the dynamic range of the analog-to-digital converter. The dynamic range is a factor of approximately 35, giving a lower energy limit of 180 keV for ^{83}As.

Included in the ^{82,83}As measurements were angular correlation measurements with the coincidence detectors at 90° and 180°. These measurements were made to establish the $0^+ \rightarrow 2^+ \rightarrow 0^+$ γ cascades in ^{82}Se. They were also used to measure the anisotropy when the coincidence data were used to determine transition intensity. The detectors were moved to a distance of 10 cm for the angular correlation measurements. At this distance a detector presented an area of 0.16 steradian (an included angle of 9°) to the decaying source.

Shown in Fig. III.2 is plot of the spectrum of events in coincidence with the 1455-keV gamma ray obtained from the ^{84}As experiment. These coincidences occur primarily in the ^{84}Se nucleus. The total number of counts in the 667-keV and 5151-keV peaks from the 1454-keV gate is an indicator of the quality of the experiment and the validity of my assignments for high-lying levels. For ^{83}As, I include a plot of the 582-keV gate (Fig. III.3) with an inset showing the low-intensity transitions from the natural parity levels. The 582-keV gamma ray has an intensity of 109 5 relative to 1000 for the 734-keV gamma ray and the 381-keV gamma ray has an intensity of 0.4 showing that very weak transitions can be measured.

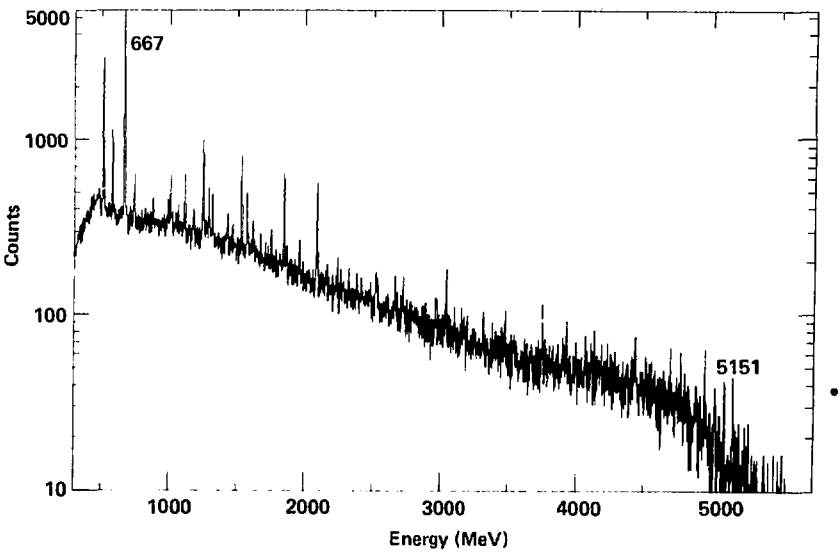

Fig. III.2. Plot of the 1455-keV gate from the ^{84}As experiment.

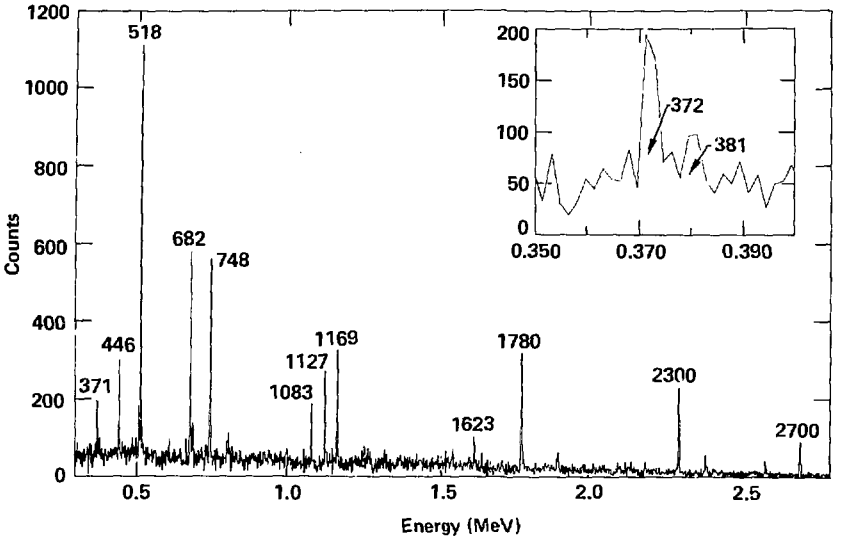

Fig. III.3. Plot of the 582-keV gate from the ^{82,83}As experiment. The inset shows the low intensity transition from the $3/2_1^-$ state to the $5/2_1^+$ state.

Data Analysis

Single-parameter data were analyzed with either the GAMANAL (GUN72) or FITEK (STO80) computer codes; the use of GAMANAL is described in Ref. LAN79. However, the analysis of my spectra by GAMANAL improved remarkably when the peak shape parameter P5 was reduced from 1.2 to 0.76. This parameter is not usually changed. Its effect is to increase the tail width of the peak. Coincidence data were first sliced (LAN79) to obtain single-parameter data from three-parameter data, then analyzed with the computer code PK2D (described below).

FITEK is an interactive routine, which uses peak shape parameters similar to those of GAMANAL. The user defines the fit region, the background at the endpoints of the fit region, and the peaks and their crude location by cursor control. The parameters may be constrained or allowed to vary until the best least-squares fit to a peak is obtained. The user also sets the background step height as a fraction of the peak height. In the fitting process, peaks may be dropped but not added. Once the best fit is obtained, the fit region is displayed showing the both experimental and calculated spectra and the background. The interactive nature of FITEK allows the user to inspect possible solutions much more easily than with GAMANAL, but correspondingly is much slower.

In the coincidence spectra generally poor statistics precluded the use of either GAMANAL or FITEK, which require good statistics. However, having produced 600 gated spectra slices from the two coincidence experiments, an automated procedure for analyzing the energy and intensity in the coincidence was needed. The common procedure for peak analysis in coincidence data is: first, to find a peak, second, find its endpoints, next, sum the counts over the peak, and then, subtract the background. This procedure cannot be automated because of the poor statistics of most coincidence spectra. Stevenson (STE77) had used an algorithm that took p channels of peak and b channels of background on each side of the peak and at each channel k defined

$$Y_k = \sum_{p} [C_i] - \frac{p}{2b} \sum_{2b} [C_i] \quad . \tag{III.1}$$

This algorithm generates reasonable peak areas but poor peak centroids. This is because the algorithm peak width is discrete but the experimental peak width varies smoothly as a function of energy.

A continuous function that imitates this algorithm is the second derivative of a Gaussian. It can be easily shown that convoluting this function with a Gaussian, constant, linear, and quadratic function gives the second derivative of a Gaussian, zero, zero and constant results, respectively. The results for the last three functions show that convoluting a spectrum background with the second derivative of a Gaussian should give nearly zero since, in principle, the background is smooth. For a convoluted Gaussian peak, the amplitude differs only by a multiplicative constant from the original peak amplitude and the centroid is unchanged when compared to the original peak. This suggests that, even though the peak shapes are not Gaussian, this algorithm would return reliable energies and intensities. Testing showed that this algorithm performed nearly as desired. It has two limitations: (1) the requirement of prior knowledge of peak widths and (2) the lack of noise damping. For the returned amplitude to be the peak area, the convolution function must be the same width as the peak. The peak widths are easily determined using the standard function of energy (GUN72). Noise is not damped because the convolution function passes a sine wave with a wave length comparable to the convolution width.

The convolution function used is

$$D(n) = (1 - 2(n/s)^2) \exp(-(n/s)^2) \tag{III.2}$$

where s is the width parameter and $n = C - C'$, where C is the center of the convolution function and C′ is the channel being considered. When convoluted with a Gaussian of area A_0 and width p, this results in

$$Y(C) = A_0 \frac{s^2}{s^2 + p^2} \left(1 - 2\frac{C^2}{s^2 + p^2}\right) \exp\left(-\frac{C^2}{s^2 + p^2}\right) \quad . \tag{III.3}$$

The actual convolution is carried out as the sum. In channel notation

$$Y_i = C_i + \sum_{n=1}^{4s} \left[(C_{i-n} + C_{i+n}) \times D(n)\right] \quad , \tag{III.4}$$

where C_i are the contents of channel i. The photopeak area and position are determined by fitting a parabola to the three points at every local maxima in the convoluted spectrum. This routine determines peak area and centroids without fitting the peaks. For coincidence spectra this is a distinct improvement over previous procedures.

Half-Life of the 582-keV Level

The half-life of the 582-keV level had not been measured, but while I was analyzing the data Hoff (HOF81) reported a tentative measurement of 5.0 ns based on the ^{82}Se(d,p)^{83}Se reaction. I determined this half-life from my gamma-gamma-time coincidence data. As will be discussed later, this half-life is important for the intruder levels, which are expected to have strongly hindered transitions to the natural levels.

The timing spectra were generated by gating on the energies of the two coincident gamma rays to create the spectrum of timing values for that coincidence. The TAC peak should have the shape of an exponential half-life curve smeared by a Gaussian:

$$Y(t) = \int_{t}^{\infty} A_0 \exp(-\lambda(t + t')) \frac{\exp(-(t'/s)^2)}{s\sqrt{\pi}} dt' \quad , \tag{III.5}$$

where t is the time, t' is the dummy variable for integration, A_0 is the height of the exponential curve, λ is the decay constant, and s is the Gaussian width which describes the timing resolution of the detector and electronics. If there is a significant amount of data in the region $t \gg s$ (e.g. $t > 3s$), then the lower limit can be replaced by infinity and

$$Y(t) = A_0 \exp(-\lambda t) \exp((\lambda s/2)^2) \tag{III.6}$$

is obtained, where λ is the logarithmic slope of Y. In this case $s = 6$ and there was very little data in the region where t is large; the entire peak must be fit. In working with the data, it was convenient to work in channels rather than time. The half-life was the tail width, $\ln 2/\lambda$ when fitting the time peak with Eq. (III.5).

To accurately determine the half-life when it is approximately equal to the timing resolution of the detector and electronics, I had to fit the entire timing spectrum. The timing resolution was determined from the timing peak resulting from the coincidence of the 734- and 1113-keV gamma-rays which is believed to have a half-life less than 0.1 ns. This peak was fit first with the tail parameters forced to zero, giving a FWHM = 9.76 ± 0.08 channels. Freeing the tail parameters changed the FWHM to 9.50 ± 0.14 channels with no observable improvement in the fit. These analyses showed that the peak was nearly symmetric, hence reasonable for fitting the peak width. However, both FWHM values produce a peak wider than the experimental peak at the extremes, where the tail width is most strongly affected. I determined that the FWHM = 9.4 gave a better fit in the outer portions of the peak and used this width in analyzing the 582-keV level time spectrum. Comparisons of calculation and experiment for both widths are shown in Fig. III.4.

The time spectrum used for the 582-keV level was a sum of direct coincidences with the 582-keV transition (the 518-, 682-, 748-, 1126-, 2300-, 2700-keV coincidences with the 582-keV transition were used). Before fitting the 582-keV level time spectrum, it was evaluated with FITEK. With the tail parameters forced to zero, the peak had distinctly asymmetric residuals. This residual asymmetry was removed when the tailing parameters were freed. The FITEK tail width was measured to be 2.5 ± 0.1 channel with a FWHM = 9.75. These values were not used directly because of uncertainty of the effect of the tail truncation device used in FITEK on the tail width.

I then calculated spectra from Eq. (III.5) for various tail widths and compared them to the experimental spectra. The best fit to the 582-keV level time spectrum was obtained with a tail width of 2.2 channels as shown in Fig. III.5a using a FWHM of 9.4 channels. For comparison, the experimental spectrum is also compared to calculated spectra with 2.0- and 2.4-channel tail widths in Fig. III.5b. The uncertainty in the FWHM is taken as 0.4 channel, the difference between the FITEK value and the FWHM used, and the uncertainty in the tail width is 0.2 channel, estimated from inspection of Figs. III.5a and III.5b. Treating these as independent errors, the total error is 0.45 channel. The gain in the TAC spectrum was 1.39 ns/channel; thus, the half-life was determined to be 3.1 ± 0.6 ns.

I have received information from Hoff (HOF82) that on remeasurement he obtained a value of 3.5 ± 0.2 ns.

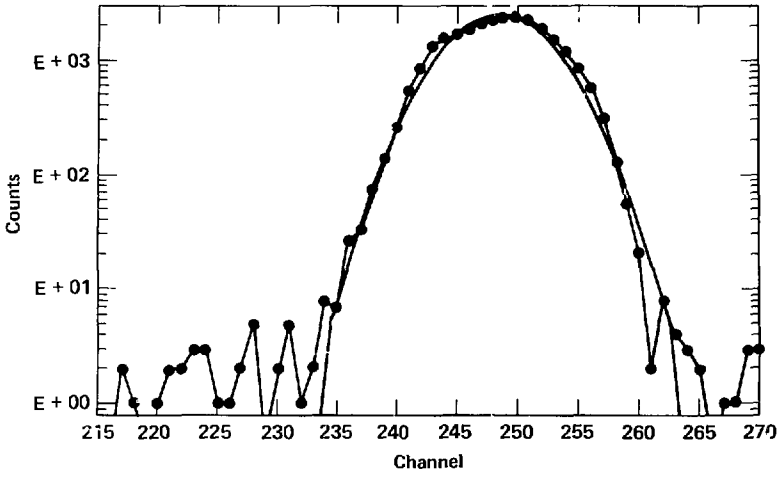

Fig. III.4. Comparison of the 734-1113-keV coincidence timing spectrum to a spectrum calculated with a 9.40 channel timing resolution. (●=data, —=calculation.)

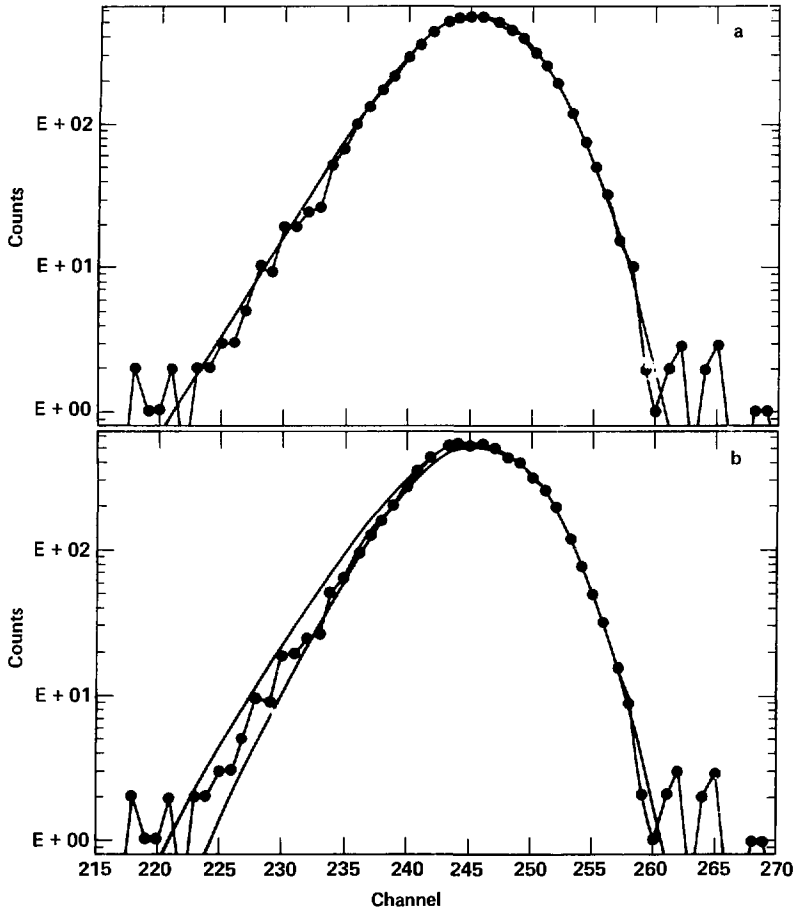

Fig. III.5. Comparison of the 582-keV level TAC spectrum with spectra calculated with a) 2.2 and b) 2.0 and 2.4 channel half-lives. (● = data, — = calculation).

IV. Data Analysis and Decay Scheme

The decay scheme for ^{83}As was developed primarily from the coincidence data. The singles data were used to establish energies and intensities, frequently with the aid of the coincidence data. The decay scheme arguments are presented in three Tables: IV.1, the coincidences observed for ^{83}As decay; IV.2, level justification; and IV.3, transition placement. The growth and decay experiment is evaluated to determine the β^- intensity to the ^{83}Se^m state, which gives the spin and parity of the ^{83}As ground state. The arguments for assigning spin and parity are given.

Table IV.1. Coincidences used in constructing the ^{83}As decay scheme. Tabulated are the coincidence spectra (Gate) and the peaks therein labeled by their energies in keV. The notes are at the end of the table, indicating the nuclide(s) to which the coincidence is assigned. The question marks indicate either that the coincidence was not assigned to any decay or that it is assigned but not placed in the decay scheme.

Gate	Peak Energy
192	311a, 371a, 435i, 465?, 518a, 544?, 560a, 580a, 780i, 817?, 932a, 1243a
229	743i, 798f?, 1296a, 1453a, 1665?, 1689?, 1849?, 1975?
311	372a, 423a, 509w, 560a, 733a?, 933a, 1081?, 1126a, 1537a, 1597a, 1556?, 1780a, 1896?, 2140?, 2431a, 2639a, 2742a
373	312a, 518a, 560a, 582a, 604?, 944?, 1408a
381	582a, 1112a, 1198?, 1895a, 2837?
395	735a, 1331a, 1519a
398	1331a, 1519a?
44f	313?, 582a, 655b?, 675f?, 682a, 755b, 1170a, 1228?, 1265a, 1895b, 2355b
480	656?
491	216?, 316?, 1058a, 1159a, 1331a, 1687d, 1842d, 1956?
518	372a, 510?w, 582a, 610a, 808a, 978a?, 1258a?, 1378a, 1622a, 1780a, 1975?
548	186?, 247?, 529?, 581?, 655b, 802a, 819b, 1527a, 1896b
550	186?, 530?, 802?, 819?, 1402?, 1527a, 1650?, 1731b?, 1896b?
561	312a, 344b, 372a, 511?, 636?, 655b, 819b, 907?, 1012?, 1076b, 1080b, 1115?, 1159?, 1280?, 1386?, 1487?, 1623?, 1693?, 1731b, 1741?, 1780a, 1896b, 2240?
582	307?, 372a, 381a, 446a, 491a, 518a, 613a, 667e?, 682a, 691a, 749a, 808a, 821?, 1058a, 1083a, 925?, 1083a, 1128a, 1151a, 1169a, 1258?, 1607a, 1623a, 1780a, 1859?, 1870?, 1900a, 2142a, 2299a, 2388a, 2586a, 2700a, 2881a, 3245a
603	654?, 804?, 833?, 1077?
609	344?, 357?, 636?, 1113?
682	446a, 582a, 1002?, 1169a, 1219?, 1715a
690	582a, 1607?, 2191?
734	398a, 511w, 781a, 804a, 873y, 896y, 904a, 915a, 947?, 980a, 1113a, 1181a, 1256a, 1283?, 1296?, 1384x, 1406x, 1519a, 1581a, 1692y, 1761a, 1807y, 1895a, 1917a, 2018a, 2205a, 2280a, 2319a, 2370a, 2424a, 2460a, 2729a, 3038a, 2865a
745	749a, 781a, 803a, 835?, 1331a
781	193i, 735a, 746a, 834a, 1014a, 1113a, 1331a, 1679?, 2077a
803	510?, 735a, 746a, 834a, 1014a, 1055y, 1113a, 1331a, 1565x, 1732b, 2078a
833	357f, 457?, 468?, 510?, 524?, 574?, 666?, 718f, 781a, 803a, 813?, 897y, 904a, 1014a, 1074a, 1144a, 1169?, 1196y, 1287x, 1419a, 1616a, 1795a, 1818a, 1919a, 2105a, 2180a, 2220a, 2271a, 2360a?, 2628a
872	344b, 655b, 736a
904	175?, 654b, 735a, 818b, 1014a, 1079?, 1113a, 1731b, 1896b, 2078a
917	654?, 734a, 980a, 1944a
933	311a, 423?, 653?, 1332?, 1389?, 1527?
974	518a, 697?, 735a, 915a, 1454?, 1616?
980	735a, 1454?
1014	344b?, 654b?, 780a, 803a, 835a, 1731b?
1057	491a, 511?w, 997f, 1311?x, 1330a, 1457?, 1526?, 1634?, 1823a
1077	344b, 510?, 560b, 655b, 734?, 799?, 819?, 834a, 1114a?, 1144?, 1540?, 2516?, 2592?, 2607?, 3115?
1080	344b, 511w, 560b, 583a, 615?, 655b, 734?, 815b, 1110b, 1159ba, 1365?, 1409?, 1504a?, 1541b, 1551b, 1618a?, 1721?, 1811b, 1981?, 2026b, 235e?, 2464?, 2701?, 2923?, 2938?, 3387?, 3509b
1113	469?, 511w, 532?, 609?, 655b, 6..7e?, 735a, 781a, 803a, 904a, 1080ba, 1255?, 1454e?, 1731b, 1811?
1127	582a, 1169a
1150	655?, 1331a
1159	491a, 560b, 655b, 1080b, 1822a
1168	343b, 446a, 511w, 518a, 560a, 582a, 654b, 682a, 850?, 872?, 923?, 967?, 1013?, 1110?, 1127a, 2978?
1195	344b, 655b, 819b, 1730b, 1896b
1244	343?, 511?w, 667?, 1455e?

Table IV.1. (Continued.)

Gate	Peak Energy
1296	230a, 510w, 1331a, 1453a
1331	491a, 655?, 746a, 781a?, 804a, 819b?, 1058a?, 1151a, 1159a, 1527a, 1549a, 1650a, 1912a, 2001a, 2092a
1384	343bx, 655bx, 734ax
1406	734a
1409	655b, 1080b
1420	324?, 343?, 817?, 835a, 1823a, 1972?
1455	510w, 578e, 667e, 741e, 878e?, 984e?, 1007e, 1110e, 1175e, 1245e, 1287e, 1297a, 1317?, 1426?, 1527a, 1569?, 1672?, 1725?, 1751?, 1844e?, 2088e?, 3041e?
1518	398a, 685a, 735a, 760a
1527	423?, 550a, 654?, 929?, 1080?, 1331a, 1454a
1550	582a, 655b, 735a, 749a, 1080b, 1331a
1581	655b, 734a, 1080b, 1455e
1616	834ah, 519?, 654b?, 1454e?, 1971b?
1624	518a, 582a
1650	582a, 655b?, 749a, 1331a
1762	344b, 655b, 735a, 819b, 1730b?, 1896b?
1780	311a?, 518a, 560a, 582a
1795	834a
1822	784a?, 1058a, 1159a, 1420a?, 1731b?
1896	344b, 448b?, 512?w, 561b, 607?, 655b, 735a, 799f, 904b, 998f, 1185b, 1197b, 1541b, 1763b
1909	1144?, 1196?
1917	655b?, 735a, 834a
1942	655b?, 735a?
2018	735a
2077	781a, 803a, 819?, 904a, 1255a, 1732?
2094	1331a?, 1731b?
2105	468d, 654b?, 834a, 1077b?, 1731b?
2142	311a, 583a, 654b, 1730b?
2202	380a?, 618?, 735a
2220	654b, 833a
2281	735a
2299	582a
2319	655b, 735a, 815b?, 1080b, 1731b?, 1971b?
2370	735a
2425	735a
2456	654b, 734a
2587	582a, 654b
2698	583a, 654b, 1080b
2725	654b, 735a, 1453?
2937	654b, 1080b
2981	654b
3037	667e, 1454e

a) ^{83}As
b) ^{82}As
c) ^{80}As
d) ^{81}As
e) ^{84}As
f) ^{83}Se
g) ^{84}Se
h) ^{85}Se
i) ^{130}Sn
j) ^{131}Sn
k) ^{132}Sn
m) ^{132}Sb
?) Uncertain.
w) Annihilation radiation.
x) Single escape peak.
y) Double escape peak.

Table IV.2. In this table the basis for establishing each level is given. See the text for an explanation of the notation used in this table.

Energy	Basis
0	Ground state. (a)
228.9	I observe C(2077=803), C(1331=745=803), C(734=1113=803), and C(834=1013=803). Further the 781-keV gamma can be substituted for the 803-keV gamma and the same observations hold. These transitions are all intense, with the more intense transitions being placed lower in the decay scheme. I determined that the 803- and 781-keV transitions feed a level at 2077 keV and the other transitions cascade down from this level. These relationships established the levels at 229, 964, 1063, 1331, 2077, 2858, and 2881 keV. The 229- and 1331-keV levels have been observed in ^{82}Se($\vec{d}$,p)^{83}Se. (a)
540.3	I observe coincidences C(311=560=372), C(311=932) and C(582=518=372). These establish levels at 540, 582, 1101 and 1473 keV. The 582-keV transition is more intense than the 518-keV transition. Similarly, the 311-keV transition is stronger than the 560-keV transition after the correction is made for 560-keV intensity in ^{82}As. This assignment was confirmed by the 932-keV crossover to the 560- and 372-keV pair. The 540-, 582- and 1100-keV levels were seen in the ($\vec{d}$,p) work. (a)
582.4	See discussion for the 540-keV level. (a)
963.6	See discussion for the 229-keV level.
1063.0	See discussion for the 229-keV level.
1100.6	See discussion for the 540-keV level. (a)
1265.3	This level is established from the C(582=682=446). One half of I(446) is assigned to ^{82}As from the 446-keV coincidence gate, making I(682) > I(446) in ^{83}As. Also I observe C(1265=446), the ground state transition. (a)
1296.2	The 1297- and 1527-keV levels are placed on the following coincidences: C(1297=230=550), C(1297=1331), C(1297=230=1454), C(1527=550=803), C(1527=1331), C(1527=1454), and C(230=1331). The 1527-keV gamma is then the crossover to the 1297-230 cascade, which yields a new level, since there were no observed coincidences through the 229-keV level. The coincidences with 550-, 1331-, and 1454-keV gammas connect with existing levels in ^{83}Se and, in addition, the 803-keV gamma was already placed in ^{83}Se. Most of these transitions can be placed in at least one other decay that could be present in my sample (i.e., $^{130\text{-}133}$Sb, $^{130\text{-}132}$Sn, ^{83,85}Se). However, the only corrections necessary were to the 230-keV transition for ^{83}Se, to the 550-keV transition for ^{82}As, and to the 1454- and 1527-keV transitions for ^{84}As.
1331.2	See discussion for the 229-keV level. (a)
1473.2	See discussion for the 540-keV level. (a)
1526.4	See discussion for the 1297-keV level.
1665.3	This level is based on the C(582=1083) coincidence. (a)
1710.2	See discussion for the 1265-keV level.
1822.5	The C(1822=1057) and C(1331=491=1057) coincidences establish this level.
1907.9	This level is established from C(518<807), C(560<807), and C(582<807).
1943.6	This level is established by C(734=980=914) and C(1944=914) coincidences.
2077.0	See discussion for the 229-keV level.
2137.7	This level is placed from the C(834=1074) coincidence and the 1908-keV transition to the 229-keV level. Also I observed C(834<1144), C(834<1196), C(1077<1144), C(1077<1196), C(1908<1144) and C(1908<1196). The 1144- and 1196-keV transitions connect to separately established levels.
2190.6	This level is placed on the basis of C(582=690), C(582<1607), C(690<1607), and C(690<2190).
2482.3	I based this level on C(734=1518). (a)
2545.9	I observed the C(734=1581). Also, a level was observed at 2535-keV in the ($\vec{d}$,p) work. (a)
2679.2	The C(834=1615) places this level.
2724.6	This level is placed on the C(734=1760) and C(582=518=1623).
2858.1	I observe the C(734=1895) coincidence, which established this level in ^{83}Se. All other coincidences with the 1895-keV gamma were assigned to ^{82}As.
2880.7	This level is assigned on the strength of the C(734=1917) coincidence. The only other coincidence with the 1917-keV gamma was the 834-keV transition, which is used in establishing the 2981-keV level.

Table IV.2. (Continued.)

Energy	Basis
2971.1	This level is placed on C(311+2431) and C(582+2389).
2981.1	This level is placed on the basis of C(1331 + 1649), C(734 + 2018) and C(834 + 1918).
3167.5	This level is placed on the C(734 + 2204) since the 2204-keV gate has no other significant peaks.
3242.9	This level is established on C(734 + 2281) and C(1822 + 1420).
3282.0	This level is established from C(734 + 2320) and C(834 + 2220) coincidences.
3333.8	This level is placed on C(734 + 2370).
3386.7	This level is established from the C(734 + 2424) coincidence.
3424.0	This level is established from the C(734 + 2460) and C(1331 + 2092) coincidences.
3463.8	This level is placed on C(582+2881).
3558.6	This level is established from C(582+2975).
3690.2	This level is established from the C(734 + 2729) coincidence.
3911.2	This level is established from C(1331+2580).
4001.6	This level is established from C(734 + 3038).

(a) Observed in the $^{82}Se(\vec{d},p)^{83}Se$ experiment (MON78).

Table IV.3. Placement of gamma transitions in the decay of ^{83}As. The energy, uncertainty, relative intensity (I(734) = 1000), uncertainty, initial level and final level are given. The notation C(...) is the same as before. Energies are in keV. Intensities are from the singles data unless otherwise specified. (For references to levels, see Table IV.2.)

Energy	Error	Intensity	Error	Initial	Final
42	2.0	0.005	100%	582	540
	C(311 + 518)				
135.8	3.0	0.2	100%	1101	964
	C(734 + 1780)				
157.2	1.3	0.9	100%	1822	1665
	C(1082 + 1058)				
165.3	1.2	0.1	120%	1265	1101
	C(518 + 446) requires				
192.0	2.0	0.7	120%	1665	1473
	C(192 + 372), C(192 + 817)				
195	2.0	1.0	80%	1526	1331
	upper limit.				
207	2.0	0.3	100%	1473	1265
	upper limit.				
230.0	0.2	10.0	10%	1526	1296
	C(1296 + 230 = 1454), see discussion for level 1296.				
231	2.0	0.3	100%	1331	1101
	upper limit.				
268.0	2.0	0.2	78%	1331	1063
	in 834 gate and singles.				
296	2.0	0.5	100%	1822	1526
	upper limit.				
311.5	0.1	30.7	3%	540	229
	see discussion for level 540.				
333.2	0.6	0.3	80%	1665	1331
	singles fit, upper limit.				
350	2.0	0.3	100%	1822	1973
	upper limit.				

Table IV.3. (Continued.)

Energy	Error	Intensity	Error	Initial	Final
367.5	2.0	0.6	80%	1331	964
	in 734 gate and singles, corrected for ^{131}Sn.				
372.6	0.1	4.4	10%	1473	1101
	see discussion for level 1472.				
380.7	0.8	0.4	72%	964	582
	C(582=380) and 1113-keV peak in 582- and 380-gates.				
397.8	0.1	2.5	13%	2881	2482
	C(734=1518=398)				
400	2.0	0.2	100%	1665	1265
	upper limit.				
411.8	1.1	1.9	40%	2077	1665
	upper limit from singles.				
423.0	2.0	0.3	197%	964	540
	singles fit only.				
445.6	0.2	6.6	4%	1710	1265
	C(582=682=446), see discussion for level 1710.				
480.0	2.0	0.2	60%	1063	582
	C(582=480) upper limit from coincidence.				
491.2	0.1	8.1	5%	1822	1331
	C(1331=491=1058), see discussion for level 1822.				
518.2	0.1	34.3	6%	1101	582
	C(582=518=372), see discussion for level 1100.				
526	2.0	0.4	100%	1822	1296
	upper limit.				
549.8	0.2	3.4	10%	2077	1526
	C(1527 550 803), see discussion for level 1527 intensity from ratio I(1527)/I(1895) in 550-kev gate. Also in ^{82}As.				
557	2.0	0.1	100%	1822	1265
	upper limit.				
560.6	0.1	10.0	10%	1101	540
	C(311 560 372), see discussion for level 1100, intensity from ratio I(311)/I(343) in 560 gate, also ^{82}As.				
565	2.0	0.1	100%	1665	1101
	upper limit.				
582.4	0.1	108.8	2%	582	0
	C(582 518 372), see discussion for level 582.				
601	2.0	0.2	100%	1665	1063
	upper limit.				
609.7	0.1	0.5	65%	1710	1101
	C(518 609)				
648	2.0	0.2	100%	1710	1063
	upper limit.				
682.9	0.1	12.3	7%	1265	582
	see discussion for level 1265.				
685.0	2.0	2.5	30%	3168	2482
	C(734 1518 685)				
690.8	0.2	2.7	12%	2881	2189
	C(582 690) 1607 peak in 582 and 690 gate.				
702.1	1.6	0.7	100%	1665	964
	in 734 gate, fits to known level, upper limit, corrected for ^{131}Sn.				
722	2.0	0.3	100%	1822	1101
	upper limit.				

Table IV.3. (Continued.)

Energy	Error	Intensity	Error	Initial	Final
734.9	0.1	1000.0	1%	964	229
	see discussion for level 963.				
745.4	0.1	29.2	20%	2077	1331
	C(1331 = 745 = 803)				
747	2.0	0.2	100%	1710	964
	upper limit.				
748.8	0.2	12.3	20%	1331	582
	C(582 = 748 = 1549)				
759	2.0	0.3	100%	1822	1063
	upper limit.				
760.6	1.5	1.4	40%	3243	2482
	C(1518 – 761)				
781.1	0.1	32.3	7%	2858	2077
	C(734 = 1113 = 781), C(2077 = 781)				
791.0	1.0	0.4	80%	1331	540
	in 311 gate, fits with 1331 level, but 311 not in 790 gate.				
803.8	0.1	92.8	2%	2881	2077
	C(734 = 1113 = 781),C(2077 = 803)				
806.0	1.0	3.1	50%	2138	1331
	C(1331 = 806), 803 and 806 peak 1 channel wider in 1331 gate than in 745 gate.				
807.5	0.3	2.5	30%	1908	1101
	C(518 < 807) and singles, fits, no 807 gate.				
812.0	2.0	0.3	125%	2077	1265
	C(682 < 813) and C(803 < 812)				
817.2	3	2.7	52%	2482	1665
	C(1083 < 817), not the 818 from ^{82}As.				
834.1	0.1	199.9	1%	1063	229
	C(834 = 1013 = 803), see discussion for level 1063.				
845.0	1.5	1.0	50%	1908	1063
	C(834 < 845) and singles.				
871.0	1.5	1.5	80%	1101	229
	C(1780 - 871) corrected for 1896 double escape.				
891	2.0	0.3		1473	582
	upper limit.				
904.0	0.1	2.9	6%	2981	2077
	C(734 = 1113 = 904)				
914.5	0.1	5.3	8%	2858	1944
	C(734 = 980 = 914)				
933.1	0.2	3.7	11%	1473	540
	C(311 = 933)				
944.0	0.3	1.8	100%	1908	964
	C(734 < 944) and singles, but half-life is wrong so this is an upper limit.				
979.8	0.1	7.3	5%	1944	964
	C(734 = 980 = 914), see discussion for level 1944.				
1010.0	2.0	1.0	100%	2482	1473
	C(372 < 1010)				
1014.0	0.1	60.6	2%	2077	1063
	C(834 = 1013 = 803), see discussion for level 2077.				
1036.8	2.0	0.5	100%	2138	1101
	C(518 < 1037) singles, upper limit.				
1036.8	2.0	1.0	60%	2981	1944
	C(979 < 1037) upper limit.				

Table IV.3. (Continued.)

Energy	Error	Intensity	Error	Initial	Final
1058.2	0.1	77.1	2%	2881	1822
	C(1822 = 1058), C(1331 = 491 = 1058), see discussion for level 1822.				
1074.0	0.7	15.0	15%	2138	1063
	C(834 = 1074), see discussion for level 2137.				
1082.9	0.5	7.1	20%	1665	582
	C(582 = 1083), see discussion for level 1665.				
1113.4	0.1	360.9	3%	2077	964
	C(734 = 1113 = 803), see discussion for level 2077.				
1125.0	0.3	2.8	20%	1665	540
	C(311 = 1125)				
1127.8	0.1	9.7	8%	1710	582
	C(582 = 1128 = 1169) and C(582 = 682 = 446 = 1169)				
1143.6	0.3	2.3	25%	3282	2138
	C(1908 = 1144), corrected for ^{131}Sn.				
1151.1	0.4	6.0	8%	2482	1331
	C(1331 = 1150)				
1158.7	0.1	13.1	15%	2981	1822
	C(1822 = 1159), C(1331 = 491 = 1159)				
1169.3	0.1	14.3	6%	2881	1710
	C(582 = 1127 = 1169)				
1196.0	0.6	1.4	22%	3334	2138
	C(1907 = 1196), corrected for ^{82}As.				
1218.9	1.0	0.7	80%	2482	1265
	C(682 - 1218) and singles.				
1240.0	0.5	0.8	50%	1822	582
	C(582 = 1240) to fit with 1822 level upper limit.				
1243.0	1.0	1.0	80%	1473	229
	C(1243 = 1859), coincidence limits.				
1257.0	0.2	2.3	18%	3334	2077
	C(734 = 1113 = 1257)				
1258.0	2.1	1.9	25%	3168	1908
	C(582 = 518 = 1258) and 807 in all of these, intensity from coincidence.				
1265.1	0.5	0.9	35%	1265	0
	C(446 - 1265), intensity from singles.				
1296.2	0.1	12.4	5%	1296	0
	C(1296 = 230 = 1454), see discussion for levels 1527 and 1296.				
1326.8	1.0	1.5	50%	1908	582
	C(582 - 1327) upper limit from coincidence.				
1331.1	0.3	14.1	7%	2858	1526
	C(1527 = 1331), C(1297 = 230 = 1331), and 1331 goes to existing level.				
1331.2	0.1	136.9	3%	1331	0
	see discussion for level 1331.				
1367.0	1.1	0.1	100%	1908	540
	upper limit to possible transition from singles.				
1381.2	1.0	2.0	50%	2482	1101
	C(582 - 1381) and C(518 < 1381)				
1408.0	2.0	2.0	100%	2881	1473
	C(372 - 1408) and singles.				
1419.5	0.2	2.3	15%	2482	1063
	C(834 = 1420)				
1420.0	1.0	2.3	15%	3243	1822
	C(1822 - 1420), intensity split on 1420 gate.				

Table IV.3. (Continued.)

Energy	Error	Intensity	Error	Initial	Final
1454.7	0.3	52.5	6%	2981	1526
	C(1527 - 1455) and C(1296 = 230 = 1454), see discussion for level 1527.				
1480.7	0.3	2.7	18%	1710	229
	from singles only; upper limit; also ^{131}Sn.				
1518.4	0.1	25.7	4%	2482	964
	C(734 = 1518), see discussion for level 2482.				
1526.4	0.1	81.1	4%	1526	0
	C(1527 = 1454), see discussion for level 1527.				
1537.2	1.6	2.2	37%	2077	540
	C(311 - 1537) is definite, but there is no 803-keV coincidence. Placement is tentative, may belong to ^{82}As.				
1548.8	0.1	30.7	4%	2881	1331
	C(582 = 748 - 1548) and C(1331 = 1548)				
1582.3	0.2	3.0	17%	2546	964
	C(734 = 1582)				
1596.6	0.8	0.9	42%	2138	540
	C(311 - 1597), singles, fits to this level.				
1607.0	1.5	1.0	70%	2191	582
	C(582 = 1607), see discussion for level 2189.				
1615.5	0.1	22.7	3%	2679	1063
	C(834 - 1615)				
1623.6	0.4	4.0	10%	2725	1101
	C(582 - 518 - 1624)				
1641.0	0.4	0.2	100%	2971	1331
	singles fit only.				
1649.2	0.1	22.0	3%	2981	1331
	C(1331 = 1649)				
1664.6	0.3	1.8	20%	1665	0
	singles only. coincidence with 654 takes 60% of intensity to ^{82}As.				
1715.6	0.5	0.8	35%	2981	1265
	C(582 · 1715) C(682 < 1715)				
1761.4	0.1	7.3	5%	2725	964
	C(734 = 1761), corrected for ^{82}As, intensity assignment from 1761 gate.				
1780.2	0.1	16.2	4%	2881	1101
	C(582 = 518 = 1780)				
1795.3	0.1	19.9	5%	2858	1063
	C(834 - 1795)				
1818.0	0.2	6.1	10%	2881	1063
	in 834 gate and singles, intensity from coincidence.				
1822.5	0.1	81.7	2%	1822	0
	C(1822 = 1057), see discussion for level 1822.				
1860.0	*0.3*	*1.7*	*60%*	*3334*	*1473*
	C(372 - 1860)				
1894.8	0.2	123.1	2%	2858	964
	C(734 = 1895), also in ^{82}As C(654 = 1895 = 343 = 560), intensity is from I(654)/I(734) in 1895 gate, energy corrected for difference between 1895 energies in 654 and 734 gates.				
1900.3	0.5	1.9	50%	2482	582
	C(582 · 1900), and singles.				
1908.9	0.1	19.9	6%	2138	229
	C(1908 = 1144), C(1908 = 1196), not placed from 1908 level because gammas feeding 1908 level are not in coincidence.				
1912.0	1.0	0.5	80%	3243	1331
	C(1331 < 1912), intensity from coincidence.				

Table IV.3. (Continued.)

Energy	Error	Intensity	Error	Initial	Final
1917.3	0.1	129.1	3%	2881	964
	C(734 = 1917) and C(834 = 1919), split from 1917 gate.				
1919.3	0.5	7.0	20%	2981	1063
	see above 1917 gamma-ray.				
1944.0	0.5	1.4	50%	1944	0
	in 914 gate, see discussion for level 1944.				
2001.0	1.0	1.2	80%	3334	1331
	C(734 = 2001)				
2017.9	0.1	12.7	8%	2981	964
	C(734 = 2018)				
2077.0	0.1	249.5	2%	2077	0
	C(2078 = 803), see discussion for level 2077.				
2092.0	1.0	1.4	20%	3424	1331
	C(1331 = 2092)				
2098.3	1.2	0.9	80%	2679	582
	C(582 < 2098)				
2104.2	0.2	3.7	10%	3168	1063
	C(834 = 2105)				
2141.7	0.3	2.9	20%	2679	540
	C(311 = 2141), no 518, intensity assignments from coincidence.				
2142.5	0.7	0.7	50%	2725	582
	C(582 = 2142), no 518, intensity assignments from coincidence.				
2180.3	1.9	0.3	100%	3243	1063
	C(834 < 2180) and singles.				
2190.6	0.7	1.1	73%	2191	0
	see discussion for level 2191.				
2204.6	0.1	213.4	1%	3168	964
	C(734 = 2205), see discussion for level 3168.				
2218.7	0.2	14.4	11%	3282	1063
	C(834 = 2220)				
2270.8	0.5	1.5	29%	3334	1063
	C(834 < 2272), and singles.				
2279.9	0.1	5.6	8%	3243	964
	C(734 = 2281)				
2299.2	0.1	8.9	6%	2881	582
	C(582 = 2300)				
2318.8	0.1	25.2	2%	3282	964
	C(734 = 2319) and 5% in ^{82}As from coincidence.				
2360.0	1.0	0.7	50%	3424	1063
	C(834 < 2360) and singles.				
2370.4	0.1	11.4	5%	3334	964
	C(734 = 2372)				
2388.3	0.9	2.3	20%	2971	582
	C(582 < 2388)				
2423.1	0.3	5.8	12%	3387	964
	C(734 = 2424)				
2429.5	0.5	2.9	18%	2971	540
	C(311 < 2432) and singles.				
2449.9	0.2	9.7	8%	2679	229
	fits from singles, 2450 coincidence with ^{82}As much less than singles.				
2461.9	1.0	2.5	15%	3424	964
	C(734 – 2462), energy and intensity from coincidence.				

Table IV.3. (Continued.)

Energy	Error	Intensity	Error	Initial	Final
2580.0	2.0	2.0	100%	3911	1331
	C(1331 - 2580) and singles.				
2585.2	0.1	1.7	20%	3168	582
	C(582 - 2585)				
2626.7	0.5	1.1	22%	3690	1063
	C(834 - 2628), intensity split based on coincidence.				
2629.0	1.5	0.3	70%	3168	540
	C(311 - 2629)				
2699.6	0.1	5.2	5%	3282	582
	C(582 - 2700)				
2724.6	0.1	1.8	35%	2725	0
	singles only. Intensity corrected for ^{84}As and ^{82}As from coincidence.				
2729.0	1.5	6.7	10%	3690	964
	C(734 - 2729) energy and intensity from coincidence.				
2742.5	0.2	4.4	10%	3282	540
	C(311 - 2742)				
2858.1	0.1	170.0	2%	2858	0
	singles and half-life, corrected for small ^{82}As component.				
2865.0	1.2	0.7	100%	3828	964
	C(734 - 2865)				
2881.4	1.0	1.1	50%	3464	582
	C(582 - 2881)				
2937.9	0.1	6.6	15%	3168	229
	singles and half-life.				
2976.2					
2981.2	0.5	15.4	4%	2981	0
	singles and half-life.				
3038.0	1.1	2.1	197%	4001	964
	C(735 - 3038)				
3242.8	0.1	35.1	2%	3243	0
	singles fit.				
3245.0	1.0	0.5	100%	3828	582
	C(582 - 3245)				

Throughout this section, shorthand notation is used in an effort to make the explanation as concise and clear as possible. The notation "C(a<b)" means that there was a peak at energy b in coincidence spectrum a, but the reverse situation was not true. The notation "C(a=b)" means that C(a<b) and C(b<a) were both true, the exclusion not holding. Expanding, C(a=b=c) means that the above is true for all pairs. The notation "C(a=b=c) and C(a=b=d)" implies that c and d do not fit "C(c=d)". The notation I(a) means the intensity of the gamma-ray transition, a, which will be an energy in keV followed by any additional information necessary.

Levels have been established only on the basis of coincidence data and half-life information. Transitions which appeared only in the singles data were placed, based on energy and half-life, between previously established levels only. This procedure was followed to cope with the three major levels (^{82}Se, ground state, ^{83}Se, ground state, and ^{83}Se^{m}, 1/2^{-} 229-keV state) which gave no coincidences. Examples are the 2858- and the 1908-keV transitions. The 2858-keV transition was placed from the 2858-keV level in ^{83}Se since this was the only place it would fit. On the basis of its energy, the 1908-keV transition depopulates either the 1908- or 2137-keV level in ^{83}Se. Based on its weak, but definite, coincidences it was placed from the 2137-keV level.

In most instances, energies and intensities were determined from the singles data. However, multiplets frequently required the use of the coincidence data to resolve these values. The 1895-keV multiplet is a good example of the procedure used for multiplets.

Using the coincidence data, the 1895-keV transition was placed feeding the 654-keV level in ^{82}Se, in coincidence with the 654-keV gamma ray, and feeding the 963-keV level in ^{83}Se, in coincidence with the 734-keV gamma ray. From data in the "Table of Isotopes" (TOI78), and my coincidence data, it was also placed in the decay of ^{83}Se^{g} feeding the 779-keV level in ^{83}Br, in coincidence with the 779-keV gamma ray. The intensity of this portion of the 1895-keV multiplet was obtained by normalizing the 718-keV gamma ray from ^{83}Se^{g} decay to the singles data. This gave I(1895, ^{83}Se^{g}) = 1.2% (4%) of I(1895,total) when corrected for decay effects. (There is also a contribution from ^{131}Sn decay of 0.001% of the multiplet intensity which was ignored.) The remaining intensity assigned to the two arsenic decays was I(1895)=2.828E6. This intensity was split between the two arsenic decays based on I(654)=7156 (2%) and I(734)=3442 (3%) in the 1895-keV coincidence gate, giving the intensity as

$$I(1895,^{83}\mathrm{As}) = \frac{I(734)}{I(734) + I(654)}\, I(1895) = 9.19\mathrm{E}5\ (4\%) \quad . \tag{IV.1}$$

The energies were established from the energy difference of the 1895-keV peak in the 654- and 734-keV gates, which was 0.9 ± 0.2 keV. From the energies of the two components of the multiplet, the energy of the multiplet is

$$E_m = \frac{I_2 E_2 + I_3 E_3}{I_2 + I_3} \tag{IV.2}$$

and

$$E_2 = E_3 + 0.9\ \mathrm{keV} \quad , \tag{IV.3}$$

where subscripts m, 2, and 3 refer to the multiplet, ^{82}As and ^{83}As respectively. The value for E_m is 1895.4 ± 0.1 keV and the intensities are known; solving for E_3 gives:

$$E_3 = E_m - \frac{I_2}{I_2 + I_3} - 0.9 = 1894.8 \pm 0.3 \quad . \tag{IV.4}$$

Upper limits on low-intensity transitions were necessary for comparison to the model being investigated. These were evaluated primarily from the coincidence data, with support from the singles data when they were consistent. The usual method was to look for the specific photopeak in the appropriate gates and then establish an uncertainty. Frequently, however, the background made the uncertainty unreasonably large. This was true for the 137-keV transition between the 1100-keV 3/2$^+$ level and the 963-keV 3/2$^-$ level. The background at 137 keV was large in the 734-keV gate. An alternative procedure was to use the possible coincidence between the 734-keV gamma ray and the 1780-keV gamma ray which feeds the 1100-keV level. In the 1780-keV gate the background at 734 keV is approximately 2 counts/channel, which allowed the 137-keV transition intensity to be set at 0.6% of the 518-keV transition intensity. The 157-keV transition between the levels at 1822 and 1665 keV was evaluated in much the same manner. Here, the 1082- and 582-keV transitions appear in the 1057-keV gate and the 582-keV transition appears in the 1158-keV gate. Previously, these transitions had been definitively placed, the 1082-keV transition depopulating the 1665-keV level and the 1058- and 1158-keV transitions populating the 1822-keV level. These coincidences showed the existence of the 157-keV transition connecting these two levels.

To use the beta transition intensity in deducing the spin and parity of the levels in ^{83}Se, it was necessary to determine the intensity of the *M*4 transition from the first 1/2$^-$ level in ^{83}Se and the beta intensity to this level.

The transition intensity from the 1/2$^-$ 230-keV level to the 9/2$^+$ ground state can be estimated from the systematic trend of the reduced transition probability of this *M*4 transition

(B($M4$)) in ^{89}Zr, ^{87}Sr, and ^{85}Kr where its intensity has been measured. The gamma-ray transition half-life is calculated from the total half-life:

$$\tau_\gamma = (1 + \alpha) \times \tau_T / I_t \quad , \tag{IV.5}$$

where τ_γ and τ_T are the gamma-ray and total half-lives, α is the total $M4$ internal conversion coefficient, and I_t is the absolute transition intensity for gamma-ray plus internal conversion. The Weisskopf estimate of the half-life for an $M4$ transition (NDS80b) is

$$\tau_{sp} = \frac{4.84E4}{E^9 A^2} \text{ s} \quad . \tag{IV.6}$$

The reduced transition probability in single particle units for this transition is

$$B(M4) = \tau_{sp}/\tau_\gamma \quad . \tag{IV.7}$$

In Table IV.4, I present the results of this procedure and use it to obtain an estimate of the $M4$ transition intensity in ^{83}Se. I obtain an isomeric transition intensity in ^{83}Se of 0.008% so that I will be justified in ignoring this transition.

Spin and Parity of ^{83}As Ground State

The intensity of the beta transition from ^{83}As to the first $1/2^-$ level in ^{83}Se can provide evidence for the correct ground state spin and parity of ^{83}As, but this intensity is unknown. However, it is known that $^{73-81}$As have ground state spin and parity $3/2^-$ and those which decay to selenium have a strong branch to the first $1/2^-$ level, as expected. The β^- intensities for decay to the first $1/2^-$ state in selenium are given in Table IV.5.

To determine the beta transition intensity I performed a careful growth and decay experiment. Multichannel multiscaled gamma-ray data was accumulated from each of 55 samples for 11 min in 20 time planes, as detailed in Table IV.6. This was enough time to follow the activity of the most intense gamma rays of both ^{83}As and ^{83}Se^m to extinction.

In Fig. IV.1, I show schematically the decays from ^{83}As and ^{83}Se that must be followed in this measurement. Absolute gamma-ray and beta intensities (TOI78) were known for the decay of ^{83}Se^m. By taking the difference of the gamma-ray intensity populating and the beta intensity (as measured by the gamma-ray intensity) depopulating the ^{83}Se^m level, I determined the beta intensity populating that level.

The photopeak amplitudes were extracted with the program FITEK, as described earlier. The amplitudes for the 391-keV ^{113}Sn (used for dead time corrections), 734-keV ^{83}As, and 674-, 988-, 1030-, and 2051-keV ^{83}Se^m photopeaks are shown in Table IV.6 for all of the time planes. The long-lived components of the 988- and 1030-keV photopeaks were determined to be from ^{132}Sb (the daughter of ^{132}Sn) and ^{89}Rb decay, respectively. These activities were identified and corrections made based on photopeak intensities, energies, and half-lives in the nineteenth and twentieth planes. Additionally, the antimony was anticipated from the presence of ^{132}Sn in all of my other arsenic spectra.

The intensity of the gamma rays used was compared to calculated decay curves to verify that the gamma rays had the correct half-life. This was done by dividing the observed number of counts by the calculated fraction that should have decayed in the given plane. The results of this analysis for the 674- and 988-keV gamma rays are shown in Figs. IV.2a and IV.2b. The values are computed assuming half-lives of 65, 70, and 75 s. (The correct half-life has been measured as 70.4 s (MEY81).) The effect of a long-lived contaminant is evident in the 988-keV gamma ray. In the present work, the 734-keV gamma ray shows a 12.4-s half-life and this value was used in these calculations.

Table IV.4. Values for the half-life, gamma-ray energy (E_γ), gamma-ray intensity (I_γ), and internal conversion coefficient (ICC) used in evaluating the systematic behavior of the B($M4$) in some N=49 nuclei. The trend in the B($M4$) was established using the first three nuclei and the B($M4$) for ^{83}Se was estimated and the gamma half-life and gamma branching ratio calculated. The values I calculated are given in parentheses.

	Nuclide			
	^{89}Zr	^{87}Sr	^{85}Kr	^{83}Se
Half-life[a]	4.18 min	2.80 h	4.48 h	70 s
E_γ (keV)[a]	588	389	305	229
I_γ (%)[a,b]	93.8	99.7	21	(0.01)
ICC[c]	2.88	2.36	1.93	1.56
Gamma half-life (s)	1.04E3	3.40E4	2.25E5	(2.22E6)
T_{sp} (s)[d]	3.17E3	1.37E5	1.28E6	1.77E7
B($M4$) (SPU)	3.06	4.03	5.69	(8.04)

[a] TOI78.

[b] Intensity of the isomeric transition, gamma plus internal conversion.

[c] ROS78.

[d] Weisskopf estimate.

Table IV.5. Values for selected beta branching intensities, $E_{\beta i}$, Q_β, and log($f_c t$) values for odd-mass arsenic. The beta transition of interest is from the arsenic ground state to the first $1/2^-$ state in the daughter selenium.

Isotope	E($1/2^-$) MeV	%-β	Half-life	Q_β MeV	log($f_0 t$)
^{77}As	0.0	97.5	38.8 h	0.69	5.7
^{79}As	0.096	95.0	9.0 min	2.2	5.2
^{81}As	0.0	67.0	33.0 s	3.75	5.2
^{83}As	0.23	0.3	13.0 s	5.46	7.9

Table IV.6. This table contains the raw data from the multichannel multiscaled data for the arsenic ground-state beta decay. The values given are the photopeak amplitudes and percent uncertainties from the program FITEK. The time values are the length of each plane and cumulative time to the end of the plane. Under each isotope heading are the energies of each photopeak for that isotope and the associated detector relative efficiency.

Plane number	Time s	^{113}Sn	^{83}As	^{83}Se^m			
		392	734	674	988	1030	2051
		–	2.2	2.4	1.7	1.7	0.9
1	0.2	416.4	–	–	–	–	–
	0.2	19.0					
2	0.4	737.7	666.0	–	–	–	–
	0.6	11.0	15.0				
3	0.5	1212.1	1020.0	–	–	–	–
	1.1	8.0	9.0				
4	0.5	1067.8	1018.0	–	–	–	–
	1.6	8.0	8.0				

Table IV.6. (Continued.)

Plane number	Time s	^{113}Sn	^{83}As	$^{83}Se^{m}$			
5	1.0	2110.5	2061.0	–	–	–	–
	2.6	6.0	7.0				
6	1.0	2444.0	2091.0	–	–	–	–
	3.6	6.0	7.0				
7	2.0	4830.0	3858.0	–	–	–	–
	5.6	5.0	4.0				
8	2.0	4612.0	3630.0	–	–	–	–
	7.6	6.0	4.0				
9	5.0	12342.0	7430.0	110.0	273.0	–	45.0
	12.6	7.0	3.0	87.0	23.0		78.0
10	5.0	12939.0	5605.0	217.0	356.0	276.1	74.0
	17.6	3.0	4.0	24.0	22.0	15.0	22.0
11	10.0	25452.0	7263.0	495.0	496.0	532.4	96.0
	27.6	2.0	2.6	18.0	10.0	10.0	25.0
12	10.0	26064.0	4338.0	549.0	493.0	581.1	154.0
	37.6	5.0	2.6	14.0	10.0	16.0	13.0
13	15.0	39449.0	3176.0	795.0	748.0	953.2	237.0
	52.6	1.5	5.0	9.0	8.0	7.1	10.0
14	15.0	39119.0	1369.0	798.0	616.0	861.9	184.0
	67.6	0.9	9.0	8.0	8.0	12.4	16.0
15	15.0	39552.0	639.0	692.0	468.0	718.0	185.0
	82.6	1.1	16.0	7.0	10.0	6.8	16.0
16	30.0	77429.0	208.0	1099.0	897.0	1340.2	300.0
	112.6	0.7	45.0	10.0	7.0	15.1	11.0
17	60.0	154076.0	298.0	1549.0	1259.0	1781.5	406.0
	172.6	1.1	20.0	7.0	6.0	13.2	10.0
18	120.0	316737.0	142.0	1192.0	1146.0	2053.8	315.0
	292.6	1.7	29.0	7.0	6.0	4.6	13.0
19	180.0	4642911.0	–	417.0	482.0	1616.3	126.0
	472.6	1.5	–	15.0	10.0	5.6	20.0
20	180.0	4650711.0	–	0.0	125.0	1202.7	0.0
	652.6	0.6		0.0	18.0	5.3	0.0

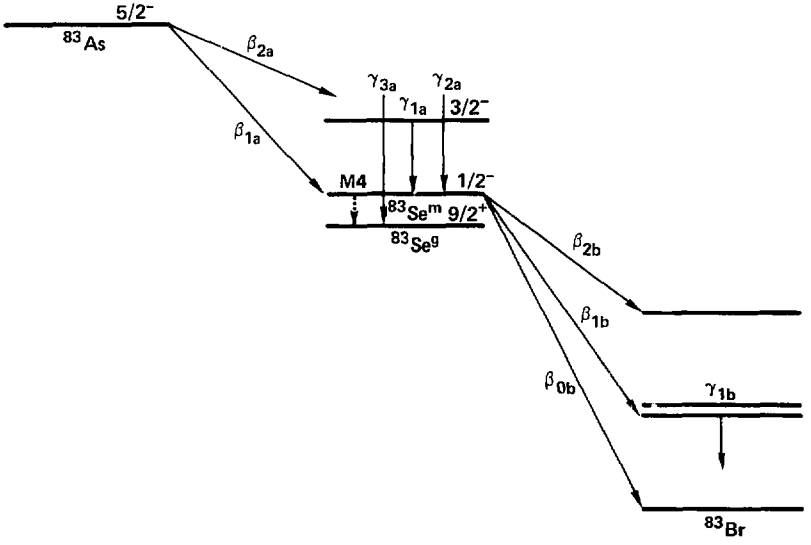

Fig. IV.1. A partial decay scheme showing the gamma transitions, γ_{1a} and γ_{1b}, followed in the growth and decay experiment. The relative beta transition intensity for β_{1a} was determined. Relative gamma transition intensities were known for the decay of $^{83}Se^{m}$ (MEY81) and were measured for the decay of ^{83}As (this work). Relative beta transition intensities for the decay of $^{83}Se^{m}$ were known (SCH68). The labels refer to: β_{2a}, beta transitions from the decay of ^{83}As going to the levels above the $^{83}Se^{m}$ state; γ_{1a}, the 734-keV transition in ^{83}Se; γ_{1b}, gamma transitions fed by the decay of only $^{83}Se^{m}$; and β_{0b}, β_{1b}, β_{2b}, the beta transitions from $^{83}Se^{m}$ which feed the levels in ^{83}Br at 0, 1, and 2 MeV, respectively. The gamma rays are: γ_{1a}, the 734-keV gamma ray which was measured in this experiment; γ_{2a}, collectively, the other gamma rays feeding the $1/2_1^-$ in ^{83}Se; γ_{3a}, the gamma rays feeding the $9/2_1^+$ in ^{83}Se; and γ_{1b}, a typical gamma ray measured in the decay of $^{83}Se^{m}$. The label *M4* refers to the possible *M4* transition which was estimated to have zero intensity.

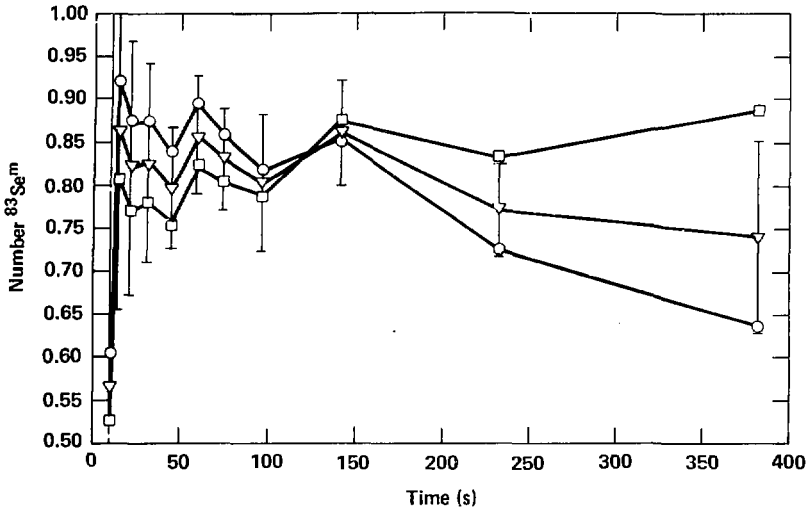

Fig. IV.2a. Number of $^{83}Se^{m}$ nuclei at zero time (N_o) calculated for each time plane in the growth and decay experiment plotted against time for the 674-keV gamma transition. Calculations are based on 65- (□), 70- (▽), and 75-s (○) half-lives. The 70-s half-life gives the most constant N_o. Error bars are indicated for the 70-s half-life.

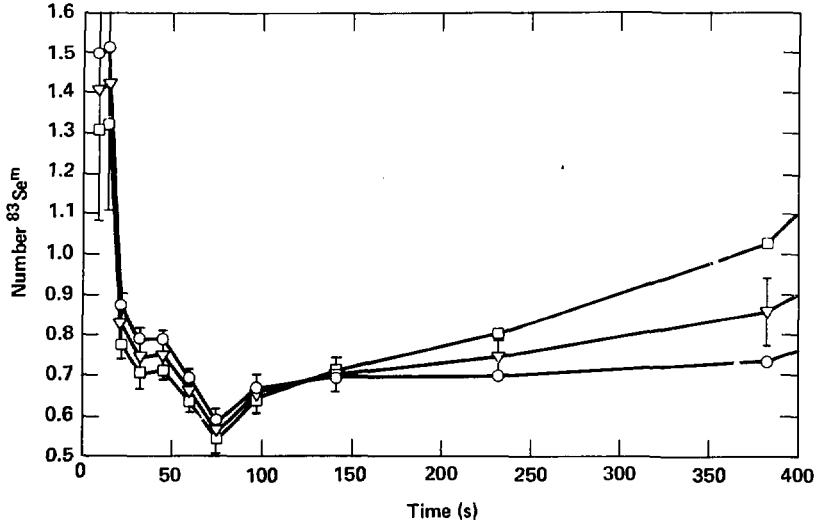

Fig. IV.2b. The plot is the same as Fig. IV.2a, but the values displayed are for the 988-keV gamma ray. Here the effect of the ^{132}Sb contaminant is readily apparent.

The individual spectra then were summed over the ninth through the eighteenth planes (7.6 to 292.6 s) and the last two planes (292.6 to 652.6 s) to give two final spectra and photopeak intensities extracted as before. This procedure eliminated the uncertainty in the dead time in the first eight planes while retaining most of the peak intensity in the first sum (60% of the arsenic and 90% of the selenium data were retained). The second sum was then used to correct for the long-lived contaminants using coefficients calculated from the decay curve.

The photopeak areas were next corrected for the fraction of decays observed over the time interval and relative detector efficiency. The decay fractions were calculated from the Bateman equations (FRI65) and the dead times calculated from the ^{113}Sn data in Table IV.6. The results of these calculations are shown in Table IV.7.

From the data for each gamma ray from the decay of $^{83}Se^{m}$, I obtain the total number of decays of $^{83}Se^{m}$, N_0, which must be equal to the number of decays populating this level

$$N_0 = C(\gamma_{1b})/I(\gamma_{1b}) = C(\gamma_{1a})/I(\gamma_{1a}) \quad , \tag{IV.8}$$

where C is the corrected counts, I is the absolute intensity considering decay to $^{83}Se^{m}$ only, and γ_{1a} and γ_{1b} refer to gamma rays following the decay of ^{83}As and $^{83}Se^{m}$, respectively. The absolute gamma intensity is related to the relative intensities by

$$I(\gamma_{1a}) = \frac{I'(\gamma_{1a})}{I'(\gamma_{1a}) + I'(\gamma_{2a}) + I'(\beta_{1a})} \tag{IV.9}$$

where the I' are relative intensities, γ_{1a} is the 734-keV gamma-ray transition feeding the $1/2^-$ level, γ_{2a} labels all other gamma-ray transitions feeding the $1/2^-$ level as measured in this experiment and β_{1a} is the β^- transition to the $1/2^-$ level. Solving Eqs. (IV.8) and (IV.9) for the β^- intensity yields

Table IV.7. Data development for evaluating the intensity of the β^- branch to the $^{83}Se^{m}$ state. Counts 1 and 2 are from the two summed planes (7.6 to 292.6 s and 292.6 to 652.6 s, respectively) as indicated in the text. N_0(raw) is from decay only, not including the detector efficiency or the absolute gamma intensity.

Energy keV	Counts 1	Counts 2	N_0(raw[a])	detector efficiency[b]	Gamma Intensity	N_0(true)
674	7371	432	8035	2.403	0.137[c]	24406
	(3.1)	(14.3)	(3.1)		(7.2)	(7.8)
734	29820[d]	0	46304	2.232	1.000[e]	20745
	(3.8)	–	(3.8)		(2.6)	(4.6)
988	6297	746	6114[f]	1.741	0.138[c]	25448
	(3.1)	(10.2)	(5.2)		(7.2)	(8.9)
1030	9427	289[g]	7366[g]	1.677	0.194[c]	23255
	(3.3)	(5.2)	(5.2)		(10.2)	(9.2)
2051	2014	130	2195	0.969	0.089[c]	25451
	(5.2)	(20.5)	(5.2)		(7.6)	(8.6)

[a] Counts corrected for decay and contamination effects only.

[b] LIN80.

[c] Absolute intensity: intensities relative to 356-keV transition from MEY81. Absolute normalization of this transition is from SCH68, MEY81, and this work.

[d] Sum for this transition is from 7.6 s to 82.6 s.

[e] This is a relative intensity; total gamma intensity to this level is 1.272.

[f] Corrected for ^{132g}Sb daughter of ^{132}Sn.

[g] Corrected for direct ^{89}Rb.

$$I'(\beta_{1a}) = \frac{C(\gamma_{1b})I'(\gamma_{1a})}{C(\gamma_{1a})I(\gamma_{1b})} - [I'(\gamma_{1a}) + I'(\gamma_{2a})] \quad . \tag{IV.10}$$

The key piece of information needed to obtain the absolute intensities in the decay of $^{83}Se^{m}$ was the intensity of the beta branch to the ^{83}Br ground state, $I(\beta_{0b})$. Using the accepted value for $I(\beta_{0b})$ of 31% (e.g., TOI78) resulted in $^{83}Se^{m}$ having significantly more transitions entering than leaving, an impossible result. Schussler (SCH68) measured relative beta intensities with a magnetic spectrometer and from these relative intensities deduced the absolute intensities. However, he failed to account for the significant contribution of ^{81}Se decay to his beta spectrum. In Appendix 2 this problem is analyzed in detail.

To normalize the beta and gamma-ray intensities I assumed instead that the 2880-keV beta group intensity supplied exactly the beta intensity needed by the levels near 1 MeV as determined from gamma-ray spectroscopy (see App. 2). With this normalization, I determined absolute intensities for the ground state beta branch from $^{83}Se^{m}$ $(38.4 \pm 2.7)\%$, and for the 356-keV gamma-ray transition $(14.9 \pm 0.9)\%$.

Using these values and the data given in Tables IV.6 and IV.7, I found the absolute beta intensity to $^{83}Se^{m}$ to be $(-4 \pm 3)\%$. From this I determined that the beta transition intensity from ^{83}As to the first excited 1/2 state in ^{83}Se is zero. From this zero beta intensity, I conclude that the ^{83}As ground state has a spin and parity of $5/2^-$.

Further confirmation of the 5/2 spin and parity assignment is obtained from the transitions involving the 2077-keV level in ^{83}Se. This level has an allowed log(ft)=5.0 and a strong gamma-ray transition to the $9/2^+$ ground state. The only possible spin and parity assignments are 7/2 for the 2077-keV level and 5/2 for the ^{83}As ground state.

However, the negative intensity for the β^- transition to the $^{83}Se^{m}$ isomeric state is physically impossible and does not allow the calculation of a log(ft) value. Using Bayes' principle it is possible to obtain the most probable β^- intensity for the observed data. Assuming that the intensity must be greater than zero, a probability distribution function with that property is generated and an expected value calculated from the inputs. Equation (IV.10) was rearranged to give

$$I'(\beta_{1a}) = \frac{\alpha C_b - \beta C_a}{C_a} \quad , \tag{IV.11}$$

where C is the number of counts corrected for contamination but nothing else, a and b label counts from the decay of ^{83}As and ^{83}Se, respectively, and α and β are constants which include decay effects, intensities, and detector efficiencies. Using the algorithm developed by Vincent (VIN82) and Eq. (IV.11), I calculated that the β^- intensity to $^{83}Se^{m}$ was $(0.3 \pm 0.2)\%$ absolute and log(ft)=7.9. This log(ft) value agrees with similar decays from ^{81}Se, ^{69}As, and ^{65}Ni, which have log(ft) values ranging from 7.4 to greater than 9.8 (TOI78).

The last intensity needed is the β^- branch to $^{83}Se^{g}$. This was estimated from the log(f_1t) for β^- decay of ^{71}Zn and ^{85}Kr to 5/2 states. All of these β^- decays transform a 1g9/2 neutron to a 1f5/2 proton so I expect the β^- decay to have a log(f_1t) similar to those in ^{71}Zn and ^{85}Kr, which have values of 9.5 and 9.4 respectively. Using this value in the ^{83}As decay gives a β^- intensity of 0.7%, which does not alter my prior intensity calculations.

This result for ^{83}As β^- decay is markedly different from other odd-mass arsenic β^- decays to the first $1/2^-$ state in selenium. In Table IV.5, I give the beta transition intensity for beta decay from the arsenic ground state to the first $1/2^-$ state in selenium. For $^{77,79,81}As$, the ground state is 3/2 and the transition has high intensity, but for ^{83}As I have found this intensity to be 0.3%. In Fig. IV.3, I give the systematics for the odd-mass arsenics (HOF81). In odd-mass $^{75-81}As$, the first $5/2^-$ is near 300 keV. It could readily become the ground state. The $5/2^-$ spin and parity assignment is consistent with the lack of beta intensity to the first $3/2^-$ state in ^{83}Se. While this appears to be a Gamow-Teller allowed transition, it is not. In a simple shell model picture, the only beta transition to a 3/2 state of seniority one transforms a P3/2 neutron into an F5/2 proton, which is

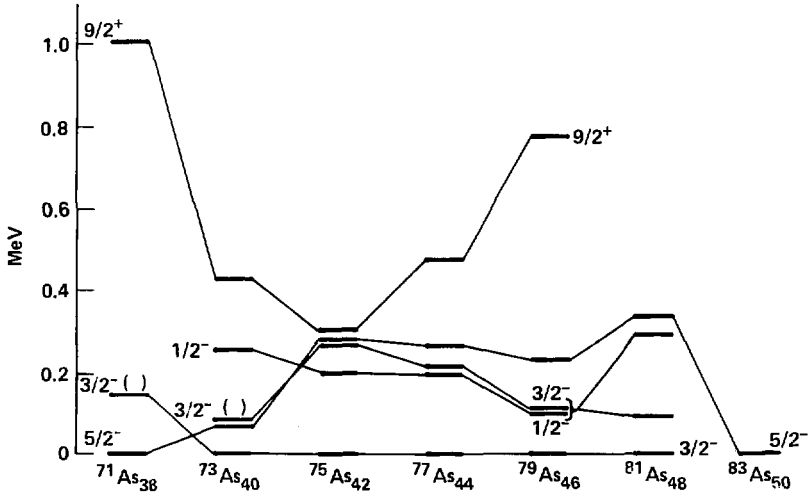

Fig. IV.3. Systematics of the nuclear levels of the odd-mass arsenics. The $5/2^-$ level is the first excited state, but is low enough in energy that it could become the ground state in ^{83}As as it is in the light mass arsenics (HOF81).

an angular-momentum forbidden process. I obtain a log(ft)=6.6, which is consistent with other log(ft) values for F5/2 to P3/2 β^- transitions (KON66).

I find no evidence for levels previously found at 0.36 and 0.43 MeV (LIN65), in agreement with Montestruque et al. (MON78). Neither did I find any evidence for the level at 0.822 MeV (MON78) or 0.85 MeV (LIN65). I give the arguments for assigning spin and parity to levels of ^{83}Se in Table IV.8. This completes the development of the ^{83}As decay scheme which is presented in Fig. IV.4.

Table IV.8. Spin and parity assignments. In this table the reasoning for the spin and parity assignments is presented. Where there is no discrepancy I took the spin and parity assignment from the $^{82}Se(\vec{d},p)^{83}Se$ experiment of Montestruque et al. (MON78). The remainder of the assignments were made on the gamma-ray transitions and on the $\log(f_0t)$ values observed in this work. All observed gamma-ray transitions were assumed to be *E1*, *M1*, or *E2* transitions. The states with allowed beta transitions ($\log(f_0t) \leq 5.9$) were restricted to possible spin and parity of 3/2 , 5/2 , and 7/2 . Spins are given as 2J.

Energy (keV)	Spin, Parity	Justification
0	9⁺	MON78.
229	1	MON78.
540	1⁺	MON78.
582	5⁺	MON78.
963	3	Transitions to levels of spin and parity 1/2⁺ and 1/2 and transitions from levels of spin and parity 7/2 . This assignment is consistent with levels in Zr_{39} (NDS75) and Sr_{49} (NDS79) where 3/2 levels have been identified near 1 MeV in transfer reaction studies.
1063	(5)	Transitions to 1/2 and from 7/2 permit either 3/2 or 5/2 . The 5/2 assignment is consistent with levels in Zr_{49} and Sr_{49} as in previous level.
1101	3⁺	MON78.
1265	(7⁺)	Transitions to the 3/2⁺, 5/2⁺, and 9/2⁺ levels permit 5/2⁺ or 7/2⁺. The lack of a transition to the 1/2⁺ level suggests the assignment given.
1297	(11⁺)	This assignment is limited only by transition to the 9/2⁺ level. However, the transitions from the levels at 1296, 1331, 1527, and 1822 keV make it appear that they are four of the five members of the one phonon 9/2⁺ multiplet. Assuming this assignment, these are the only reasonable spin and parities for these levels.
1331	5⁺	MON78.
1473	(3⁺)	3/2 spin from gamma-ray transitions. Positive parity preferred from intensity of transitions to positive parity states.
1526	(9⁺)	See the discussion for the level at 1297-keV.
1665	5⁺	MON78.
1710	(3⁺)	Transitions to 1/2 and 5/2⁺ levels permit 1/2⁺, 3/2, or 5/2 assignment. Transition intensity to positive parity states favors the positive parity assignment. The 3/2 assignment is consistent with a transition to the (7/2)₁⁺ level.
1822	(7)⁺	See the discussion for the level at 1297-keV. Transitions limit the spin and parity to 5/2⁺ or 7/2.
1908	3,5⁺	Transitions to 1/2⁺, 5/2⁺, and 5/2 permit any of these assignments.
1943	5⁺,7	Transitions to 3/2 and 9/2⁺ levels allow only these.
2077	7	Transition to 9/2⁺ level and an allowed $\log(ft) = 5.0$ give 7/2 .
2138	3⁽⁺⁾	Transitions to 1/2⁺, 1/2 , 5/2⁺, and 5/2 levels allowed only these assignments Presence in Ref. MON78 suggests positive parity.
2190	5⁺,7	Transitions to 5/2⁺ and 9/2⁺ levels and a transition from a 3,5/2 level allowed only these assignments. Presence in Ref. MON78 reaction favors positive parity.
2482	5⁺	MON78.
2546	3⁺	MON78.
2679	3	Transitions to levels of 1/2⁺, 1/2 , 5/2⁺, and 5/2 allowed a 3/2 assignment. Allowed $\log(ft) \sim 5.9$ requires negative parity.
2725	5⁺	Transitions to 9/2⁺, 3/2⁺, and 3/2 allowed only the 5/2⁺ assignment.
2858	7	Transition to 9/2⁺ level and the allowed $\log(ft) = 4.7$ permitted only the 7/2 assignment.
2881	(5)	Transitions to 3/2⁺, 3/2 , 5/2⁺, 5/2 , and 7/2 permitted 3/2 or 5/2 assignment. The allowed $\log(ft) = 4.7$ gives the negative parity assignment. The transition to the (7/2⁺) level at 1822 keV gives the (5/2) spin.
2971		Limited only by transitions to 1/2⁺ and 5/2⁺ levels.
2981	7	Transition to 9/2⁺ level and an allowed $\log(ft) = 5.1$ give the assignment.

Table IV.8. (Continued.)

Energy (keV)	Spin, Parity	Justification
3167	3	Transitions to 1/2 , 1/2', 5/2 , and $5/2^+$ gave a spin of 3/2. The allowed log(ft)=4.7 gives the negative parity.
3243	7	Transition to $9/2^+$ level and the allowed log(ft)=4.7 give this assignment.
3282	3	Transitions to $1/2^+$, $5/2^+$, and $5/2^-$ permitted 3/2 or $5/2^+$ assignment. The allowed log(ft)=5.6 gives the negative parity.
3334	3 ,5	Transitions to $3/2^-$, $3/2^+$, $5/2^-$, $5/2^+$, and $7/2^-$ permit $3/2^-$ or 5/2. The allowed log(ft)=5.6 gives the negative parity.
3386		Restricted only by transition to $3/2^-$ level.
3424		Restricted only by transitions to $3/2^-$, $5/2^+$, and $5/2^-$.
3464	5'	*MON78.*
3558		Transition to $5/2^+$ is the only restriction.
3690		Restricted only by transitions to $3/2^-$ and $5/2^-$ levels and allowed log(ft)=5.7.
3828		Restricted only by a transitions to $3/2^-$ and $5/2^+$ levels.
3911		Restricted only by a transition to $5/2^+$ level.
4001		Restricted only by a transition to $3/2^-$ level.

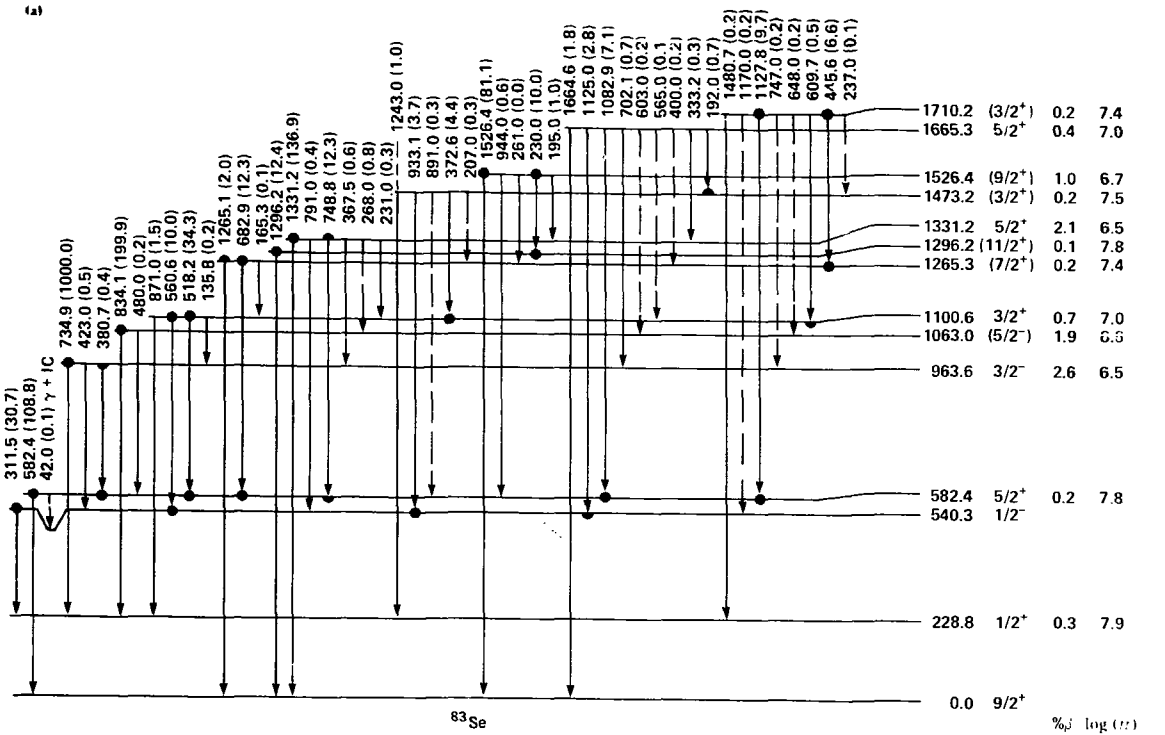

Fig. IV.4 Decay scheme for ^{83}As.

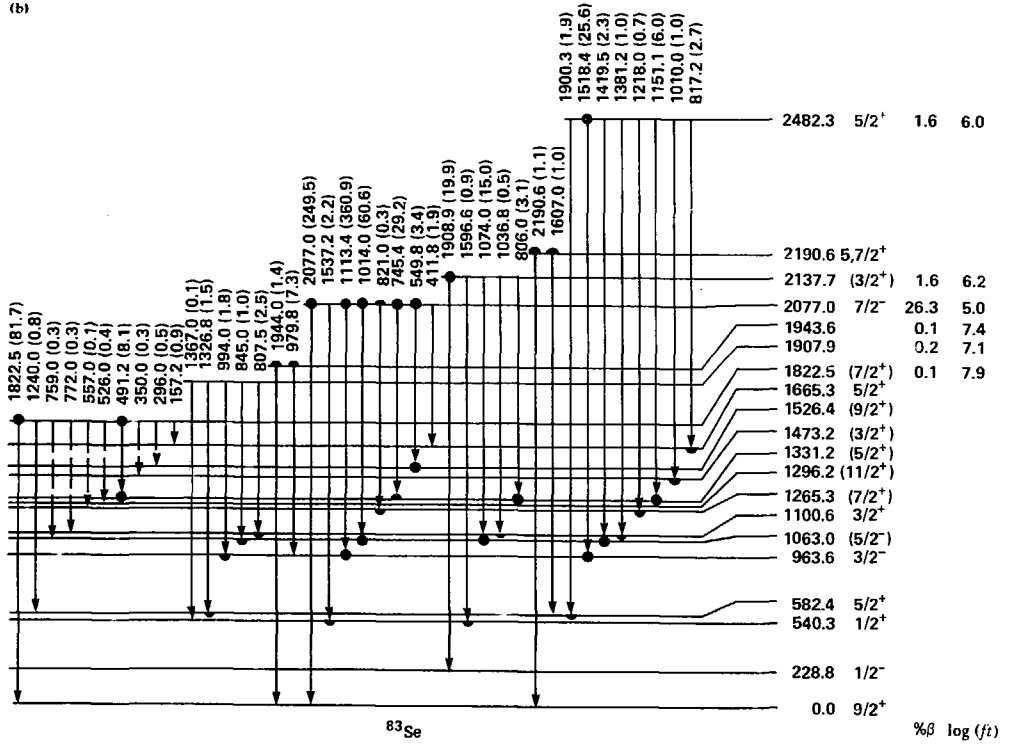

Fig. IV.4 (Continued.)

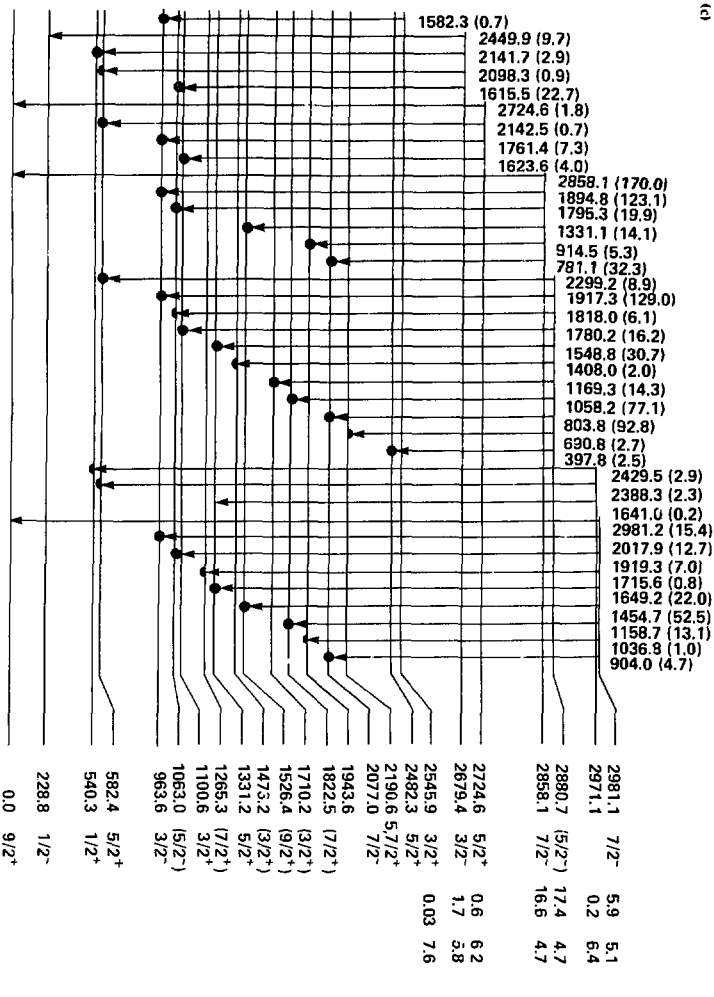

Fig. IV.4 (Continued.)

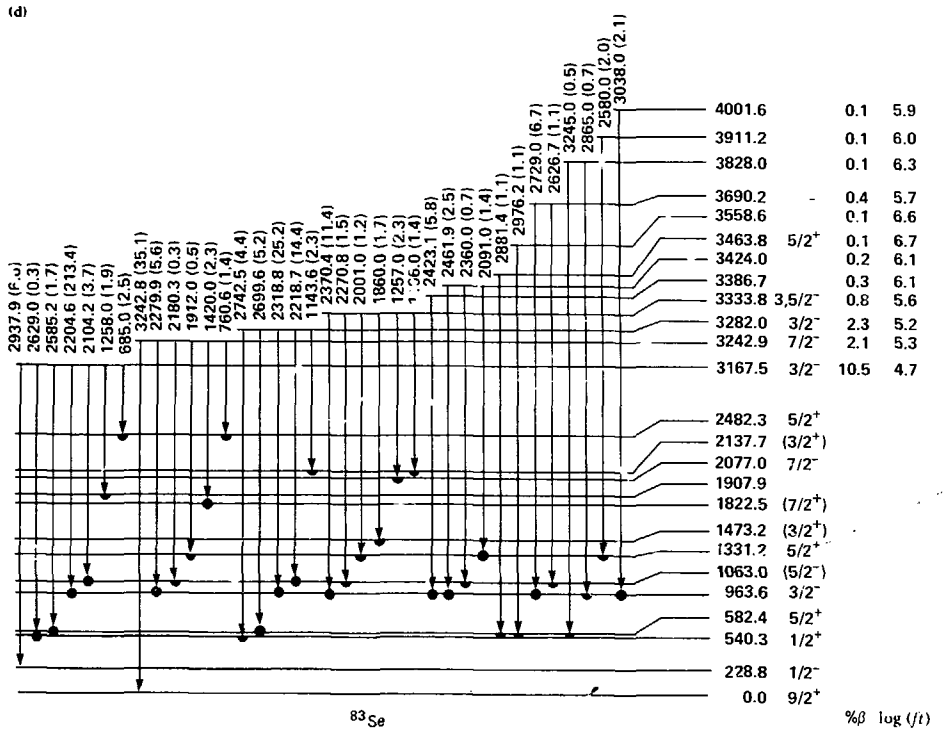

Fig. IV.4 (Continued.)

V. Systematics of N=49 and Z=49 Nuclei

In odd-mass nuclei lacking one proton (neutron) from shell closure and near mid neutron-(proton-) shell there should be a set of levels based on a hole in the natural single proton (neutron) (1h) states and another set of levels, also at low energy, based on a particle in the intruder single proton (neutron) states and 2 holes in the natural single proton (neutron) states. These intruder states are found in the $_{49}$In (i.e. 1g7/2, 2d5/2, 2d3/2, and 3s1/2) and $_{81}$Tl (i.e. 1h9/2, 1i13/2, and 2f7/2) nuclei (WOO80, ZGA80). Charge independence suggests that similar structure should occur in the N=49 and N=81 isotones, but this structure has not been observed. In particular, this structure has not been observed in $^{89}Zr_{49}$ or $^{87}Sr_{49}$. However, I have observed this structure in ^{83}Se. Unified model calculations by Heyde have been used to completely describe the structure of the odd mass indium nuclei (HEY78, GLA79, HEY80 and earlier work described therein). I will use these unified model calculations performed by K. Heyde (HEY82a) to describe the structure of $^{83}Se_{49}$ and to describe the intruder level systematics for the N=49 isotones.

In nuclei which lack a proton (neutron) from shell closure and are near mid neutron-(proton-) shell the following five significant properties are observed and serve to define the natural and intruder states:

- There is a group of states at low energy from across the shell closure, called intruder states.
- There exist vibrational bands built on both the natural and intruder states.
- The core for the intruder states is different from the core for the natural states.
- Gamma-ray transitions between the natural and intruder states of the same parity are highly hindered.
- The $E1$ transitions are all highly hindered.

I will discuss each of these properties first for the indium (Z=49) case which has been well developed and then for the ^{83}Se (N=49) case to show the similarity.

The natural states for a single hole in either 50 nucleon shell are the 1g9/2, 2p1/2, 2p3/2, and 1f5/2 states. At low energy in the indium nuclei, levels have been identified through the ^{A}Cd(^{3}He,d)$^{A-1}$In (A even) reactions which have large spectroscopic factors for the 1g7/2, 2d5/2, 2d3/2 and 3s1/2 single particle states (MAR74, THU70, HAR72), states which occur above the 50 particle shell closure. These levels would normally be expected to occur above 2 MeV in excitation energy due to the single particle energy gap at the major shell closure. The systematics of these levels are shown in Fig. V.1. The intruder levels show a distinct minimum at ^{117}In which is mid neutron-shell.

Other low-lying levels can be described by coupling the single particle or hole to vibrational modes of the core. The core for the intruder states is different from the core for the natural states. In a schematic sense the natural states are a "core + hole", while the intruder states are a "core + particle"; however the cores obviously do not have the same number of nucleons. The core for the natural states has 50 nucleons, while the core for the intruder states has 48 nucleons. The differences in the vibrational modes of these two cores can be seen by comparing the excitation energies of the first 2$^+$ states in the even-even core nucleus. In Fig. V.2 these energies are shown for the even-even tin and cadmium isotopes (Z=50 and 48, respectively). The excitation energy of the first 2$^+$ state in the 48 particle core is approximately half that in the 50 particle core.

There exist vibrational bands built on both the natural and intruder states. These bands feature enhanced $M1$ and $E2$ intra-band transitions and highly hindered inter-band transitions. In the indium isotopes these enhancement factors have been measured (HEY78, GLA79, HEY80) and show strongly enhanced B($E2$) values in the intruder band and enhanced B($M1$) from states in the vicinity of the particle-one-phonon-vibrational multiplet built on the 9/2$^+$ hole. In ^{83}Se, the measurements are not available for reduced transition probabilities, but the band structure is still apparent.

From the isospin independence of nuclear forces, states similar to those in Z=49 nuclei should occur in the N=49 nuclei. Studies of ^{87}Sr and ^{89}Zr failed to find any of the particle intruder levels state below 2 MeV, except for the 2d5/2 . However, the ^{82}Se(d,p)^{83}Se reaction study by

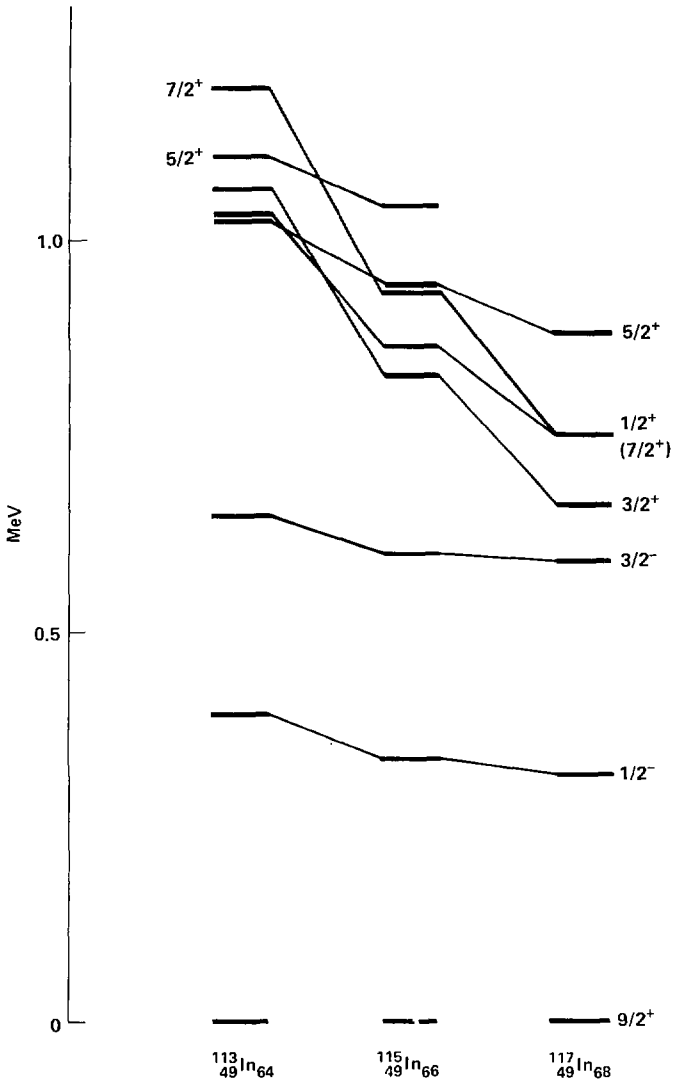

Fig. V.1. Systematics of the low lying levels in $^{113-119}$In with emphasis placed on the low lying $7/2^+$, $5/2^+$, $3/2^+$, and $1/2^+$ intruder levels.

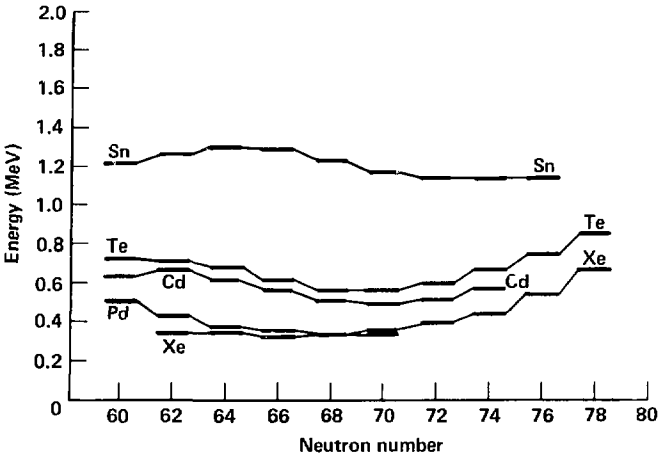

Fig. V.2. Systematics of the energy of the first 2^+ level in the indium region.

Montestruque, et al. (MON78) identified the intruder states 2d5/2, 3s1/2, and 2d3/2 in ^{83}Se at low energy. Figure V.3 shows a partial level diagram for the low energy intruder states relative to the natural states for selected N=49 isotones.

The similarity of the intruder levels in the N=49 isotones is pointed up by the consistency of the spectroscopic factor, $(2J+1)S_{lj}$, for the (d,p) reaction. These relatively constant values (Table V.1) for the $5/2^-$, $1/2^+$, and $3/2^+$ levels for ^{83}Se, ^{85}Kr and ^{87}Sr show that while the levels move up in excitation energy, the single particle component is relatively constant.

However, in the neutron case, the intruder band structure is well developed only in ^{83}Se and ^{81}Ge, where the energy of the first 2^+ state in the N=48 is below 0.7 MeV (Fig. V.4). This is the energy of the first 2^+ in the cadmium isotopes. I will discuss this topic further when comparing the theoretical and experimental results.

The unified model describes most of the Z=49 (indium) isotopes very well, particularly ^{113,115,117,119}In (HEY78, GLA79, HEY80 and earlier work described therein). Attempts to use a similar description in the N=49 nuclei ^{89}Zr and ^{87}Sr have not met with success. I will compare the properties of these two groups of nuclei to show that this form of the vibrational model does describe the N=49 nucleus, ^{83}Se.

Table V.1. Systematics of the spectroscopic factor for the (d,p) reaction to produce ^{83}Se, ^{85}Kr and ^{87}Sr. The values given are for $(2J+1)S$ with the level energy in MeV in parentheses.

Spin Parity	Nucleus		
	^{83}Se	^{85}Kr	^{87}Sr
$5/2^-$	2.76 (0.58)	3.43 (1.14)	2.94 (1.78)
$3/2^+$	0.60 (1.10)	0.36 (2.06)	0.35 (2.7)
$1/2^+$	0.56 (0.54)	0.76 (1.43)	0.56 (2.18)

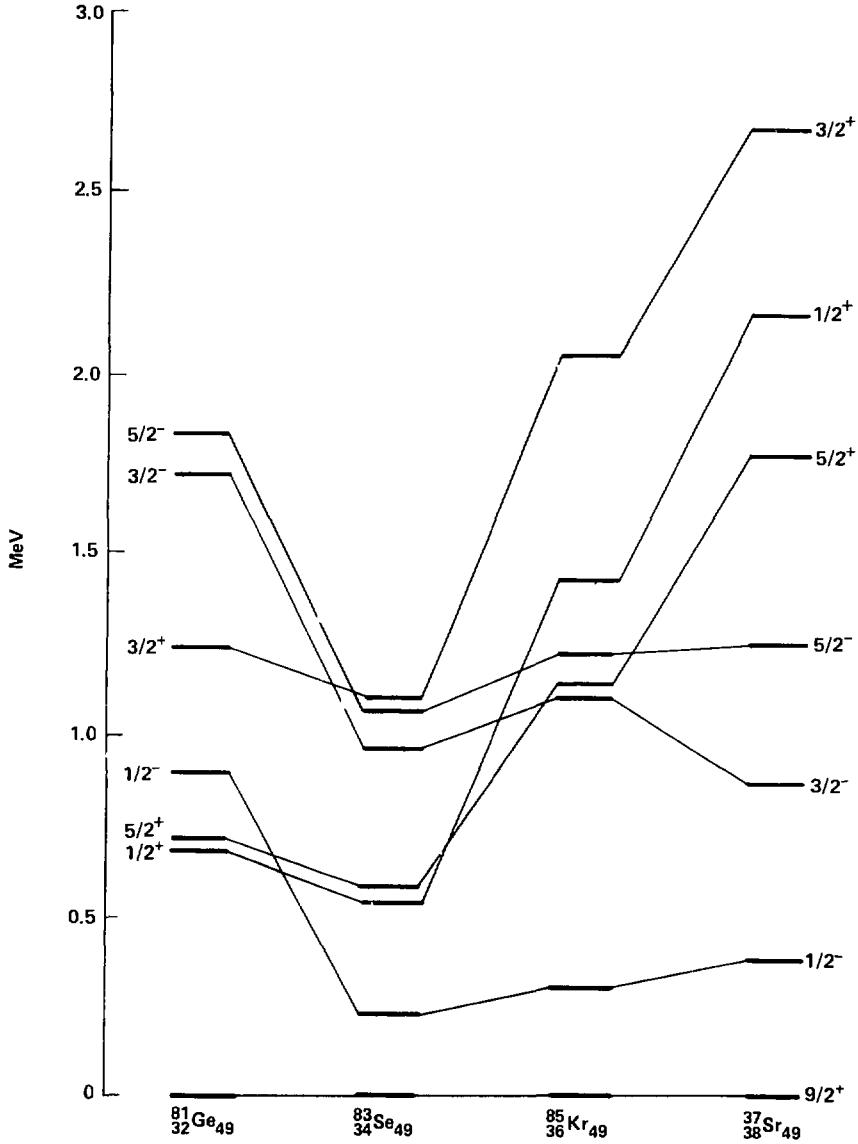

Fig. V.3. Systematics of the low lying levels in the N=49 isotones, with emphasis placed on the low-lying $5/2^+$, $1/2^+$, and $3/2^+$ intruder levels.

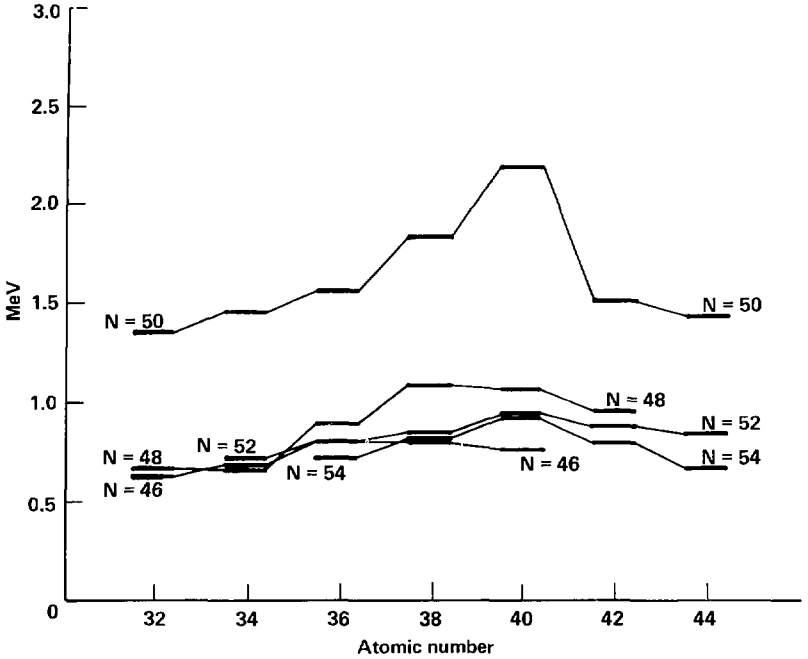

Fig. V.4. Systematics of the energy of the first 2^+ level in the N=50 region.

VI. Theory

The unified model is a phenomenological model for describing collective core excitations and the coupling of these core excitations to the valence particle(s). In the N=49 and Z=49 nuclei these core excitations are vibrations. I will give a qualitative description of the vibrations of the even-even core, followed by the odd-even case in the weak coupling limit. The unified model then introduces the more realistic intermediate coupling. I will discuss the unified model as developed by Heyde and others to explain the structure observed in indium nuclei, and use this model to explain the structures of ^{83}Se and other N=49 isotones.

Vibrational Model

The vibrations will appear directly as part of the low energy (<2.5 MeV) nuclear structure only if the energy required to excite them is less than approximately 2.5 MeV. Thus, monopole and dipole vibrations are not observed at low energy. The monopole vibration occurs at high excitation energy because the nuclear density is fixed. The dipole vibration can appear only as the giant dipole resonance which occurs at excitation energies above 15 MeV. I will restrict the discussion to quadrupole vibrations. Higher order vibrations (particularly the 3^-, octupole vibration)

have been observed. They are treated similarly to the quadrupole vibrations and can couple to other vibrations and the single particles and holes. They will not be discussed further as the octupole vibration lies near 3 MeV in N=48 and N=50 nuclei (MAT77), while the quadrupole vibration occurs at 0.7 and 1.5 MeV, respectively, in these nuclei.

Vibrational structure appears as collective motion in even-even nuclei. In the weak coupling limit there is no interaction between the different vibrational levels. The Hamiltonian is (BOH75)

$$H_{coll} = \sum b^{\dagger} b \quad , \tag{VI.1}$$

where $b^{\dagger}$ is the creation operator for vibrational quanta (phonons). The levels obtained for quadrupole vibration are shown in column 2 of Fig. VI.1. Each level can be identified by (n,R) where n is the number of phonons which are coupled to angular momentum R. The levels are at an excitation energy given by $E_n = n\hbar\omega$, where $\hbar\omega$ is the phonon energy. The levels are degenerate in R.

When an odd particle (hole) of spin and parity j is added to the even-even vibrational core the Hamiltonian becomes (BOH75)

$$H = H_{coll} + H_{sp} \tag{VI.2}$$

where H_{sp} describes the single particle motion. The levels are obtained at the same excitation energies as in the even-even case but the states are now described as $[(n,R)j]\,J$ where the single particle of spin and parity j coupled to the core angular momentum, R, to give total angular momentum and parity J, with J restricted by

$$R + j \geq J \geq |R - j| \quad . \tag{VI.3}$$

These levels are also at excitation energy $E_n = n\hbar\omega$ and are degenerate in both R and J. The spins for a $1/2^+$ and a $9/2^+$ particle are shown in columns 4 and 5 of Fig. VI.1, respectively.

The degeneracy can be removed by adding to the Hamiltonian a residual interaction term which treats the particle-phonon interaction,

$$H_{int} = -k \sum_{\mu} b_{2\mu} Y_{2\mu}(x) \tag{VI.4}$$

3	0,2,3,4,6	————	1;3,5;5,7;7, 9;11,13	9;5,7,9,11,13;3,5,7,9,11,13, 15;1,3,5,7,9,11,13,15,17;1,3, 5,7,9,11,13,15,17,19,21
2	0,2,4	————	1,3,5,7,9	9;5,7,9,11,13;1,3,5,7,9,11,13, 15,17
1	2	————	3,5	5,7,9,11,13
0	0	————	1	9
n	R	level	j=1/2	j=9/2

Fig. VI.1. Energy levels for quadrupole vibration. Spins are given for quadrupole vibration, column 2, and for quadrupole vibration coupled to a spin 1/2 particle, column 4, and for quadrupole vibration coupled to a spin 9/2 particle, column 5. For the odd particle the spins are given as 2J.

where Y is the spherical harmonics and x is the particle coordinates. The effect of varying the coupling constant, k, in the case of one phonon and a $5/2^+$ particle has been discussed by Choudhury (CHO54).

The observables of interest are the level energies, the reduced transition probabilities, and the spectroscopic factor for particle stripping reactions. The electromagnetic transitions can go only by $E2$ (for quadrupole vibration) or $M1$ radiation. For $E2$ transitions the selection rule is

$$|n_i - n_f| = 1 \tag{VI.5}$$

The reduced transition probabilities for transitions between multiple phonon states for quadrupole vibrations are given by (BOH75,p. 360)

$$B(E2;|(n,R)j| J' \rightarrow |(n',R')j| J'| = (2J'+1)(2R+1) \times \begin{Bmatrix} R & j & J \\ J' & 2 & R' \end{Bmatrix}^2 B(E2;(n,R) \rightarrow (n',R')) \tag{VI.6}$$

where the only transitions have multipolarity $E2$. For $M1$ transitions the matrix element is (BOH75,p. 360)

$$\langle |(n,R)j| J' \, M(M1) \, |(n,R)j| J \rangle = \sqrt{\frac{3}{4\pi}} \frac{e\hbar}{2Mc} g_j [J(J+1)(2J+1)]^{1/2} \delta_{JJ'}$$

$$+ (-1)^{R+j+J+1} ((g_\lambda - g_j) R(R+1)(2R+1))^{1/2} \begin{Bmatrix} R & j & J \\ J' & 1 & R \end{Bmatrix} . \tag{VI.7}$$

The spectroscopic factor for transfer reactions can be obtained. If the state is expanded as

$$\sum_{n'R'j'} c(n'R'j'J) \, |(n',R')j'| J \rangle \quad , \tag{VI.8}$$

then the spectroscopic factor is given by

$$S_{fi} = c^2(|(0,0)j| J) \tag{VI.9}$$

for the transfer of a particle of spin and parity j into the even-even core with spin and parity 0^+.

Unified Model

The coexistence of the natural and intruder levels requires a model that treats both types of levels on an equal footing. The unified model has been extended to do this by K. Heyde (HEY78, HEY80). For completeness I describe this model in the following section.

The Hamiltonian must be separable as

$$H = H_{coll} + H_{sp} + H_{int} \tag{VI.10}$$

where the three parts of the Hamiltonian describe the collective, single particle and residual interaction. The actual Hamiltonian is given by

$$H = E_0 + \sum_\lambda b_\lambda^\dagger b_\lambda \left| \hbar\omega_\lambda + (2\lambda+1)/2 \right| + \sum_\alpha \epsilon_\alpha N(c_\alpha^\dagger c_\alpha)$$

$$+ \sum_{\alpha\beta\lambda\mu} \langle\alpha|Y_{\lambda\mu}|\beta\rangle \hbar\omega_\lambda E_\lambda \left[b^\dagger_{\lambda\mu} + (-1)^\mu b_{\lambda-\mu}\right] N\left(c^\dagger_\alpha c_\beta\right)$$

$$+ \frac{1}{4} \sum_{\alpha\beta\gamma\delta} V_{\alpha\beta\gamma\delta} N\left(c^\dagger_\alpha c^\dagger_\beta c_\gamma c_\delta\right) \qquad \text{(VI.11)}$$

where E_0 is the energy of the 0^+ ground state in the N=50 nucleus.
$b^\dagger_{\lambda\mu}$ is the phonon creation operator, with the restriction $\lambda=2$
$\hbar\omega_\lambda$ is the phonon energy in the N=50 nucleus
ϵ_α is the single particle energy
E_λ is the dimensionless coupling coefficient, defined by

$$E_2\hbar\omega_2 = \left\langle r\frac{\partial V}{\partial r}\right\rangle \frac{4(5\pi)^{1/2}}{3ZeR_0^2} B\left(E2;2_1^+ \rightarrow 0_1^+\right)^{1/2} \qquad \text{(VI.12)}$$

$N(c_\alpha...)$ is the number operator
$V_{\alpha\beta\gamma\delta}$ is the residual interaction between the neutron particles or holes.

By restricting the single particle degrees of freedom to the 2d5/2, 3s1/2, 2d3/2, 1g7/2, and 1h11/2, and the single hole degrees of freedom to the 1g9/2, 2p1/2, 2p3/2, and 1f5/2 orbitals the Hamiltonian can be restructured as

$$H = H_c + H_{sp} + H_{sh} + H_{ps} + H_{hc} + H_{phc} + V_{hh} + V_{ph} \qquad \text{(VI.13)}$$

where H_c ; describes the low-lying excitations of the N=50 core,
H_{sp}, H_{sh} ; describe the single-particle and -hole motion,
H_{ps}, H_{hc}, H_{phc} ; describe the particle-, hole- and particle-hole-core interaction,
V_{hh}, V_{ph} ; describe the residual hole-hole and particle-hole interaction,

$H_c = E_0 + \sum_\lambda b^\dagger_\lambda b_\lambda \left[\hbar\omega_\lambda + (2\lambda+1)/2\right]$;

$H_{sp} = \sum_\alpha \epsilon_\alpha N\left(c^\dagger_\alpha c_\alpha\right)$; α is a particle,

$H_{sh} = \sum_\alpha \epsilon_\alpha N\left(c^\dagger_\alpha c_\alpha\right)$; α is a hole,

$H_{ps} = \sum_{\alpha\beta\lambda\mu} \langle\alpha\, Y_{\lambda\mu}|\beta\rangle \hbar\omega_\lambda E_\lambda \times \left[b^\dagger_{\lambda\mu} + (-1)^\mu b_{\lambda-\mu}\right] N\left(c^\dagger_\alpha c_\beta\right)$; α, β are particles,

H_{hc} = " ; α, β are holes

H_{phc} = " ; α is a particle and β is a hole or the reverse,

$V_{hh} = \frac{1}{4} \sum_{\alpha\beta\gamma\delta} V_{\alpha\beta\gamma\delta} N\left(c^\dagger_\alpha c^\dagger_\beta c_\gamma c_\delta\right)$; α, β, γ, δ are holes,

V_{ph} = " ; α, β, γ, δ are particles or holes; α, β different and γ, δ different.

The allowed configurations are one hole and one particle plus two holes.

The first step in solving the Hamiltonian, Eq. (VI.13), is to describe the low-lying excitations in the N – 48 isotones

$$H_{sh}(N-48) = \omega(N-48) \qquad \text{(VI.14)}$$

which is explicitly

$$(H_{\rm c} + H_{\rm ch} + H_{\rm hc} + V_{\rm hh})\,|{\rm N}=48;I^{(i)}M\rangle = \omega(I,i)|{\rm N}=48;I^{(i)}M\rangle \qquad \text{(VI.15)}$$

where the N=48 eigenstates are expanded to

$$\left|{\rm N}=48;I^{(i)}M\right\rangle = \Omega^{\dagger}_{I,i}({\rm N}=48)|\tilde{0}\rangle = \sum_{h_1 h_2 JR} d^{(i)}\left[(h_1,h_2)J,R;I\right] \times \left[(\tilde{c}_{h1},\tilde{c}_{h2})_J \otimes \Omega^{\dagger}_R({\rm N}=50)\right]_{IM}|\tilde{0}\rangle \qquad \text{(VI.16)}$$

where:

$I^{(i)}$	is the ith state with spin and parity I,
$\Omega^{\dagger}$	is the phonon creation operator in the appropriate nucleus,
$d^{(i)}[..]$	is the expansion coefficient for the state having holes in single particle states h_1 and h_2 coupled to J total angular momentum; the single particle state is then coupled to the N=50 phonon state. n phonons coupled to to angular momentum R, which are finally coupled to total angular momentum state I with z component M,
c_h	is the annihilation operator, which creates holes,
R	abbreviates $(n_\lambda,R_\lambda)R$.

Solution of Eq. (VI.16) yields the phonon states for N=48.

Having obtained the phonon levels for N=48 and N=50 nuclei, the states of the N=49 nucleus are created. For the hole states in the N=50 core

$$\left|j_h^{-1},{\rm N}=50(R);IM\right\rangle = \left[\tilde{c}_h \otimes \Omega^{\dagger}_R({\rm N}=50)\right]_{IM}|\tilde{0}\rangle \qquad \text{(VI.17)}$$

and for the particle states in the N=48 core

$$\left|j_p,{\rm N}=48(I_i)IM\right\rangle = \left[c^{\dagger}_p \otimes \Omega^{\dagger}_i(48)\right]_{IM}|\tilde{0}\rangle \qquad \text{(VI.18)}$$

The resulting wave functions are then (in the most general form)

$$I^{(n)}M\rangle = \sum_{hR} h^{(n)}(hR;I)\left|j_h^{-1},{\rm N}=50(R);IM\right\rangle + \sum_{pi} p^{(n)}(pi;I)\left|j_p,{\rm N}=48(I,i);IM\right\rangle \qquad \text{(VI.19)}$$

The secular equations for the N=49 nuclei were then expressed in matrix form as

$$\begin{pmatrix} H+\epsilon_h+\sum_\lambda \hbar\omega_\lambda N_\lambda & L(s,I';I) \\ L(s',I;I) & K+\omega(I,i) \end{pmatrix} \begin{pmatrix} h^{(n')} \\ p^{(n')} \end{pmatrix} = E(I^{(n)}) \begin{pmatrix} h^{(n)} \\ p^{(n)} \end{pmatrix} \qquad \text{(VI.20)}$$

where

$$\begin{aligned}
H &= H(hR,h'R';I) \\
&= \left\langle j_h^{-1},{\rm N}=50(R);I\middle|V_{\rm hc}\middle|j_{h'}^{-1},{\rm N}=50(R');I\right\rangle \\
L(s,I';I) &= \lambda(hR,p'I'i';I) \\
&= \left\langle j_h^{-1},{\rm N}=50(R);I\middle|V_{\rm ph}+H_{\rm phc}\middle|j_{p'},{\rm N}=48(I'i');I\right\rangle \\
L(s',I;I) &= \lambda(h'R',pIi;I) \\
K &= K(pIi,p'I'i';I) \\
&= \left\langle j_{p'},{\rm N}=48(Ii);I\middle|V_{\rm ph}+H_{\rm pc}\middle|j_{p'},{\rm N}=48(I'i');I\right\rangle \\
h^{(n')} &= h^{(n)}(h'R';I) \\
h^{(n)} &= h^{(n)}(hR;I)
\end{aligned}$$

$$p^n(') = p^n(p'l'i';J)$$
$$p^n(\ ) = p^n(pli;J)$$

Detailed expansions for these matrix elements are given in Appendix A of reference HEY78.

Parameters

I now give the parameters used to describe ^{83}Se (HEY82). The collective parameters are

$\hbar\omega_2(N=50) = 1.4$ MeV

$\hbar\omega_2(N=48) = 0.655$ MeV

from experimental measurement for the quadrupole phonon energies. No octupole phonons were used as these have been identified at 2.5 MeV (MAT77) for nuclei with N<51 and Z>30 and will have little effect on the low energy structure. Values for the dimensionless coupling coefficients are

$\Gamma_2(N=50) = 1.0$

$\Gamma_2(N=48) = 6.0,$

which are taken from Eq. (VI.12) using experimental values for $\hbar\omega_2$ and B(E2) with slight empirical adjustment. The single particle and hole energies in MeV are

$\epsilon_{1h11/2}$	2.6		
$\epsilon_{1g7/2}$	2.8	$\tilde{\epsilon}_{1f5/2}$	1.35
$\epsilon_{2d3/2}$	2.6	$\tilde{\epsilon}_{2p3/2}$	1.15
$\epsilon_{3s1/2}$	1.5	$\tilde{\epsilon}_{2p1/2}$	0.40
$\epsilon_{2d5/2}$	0	$\tilde{\epsilon}_{1g9/2}$	0

which were modified from Ref. REE70. The energy required to create a particle hole pair, E_{ph}, is 2.15 MeV. The residual interaction, $V_{\alpha\beta\gamma\delta}$, was a delta function force without spin exchange of the form $V = V_0\delta(\mathbf{r}_1 - \mathbf{r}_2)$ with V_0 adjusted to fit the levels of ^{82}Se (HEY80).

I compare the results of the model calculations to three sets of experimental data: the energy levels, the gamma-ray transition data from the decay of ^{83}As and the ^{82}Se(d,p)^{83}Se stripping reaction. The operator for the electric moments is

$$M(EL,\mu) = (B(EL,\uparrow 0)_{N=50})^{1/2}\left[b^\dagger_{\lambda\mu} + (-1)^\mu b_{\lambda\mu}\right] \times \sum_{\alpha\beta} \langle\alpha|r^\lambda Y_{\lambda\mu}|\beta\rangle c^\dagger_\alpha c_\beta \qquad \text{(VI.22)}$$

and for the magnetic dipole moment is

$$M(M1,\mu) = g_R R_\mu + \sum_{\alpha\beta} \langle\alpha|g_l \ell_\mu + g_s s_\mu|\beta\rangle c^\dagger_\alpha c_\beta \quad , \qquad \text{(VI.23)}$$

where g_l and g_s are the orbital and spin gyromagnetic factors, respectively. The detailed matrix elements that result from these operators are given in Appendix B of Ref. HEY78. The transitions can be reduced to three pertinent transition types:

1. Single particle transitions within either the N=48 or N=50 subsystem.
2. Collective transitions in either the N=48 or N=50 subsystem.
3. Single particle transitions between the N=48 and N=50 subsystems.

With these operators level lifetimes, $M1$-$E2$ mixing ratios and branching ratios for the levels can be calculated.

The spectroscopic factors for neutron stripping into levels above the N=50 shell closure is

$$S^{\alpha}_{\eta}(J) = p^{\alpha}(\ell_j, 0^+_i; J)^2 \delta_{jj} \quad . \tag{VI.24}$$

These operators allow calculation of the experimentally observed values in ^{83}Se. The other operators applicable to this model are described in Ref. HEY78. They include operators for the neutron pickup reaction, and the static magnetic dipole and electric quadrupole moments.

VII. Discussion

I will compare first the theoretical and experimental results for $^{83}_{34}Se_{49}$; the level properties, spin and parity, excitation energy, and spectroscopic factor. The theory is the unified model discussed in the previous section and the experimental measurements are my gamma-ray measurements and the ^{82}Se(d,p)^{83}Se experiment by Montestruque et al. (MON78). Next, I will compare the observed and predicted gamma-ray transitions in ^{83}Se. Last, I will discuss the effect of Z=40 shell closure, which blocks the collectivity needed to develop the intruder structure levels at low energy in nuclei near Z=40.

I expect three types of levels in ^{83}Se: the natural, negative parity levels arising from the 2p1/2, 2p3/2, and 1f5/2 single neutron hole states; the natural, positive parity levels arising from the 1g9/2 single neutron hole states; and the intruder, positive parity levels arising from the 2d5/2, 2d3/2, 3s1/2, and 1g7/2 single particle states. The model 1h11/2 component does not mix with any of the natural components, nor does it occur in any levels below 3.6 MeV. The parameters used in modeling ^{83}Se were given in the previous section. In Appendix 3, I give the theoretical composition of the levels to 3.5 MeV and up to spin $13/2^+$ and $7/2^-$. In Fig. VII.1, I show a ladder diagram comparing theoretical and observed energies. A fourth type of level has been added; those positive parity levels where neither natural or intruder dominates substantially.

Natural Levels

The first $1/2^-$, $3/2^-$, and $5/2^-$ levels show a good comparison in energy between theory and experiment. The theoretical group of levels between 1.7 and 2.0 MeV is not clearly identified experimentally and may be the levels of uncertain parity indicated in Fig. VII.1. The gamma-ray transition branching ratios will be discussed later.

The $(11/2^+)$, $5/2^+$, $(9/2^+)$ and $(7/2^+)$ levels at 1296, 1331, 1527, and 1822 keV could be members of the $[(1,2)9/2^+]$ multiplet. Theoretically the multiplet is rather unmixed with the multiplet component being at least 0.8 in all levels. Level energies show good agreement between theory and experiment as shown in Fig. VII.1. For an unmixed multiplet, the energy centroid, given by

$$\sum_I E_I/5,$$

should be the energy of the first 2^+ state in the core nucleus, ^{84}Se, which is at 1454 keV. For the four levels observed, the centroid is at 1494 keV, experimentally, and 1476 keV, theoretically. For the complete multiplet the centroid is at 1454 keV, theoretically.

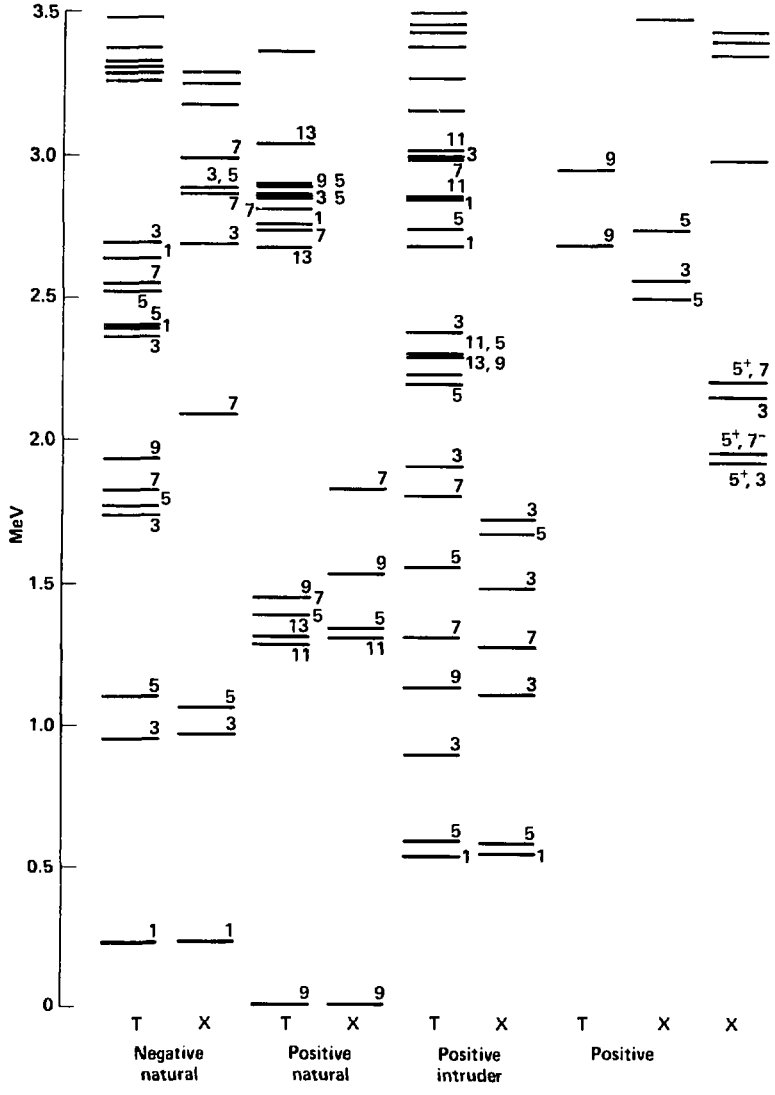

Fig. VII.1. Comparison of experimental and theoretical level energies for ^{83}Se. Each column is labeled theory (T) or experiment (X). The first four pairs of columns are the natural negative parity levels, the natural positive parity levels, the positive parity intruder levels (I), and the positive parity mixed levels. The last column has the experimental levels of unknown parity. The spins of the levels are given as 2J. All the negative parity levels are in the first two columns, the remainder are positive or unknown parity.

Intruder Levels

Experimentally, the intruder levels do not have any multiplet grouping in energy. Theoretically, all of the intruder levels are of mixed composition, usually including some small natural component. By mixed composition I mean that the level has no component with a squared expansion coefficient which was greater than 0.4, with most being less than 0.3. This mixing suggests that the multiplet structure would be substantially shifted as observed in experiment. Many of the calculated levels, especially above 2 MeV, were not found in the experiment, although this may be due to the levels not being populated in β-decay.

The unified model gives much better prediction on number and energy of $1/2^+$ states than does the weak coupling model. The weak coupling limit predicts the following eleven $1/2^+$ states below an excitation energy of 3 MeV: [(0,0)1/2$^+$], [(2,0)1/2$^+$], [(3,0)1/2$^+$], [(1,2)3/2$^+$], [(2,2)3/2$^+$], [(3,2)3/2$^+$], [(1,2)5/2$^+$], [(2,2)5/2$^+$], [(3,2)5/2$^+$], [(3,3)5/2$^+$], [(2,4)9/2$^+$] where the level energy is determined in the weak coupling way as

$$E_x = n\hbar\omega + E \text{ (single particle)} \qquad \text{(VII.1)}$$

and n is the number of phonons of energy $\hbar\omega$ and E is the excitation energy of the lowest state of spin j. The states based on the 7/2$^+$ single particle were ignored since no spectroscopic factor was found for the 1g7/2 in the (d,p) experiment. The unified model predicts only 4 $1/2^+$ levels below 3 MeV, three of which lie between 2.5 and 3 MeV. Experimentally, there are three $1/2^+$ levels identified below 4 MeV, with four more levels which could be $1/2^+$, but with $3/2^+$ preferred and one possible assignment of $1/2^+$. Figure VII.2 shows the $1/2^+$ levels found by the weak coupling model, experiment and the unified model. The unified model predicts the gap from 0.6 to 2.3 MeV, with no $1/2^+$ levels, while the weak coupling limit does not.

Spectroscopic Factor for $\vec{(d,p)}$ Reaction

The single particle transfer reaction serves as a good test of the model states. For ^{83}Se only the ^{82}Se(d,p)^{83}Se reaction has been studied. This reaction observes the spectroscopic factor for the intruder single particle only. In Fig. VII.3 the theoretical and experimental spectroscopic factors are compared. The theoretical spectroscopic factors are generally a factor of 2 lower than experiment. This difference is consistent with that found in the indium nuclei (HEY78, HEY80, GLA77). A further test of the model is a comparison of the theoretical and experimental values for the summed spectroscopic factor,

$$S_{\ell_j} = \sum_i S_{\ell_j i} \quad ; \qquad \text{(VII.2)}$$

the mean energy E_j,

$$E_j = \frac{\sum_i E_{ji} S_{\ell_j i}}{S_{\ell_j}} \quad ; \qquad \text{(VII.3)}$$

and the width of the spectroscopic factor distribution,

$$W_j^2 = \frac{\sum (E_{ji} - E_j)^2 S_{\ell_j i}}{S_{\ell_j}} \quad . \qquad \text{(VII.4)}$$

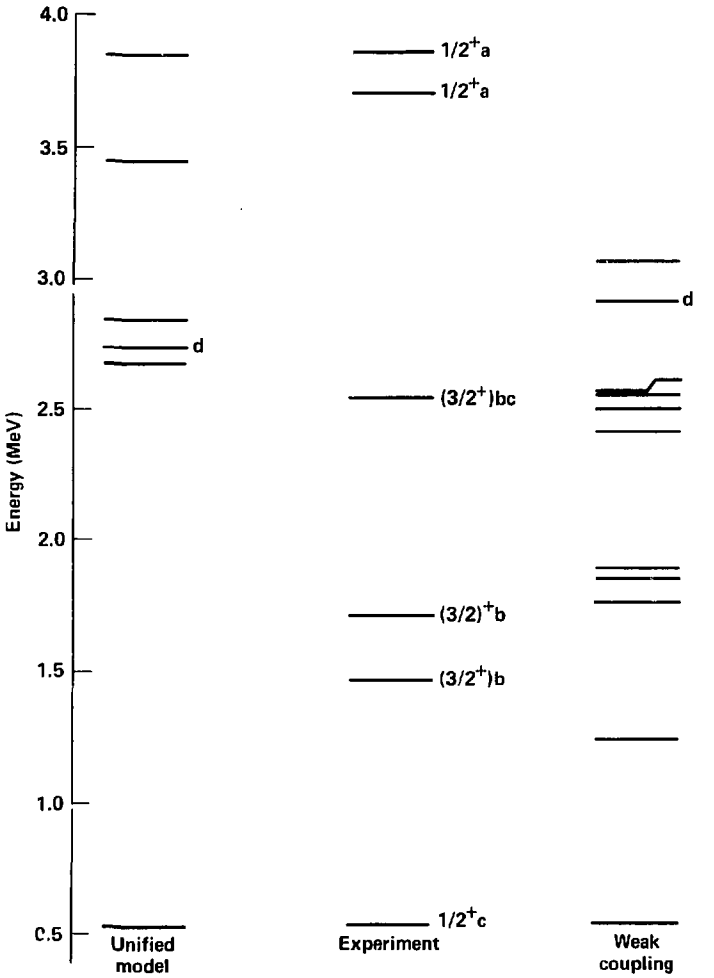

Fig. VII.2. Comparison of the $1/2^+$ states found by the unified model, experiment, and the weak coupling limit. Notes: a) LIN65, b) this work, c) MON78, d) natural level.

In Table VII.1, I present these values for $j=3/2^+$ and $j=5/2^+$. Much better agreement is obtained for the averaged values than for the individual levels.

There are two interesting discrepancies between theory and experiment. The $5/2^+$ 2.18 MeV theoretical level has a spectroscopic factor of 2.77 which is much higher than any of the experimental levels. This would seem to indicate that the $5/2^+$ spectroscopic factor does not spread

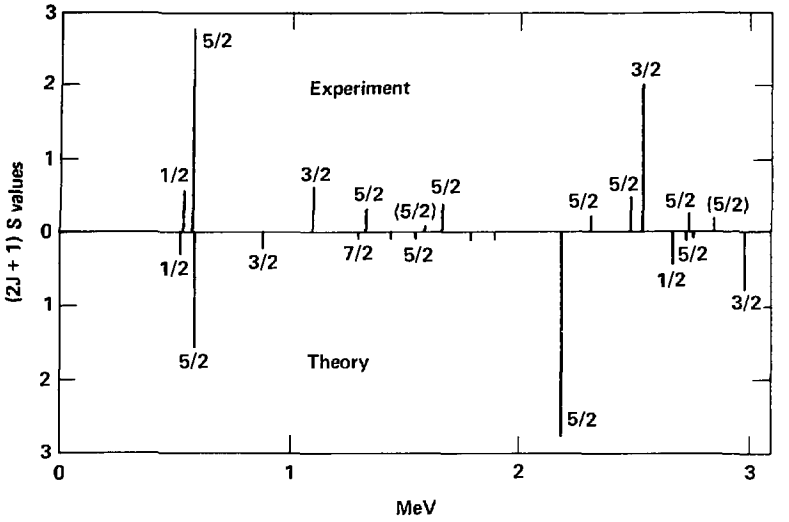

Fig. VII.3. Comparison of spectroscopic factor for theory and experiment in the $^{82}Se(d,p)^{83}Se$ reaction. All states shown are positive parity.

Table VII.1. Comparison of spectroscopic factor distribution for theory and experiment for the $^{82}Se(d,p)^{83}Se$ reaction. Experimental values are from determined from Ref. MON78.

	Levels of Spin and Parity			
	3/2⁺		5/2⁺	
	Theory	Experiment	Theory	Experiment
S_{lj}	1.45	2.58	4.28	5.32
E_l	2.84	2.20	1.66	1.50
W_l	0.92	0.60	0.77	1.08
cutoff	3.7	3.7	–	–

enough in the calculation. On the other hand, there is no theoretical level with the spectroscopic factor held by the experimental 3/2⁺ 2454-keV level, which suggests the opposite difficulty for the 3/2⁺ levels.

Gamma-Ray Branching Ratios

Natural Levels

I discuss the gamma-ray branching ratios for the low lying levels and the 7/2 levels as determined by my experiment. First, I will discuss the 9/2⁺ level and its associated multiplet; next the natural 7/2 levels; and last the intruder levels.

Figure VII.1 shows the good agreement obtained between theory and experiment for the energy of the four observed members of the [(1,2)9/2$^+$] multiplet found experimentally. I compare the theoretical and experimental gamma-ray branching ratios from these levels in Fig. VII.4. The gamma-ray branch to the ground state dominates for each of these levels. The $\Delta\ell$=1 intramultiplet transitions all show good agreement between theory and experiment. The 13/2$^+$ member of this multiplet is not observed, as a two gamma-ray cascade is required to populate such a high spin state from a 7/2$^-$ state populated via β^- decay.

Most of the large discrepancies occur where the experimental branching ratios are very small and uncertain, hence the discrepancies are not significant. The theoretical branching ratio for the 557-keV transition from the 7/2$^+$ 1822-keV level to the 7/2$^+$ 1265-keV level is 60 times too large. This discrepancy will be discussed when I discuss the 7/2$^+$ with the intruder levels.

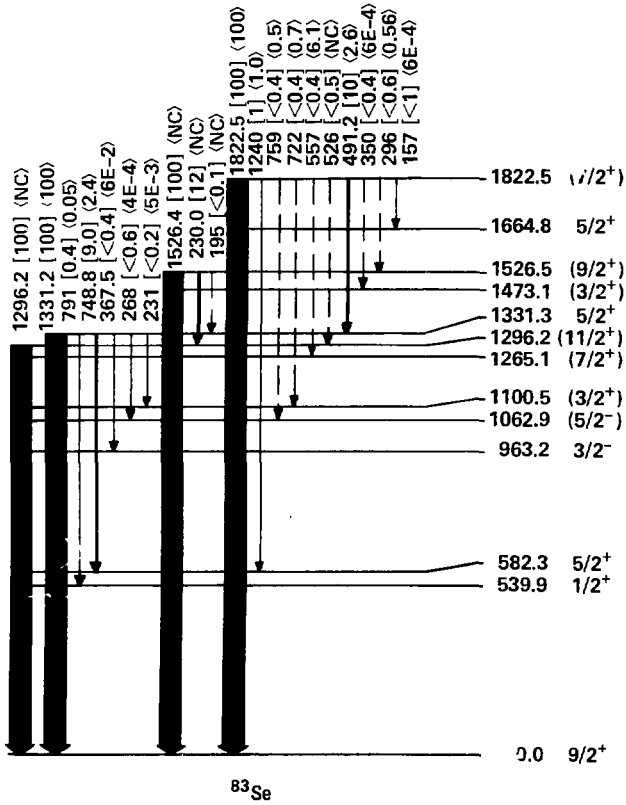

Fig. VII.4. Gamma transition branching ratios for theory and experiment for the [(1,2)9/2$^+$] multiplet in ^{83}Se. Branching ratios are normalized to 100 for the most intense experimental transition. The branching ratios are given in square brackets [experimental] and in angle brackets ⟨theory⟩, (NC) means that the theoretical transition was not calculated.

From the gamma-ray branching ratios, the $5/2^+$ 1331-keV level is a member of the $[(1,2)9/2^+]$ multiplet. Theoretically the branch to the $5/2^+$ 582-keV intruder level is a factor of 4 weaker than experiment. The theoretical $(2J+1)S$ value is 0.00, while the experimental value is 0.33. The major intruder component of this level is 4% $[(1,2)5/2^+]$. If this were $[(0,0)5/2^+]$, it would give a $(2J+1)S$ value of 0.24, but it is the wrong component.

The $7/2^-$ States

These levels are interesting because they can have no seniority one component, except for a vanishingly small 1f7/2 hole component, and have not been previously identified in N=49 nuclei. In Fig. VII.5, I show these levels and their branching ratios for $M1/E2$ transitions. (All these levels have intense $E1$ transitions to the ground state, but the theory makes poor predictions for $E1$ transitions.)

The configuration of these $7/2^-$ states can be a) $[(2,4)1/2^-]$, b) $[(1,2)3/2^-]$ or c) $[(1,2)5/2^-]$ for levels at 2077, 2858, and 2981 keV. The $3/2^-$ 963- and $5/2^-$ 1063-keV levels can have configurations $[(0,0)3/2^-]3/2^-$ and $[(1,2)1/2^-]3/2^-$; and $[(0,0)5/2^-]5/2^-$ and $[(1,2)1/2^-]5/2^-$ respectively. The relative $B(E2)$ for transitions between these configurations are:

1) for $7/2^- \rightarrow 3/2^-$
   - $[(1,2)3/2^-]7/2^- \rightarrow [(0,0)3/2^-]3/2^-$ 1.0
   - $[(2,4)1/2^-]7/2^- \rightarrow [(1,2)1/2^-]3/2^-$ 1.7
2) for $7/2^- \rightarrow 5/2^-$
   - $[(1,2)5/2^-]7/2^- \rightarrow [(0,0)5/2^-]5/2^-$ 1.0
   - $[(2,4)1/2^-]7/2^- \rightarrow [(1,2)1/2^-]5/2^-$ 0.2

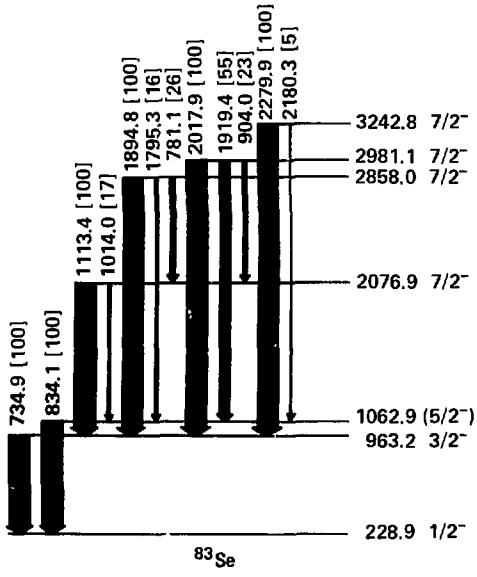

Fig. VII.5. Gamma transition branching ratios for theory and experiment for the $7/2^-$ levels. Other information is the same as for Fig. VII.4.

I assume that the 7/2⁻ to 5/2⁻ transition is predominately an *E*2 transition. The *M*1 is a single particle transition, while the *E*2 is a collective transition. This suggests that the $7/2^-$ levels are predominately of configurations a and b, for if configuration c is a major component of the $7/2^-$ levels, the transition to the 5/2⁻ state should be enhanced. Based on the transition branching ratios, only the 2981-keV level could be of configuration c. Any *M*1 contribution to the transition to the 5/2⁻ state only emphasizes the $1/2^-$ multiplet component, as this component allows no *M*1 transition.

The calculated coefficients for the components of the $7/2^-$ levels are given in Table VII.2. They show reasonable agreement with the above evaluation, with the $1/2^-$ and $3/2^-$ based components dominating.

The Intruder Levels

The intruder levels are all positive parity and can be expected to mix with each other. The major components are 2d5/2, 3s1/2, and 2d3/2, with the 1g7/2 being small. Further the natural 1g9/2 configurations will mix with the intruder configurations to varying degrees.

Our measured value for the half-life of the $5/2^+$ 582-keV level, 3.1 ns, shows that the transition to the 9/2⁺ ground state is hindered by a factor of 8.1 relative to the single particle estimate (NDS81). The unified model calculations show a hindrance factor of 1.6. Both of these hindrance values are significantly different from the core *E*2 transitions which have enhancement values of 7 for the ^{84}Se core, and 17 for the ^{82}Se core. This is consistent with the cores for the intruder and natural states being substantially different which precludes the transition being a simple single particle transition.

The transition from the $5/2_3^+$ level to the $1/2_1^+$ level, which might be expected from similar highly enhanced transitions in the indium nuclei, has as a branching ratio less than 0.3. Including the value for the internal conversion coefficient, 19 (ROS78), this limit corresponds to a maximum 10-fold enhancement of the transition. This enhancement is comparable to those observed in the indium nuclei. The model calculations obtained a branching ratio of 4E-3, an enhancement of 12, which is consistent with the experimental results.

The $1/2_2^+$, $5/2_2^+$, $3/2_1^+$, $7/2_1^+$, and $5/2_3^+$ are the low-lying intruder levels. The energy of these levels does not display the particle plus vibrational core multiplet structure, such as was observed with the 1g9/2 hole plus N=50 vibrational core, nor do the gamma-ray transitions fit that description. Figure VII.6 shows the experimental energy levels and compares experimental and theoretical gamma-ray branching ratios. These levels have been identified as having intruder components in the (d,p) reaction (MON78), except for the 7/2⁺, and the gamma-ray branching ratios confirm this identity. The multiplet structure is destroyed by the strength of the particle-vibration coupling and the presence of several single particle orbitals at low energy. The analogous situation occurs in the indium nuclei.

Experimentally the largest branch is always to the $5/2^+$ 582-keV level, with a smaller branch to the $1/2^+$ 547 keV level, where allowed. Branches to the natural states are always smaller as expected. Branches between the $3/2^+$, $7/2^+$ and $5/2^+$ 1665-keV levels are also very small.

Table VII.2. Selected expansion coefficients for the first three 7/2⁻ states and the $3/2_1^-$ and $5/2_1$ states. These can be used for estimating the gamma-ray branching ratios from the 7/2⁻ states to the $5/2_1$ and the $3/2_1$ states.

	Expansion coefficient for					
J^π	[(2,4)1/2]	[(1,2)1/2]	[(1,2)3/2]	[(1,2)5/2]	[(0,0)3/2]	[(0,0)5/2]
$7/2_1$	0.579	–	0.672	0.158	–	–
$7/2_2$	0.074	–	0.233	0.768	–	–
$7/2_3$	0.597	–	0.305	0.119	–	–
$3/2_1$	–	0.558	0.278	0.162	0.688	–
$5/2_1$	–	0.618	0.152	0.264	–	0.619

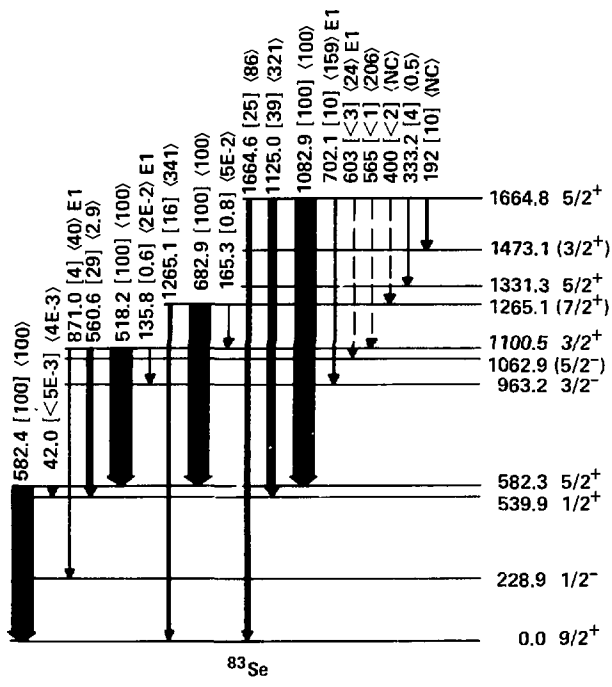

Fig. VII.6. Gamma transition branching ratios for theory and experiment for the intruder-one-phonon levels. Other information is the same as for Fig. VII.4.

Theoretically, the major branches from the 3/2$^+$ and 5/2$^+$ 1665-keV level are to the intruder levels. The specific branching to the intruder levels is not well reproduced. Without experimental $M1/E2$ mixing ratios and experimental reduced transition probabilities, it is not possible to explain these differences.

The two (3/2)$^+$ levels at 1472 and 1710 keV (Fig. VII.7) feed the lower intruder levels strongly. Their theoretical energies were off by 300 keV. The spectroscopic factors were very low both in theory and experiment. The experimental branching ratios from the 1710-keV level are well reproduced by the theory. The experimental branching ratios from the 1472-keV level appear poorly reproduced.

The unified model correctly predicts the main features of the low-lying level structure in ^{83}Se. The intruder band structure is confirmed. The deficiencies in the intruder band branching ratios are probably cancellation effects (HEY82b). The misplaced gamma-ray transition intensity from the intruder levels and the missing spectroscopic factor from the 5/2$^+$ natural level may be caused by incorrect mixing of the intruder and natural levels. Also possible are the missing contributions from 2-particle 3-hole configurations. Lin (LIN65) has measured a substantial component of $n(d5/2)^2_{0^+}$ in the ^{82}Se ground state, which suggests the 2-particle 3-hole configuration may be present in the low-lying levels of ^{83}Se. These configurations are not treated in the unified model.

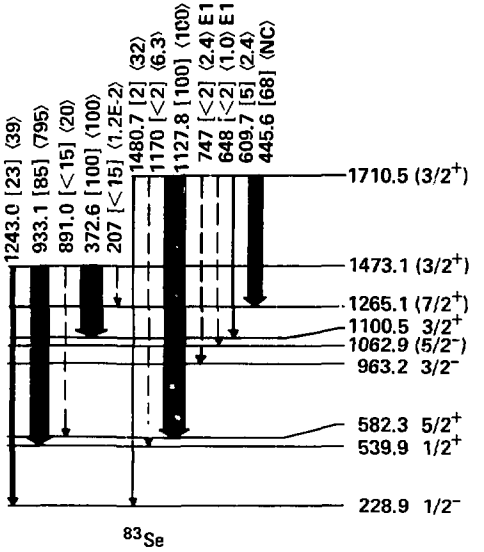

Fig. VII.7. Gamma transition branching ratios for theory and experiment for the $3/2^+$ intruder-two-phonon multiplet. Other information is the same as for Fig. VII.4.

Theoretical Systematics

In the earlier section on systematics of the N=49 isotones and Z=49 (indium) isotopes, I pointed out that while the natural levels remain at nearly constant energy in both systems, the energy of the intruder levels varies substantially. In the indium nuclei the intruder level energies are slowly changing (Fig. V.1) but in the N=49 isotones the level energies are rapidly increasing in energy from Z=32 germanium to Z=40 zirconium (Fig. V.3). I noted that this behavior is similar to the behavior of the energy of the 2^+ level in the respective core nuclei. I will now look at the unified model parameters used to reproduce the systematic behavior in these two groups of nuclei.

In Tables VII.3 and VII.4, I present the unified model parameters used to reproduce the 49 nucleon systematics, Z=49 and N=49 respectively. The parameter $\hbar\omega_2$ is taken from the energy of the 2^+ excited state of the appropriate nucleus as previously discussed. The dimensionless coupling coefficient is constant for indium nuclei, and for the N=50 core in the N=49 case. However, for the N=48 core it varies dramatically, from 6 for selenium to 3.5 for strontium. The energy required to create the particle hole pair also changes much more rapidly in the 49 isotones than in the indium nuclei. The single particle energies do not change at all in indium, and only slightly in the N=49 isotones.

The changes in the collective parameters of the unified model reproduce the systematic behavior of the intruder levels in the N=49 nuclei (Fig. VII.8). Further, the differences in behavior among the lowest $1/2^+$, $3/2^+$, and $5/2^+$ intruder states are also correctly reproduced, without recourse to the single particle energies. I note that the $3/2^+$ level energy changes most, but the corresponding single particle energy not at all.

The collective nature of the Z or N = 48 nucleus appears to be the dominant factor in the appearance of the intruder states. In the indium case, far from shell closure, the intruder levels are at low energy and vary slowly with neutron number. The minimum is at mid neutron shell ^{117}In. In the N=49 case, the intruder levels are at low energy in ^{81}Ge and ^{83}Se, at mid proton shell. These are much closer to shell closure than in the indium case (3 nucleon pairs vs. 7 nucleon pairs) and the intruder levels rise rapidly to the proton shell closure at Z=40.

Table VII.3. The parameters used for the N=49 nuclei to reproduce the systematic behavior of the intruder and natural levels. The parameters are the quadrupole phonon energy, $\hbar\omega_2$, the dimensionless coupling coefficient, E_2, the energy required to create a particle hole pair, ΔE_{ph}, and the single particle energies, ϵ. All parameters are in MeV, except for E_2.

	$^{81}_{32}Ge_{49}$	$^{83}_{34}Se_{49}$	$^{85}_{36}Kr_{49}$	$^{87}_{38}Sr_{49}$
$\hbar\omega_2(N=50)$[a]	1.400	1.400	1.565	1.836
$\hbar\omega_2(N=48)$[a]	0.655	0.655	0.882	1.077
$E_2(N=50)$	2.0	2.0[b]	2.0	2.0
$E_2(N=48)$	5.75	6.00	4.50	3.50
$\epsilon_{g9/2}$	0[c]	0	0	0
$\epsilon_{p1/2}$	1.30	0.70	0.80	1.00
$\epsilon_{p3/2}$	2.30	0.70	1.70	1.50
$\epsilon_{f5/2}$	2.55	1.65	1.90	2.00
ΔE_{ph}	2.0	2.0	2.50	2.80
$\epsilon_{d5/2}$	0	0	0	0
$\epsilon_{3s1/2}$	1.40	1.50	1.60	1.80
$\epsilon_{2d3/2}$	2.60	2.60	2.60	2.60
$\epsilon_{g7/2}$	2.80	2.80	2.80	2.80
$\epsilon_{1h11/2}$	2.60	2.60	2.60	2.60

[a] Experimental value.

[b] A value of 1.0 was used in the calculations for ^{83}Se.

[c] Zero values without decimal point are zero by definition.

Table VII.4. The parameters used for the Z=49 nuclei to reproduce the systematic behavior of the intruder and natural levels. The parameters are the quadrupole phonon energy, $\hbar\omega_2$, the dimensionless coupling coefficient, E_2, the energy required to create a particle hole pair, ΔE_{ph}, and the single particle energies, ϵ. All parameters are in MeV, except for E_2.

	$^{115}_{49}In_{66}$	$^{117}_{49}In_{68}$	$^{119}_{49}In_{70}$	$^{121}_{49}In_{72}$
$\hbar\omega_2(Z=50)$[a]	1.293	1.3	1.17	1.14
$\hbar\omega_2(Z=48)$[a]	0.538	0.54	0.487	0.506
$E_2(Z=50)$	2.4	2.4	2.4	2.4
$E_2(Z=48)$	8.1	7.6	7.6	7.6
$\epsilon_{g9/2}$	0[b]	0	0	0
$\epsilon_{p1/2}$	0.60	0.60	0.60	0.60
$\epsilon_{p3/2}$	1.30	1.30	1.20	1.20
$\epsilon_{f5/2}$	2.00	2.00	1.90	1.90
ΔE_{ph}	2.4	2.34	2.5	2.5
$\epsilon_{g7/2}$	0	0	0	0
$\epsilon_{d5/2}$	0.50	0.50	1.0	1.0
$\epsilon_{1h11/2}$	2.10	2.10	2.10	2.10
$\epsilon_{2d3/2}$	2.60	2.60	2.60	2.60
$\epsilon_{3s1/2}$	2.95	2.95	2.95	2.95

[a] Experimental.

[b] Zero values without decimal point are zero by definition.

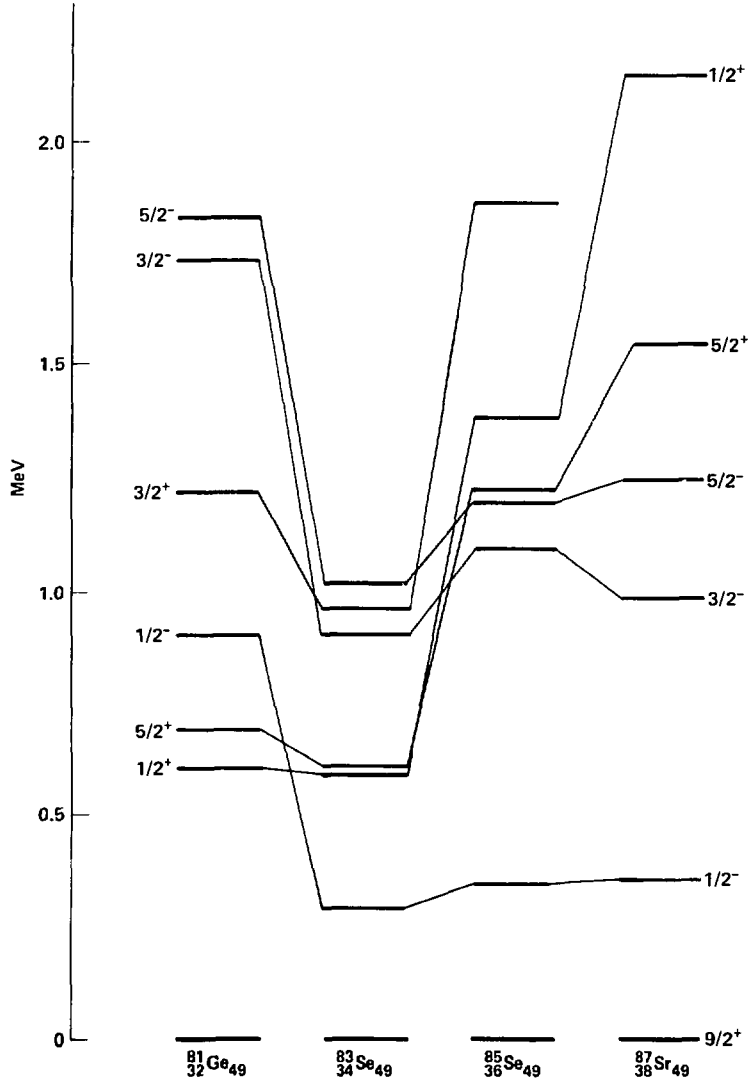

Fig. VII.8. Theoretical N=49 level systematics showing the lowest natural levels of spin and parity 9/2⁺, 1/2⁻, 3/2⁻, and 5/2⁻, and the lowest intruder states of spin and parity 1/2⁺, 3/2⁺ and 5/2⁺.

VIII. Future Experiments

Several more experiments are needed to further illuminate shape coexistence in the N=50 region. In these experiments particular attention should be given to determining level lifetimes and *M1/E2* ratios as required for a more detailed comparison with the theoretical predictions. Also, a specific search needs to be made for the missing $1/2^+$, $7/2^+$, and $11/2^-$ spectroscopic factor. Where gamma rays are observed angular correlation/distribution of the gamma rays must be observed. Only with this information will it be possible to check the theoretical gamma-ray transition intensities.

The following studies would be useful in studying the N=49 isotones:

- $^{82}Se(n,\gamma)^{83}Se$ — This experiment would locate the low spin states, particularly to confirm the few $1/2^+$ states which have been found and are predicted by the unified model. The gamma rays should also cascade through the $1/2^+$ states which have no observable [(0,0)0,$1/2^+$] component.
- $^{82}Se(d,p\gamma)^{83}Se$ — to study the $3/2^+$ and $5/2^+$ states which are predominately populated in this experiment. This experiment would give a clearer picture of the intruder structure as the intruder component is directly populated, rather than the natural component as in the β decay experiment I performed. Also possible are the (t,d) and (t,dγ) experiments. These later experiments should locate the $7/2^+$ spectroscopic factor, if it is present.
- $^{86}Kr(n,\alpha\gamma)^{83}Se$ — to study the more complex states which may not be excited by the neutron transfer reactions mentioned above. This reaction will be difficult as the reaction has Q = −2.7 MeV and krypton is a difficult target to use.
- $^{84}Kr(\vec{d},p)$, $^{86}Kr(\vec{p},d)$, $^{84}Kr(d,p\gamma)$, and $^{86}Kr(p,d\gamma)^{85}Kr$ — reactions to study the development of the collective intruder structure in transition. Some of these experiments have been done but incompletely; neither polarized projectiles nor in-beam gamma rays have been used.
- Identification of other 7/2 levels in the N=49 nuclei would shed light on the extent to which vibrational structure of the natural levels is affected by changing collectivity in these nuclei.

For the N=51 nuclei, which have a single particle outside the closed shell, the conjugate structure to that found in the N=49 nuclei is expected, with the particle and hole states being the natural and intruder states respectively. To the extent that the shell closure at Z=40 affects the intruder structure as it does for the N=49 isotones, the most likely candidates for study are ^{95}Ru and ^{97}Pd.

The following studies would be useful in studying the N=51 isotones:

Studies of levels ^{95}Ru have been studied using β^+ decay (WEI75), (p,d) (BAL71), and (α,nγ) (LED71). Only the β^+ decay study is relatively complete. The (α,nγ) reaction revealed only four levels.

- $^{96}Ru(\vec{p},d)^{95}Ru$ and $^{96}Ru(p,d\gamma)^{95}Ru$ to find the intruder states and their bands, with the polarized protons to determine the correct spins.
- $^{94}Mo(\alpha,3n\gamma)^{95}Ru$ and a more careful study with the $^{92}Mo(\alpha,n\gamma)^{95}Ru$ reaction might reveal more of the band structure.
- $^{96}Ru(n,2n)^{95}Ru$, $^{96}Ru(n,2n\gamma)^{95}Ru$ are also possible studies.
- $^{96}Ru(^3He,2n\gamma)^{97}Pd$ and $^{96}Ru(\alpha,3n\gamma)^{97}Pd$ reactions would give spins and parities and transition intensities. The $^{96}Ru(^3He,2n\gamma)$ was done by Fettweis et al. (FET82).

IX. Conclusions

In this thesis work I have developed AUTOBATCH, which utilized computer controlled automation to chemically prepare large numbers of replicate samples of short lived fission products for gamma-ray spectroscopy. With AUTOBATCH the gamma rays following the β^- decay of $^{83}_{33}As_{50}$ were studied to determine:

- the ground state spin and parity of ^{83}As to be $5/2^-$;
- the absolute intensity of the β^- branch from ^{83}As to $^{83}Se^m$ to be 0.3%;
- the absolute intensity of the ground state β^- branch from $^{83}Se^m$ to ^{83}Br to be 38% through a better normalization;
- the half-life of the $5/2_1^+$ level to be 3.2 ns;
- the structure of $^{83}_{34}Se_{49}$.

The results are used to show that the intruder vibrational structure which had been previously observed in the odd mass $_{49}$In isotopes could be observed in the N=49 isotones. The intruder vibrational structure is most strongly developed, not at core mid-shell, $^{89}_{40}Zr_{49}$, but rather at core mid-sub-shell, $^{83}_{34}Se_{49}$. This difference is qualitatively understood to be due to the blocking of collectivity by the subshell closure at Z=40 which prevents the intruder vibrational structure from occurring in ^{87}Sr and ^{89}Zr.

Appendix 1. AUTOBATCH Details

Transport Capsule

The transport capsule, called a rabbit, was a hollow polyethylene cylinder 6.2 cm long by 2.8 cm diameter, with a mass of 21 g when loaded. Both ends had thin sections which were easily penetrated by the extraction needle. The rabbit caused two problems which were solved by modifying the handling equipment and procedures.

The rabbit traveled at 50 m/s, abrading polyethylene fuzz from the rabbit. This fuzz interfered with the photo sensors. Daily cleaning eliminated this problem.

The rabbit was sufficiently elastic that it bounced when it hit the receiver. This bouncing made it difficult to determine when the rabbit was stopped on the bottom of the receiver. The new receiver reduced both of these problems to acceptable levels.

Loader/Launcher

The original loader was a manually loaded single shot loader implemented with a "quick disconnect" fitting. Loading was so physically difficult that rabbits could only be loaded one a minute. Loading rabbits into the launcher required one person full time.

The new launcher was a modified NURE launcher. The rabbit was loaded through a breech operated by a pneumatic cylinder. A supply of rabbits was held in a gravity feed magazine above the breech. The magazine could be loaded in two minutes, without interrupting sample processing. A photosensor activated an audible alarm when there were three rabbits left in the magazine. The only difficulty with this launcher occurred when the magazine was allowed to run to empty. The last rabbit would not drop into the breech, causing the loader to jam. The major advantages were elimination of one worker and reduction of the loading time from sixty to five seconds. Recycle times down to 15 s were not limited by the launcher.

Receiver

Original Receiver

The old receiver used a three position moving block assembly to manipulate the rabbit. The rabbit was received in the first position. When the receiver photosensor detected the rabbit in the receiver the program allowed a fixed delay time for the rabbit to settle down in the receiver. After the delay the block was moved to the second position where the extraction needle was inserted into the rabbit. After the chemistry was completed the needle was removed and the block moved to the third position where the rabbit dropped into a waste container. The block then returned to the first position.

This receiver was unsafe at any speed. After the receive step the rabbits frequently jammed either because the transport capsules were not at the bottom of the receiver or because the capsule cover had popped. At the third step the rabbit frequently failed to drop out of the receiver, again causing the receiver to jam. For long-lived nuclides these problems could be reduced to an acceptable level. For short-lived nuclides these problems were compounded by impact damage from moving the block too fast. This block weighed 2 kg, which the pneumatic cylinder slammed very hard at all but the slowest speeds. This slamming jarred position sensors out of alignment resulting in progressive self-destruction. A less massive block was tried with no significant improvement. A further unavoidable problem was the excessive time required for the needle to penetrate the capsule.

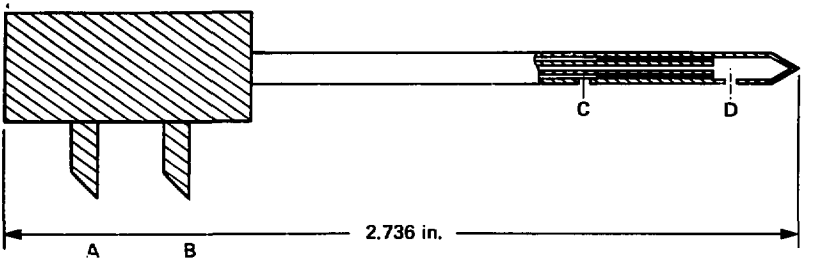

Fig. A1.1. The extraction needle. The outer part of the needle is a single piece, formed from hypodermic needle tubing. The tip is formed by cold flow in a dye. Tubes A and B are side arms for connecting to the rest of the system. Ports C and D are for extraction and venting respectively.

New Receiver

The new receiver shown in Fig. II.6 avoided the problems of the original receiver by having but one moving part, the flapper, and it moved only during the dump step. The new receiver was a box forming the end for the transport tube. The extraction needle was fixed upright in the bottom of the box. The rabbit's own momentum impaled it on the needle. The gas pressure behind the rabbit prevented its rebounding from the needle. When the sample was processed the flapper was moved to the dump position and a blast of air ejected the rabbit to a waste container. This new receiver eliminated most of the faults of the old receiver, and when it did fail, it did not jam; it merely wasted a sample. The flapper was light and required motions could all be made when the moves were not time critical, greatly reducing the strain on the receiver.

Needle

The needle (shown in Fig. A1.1) was used to extract the liquid sample from the polyethylene sample capsule. The needle consists of a double concentric needle proper and a base with two side arms for connecting the needle to the chemistry apparatus. These pieces were silver-soldered together. The double concentric design was necessary to vent the sample capsule. Attempts were made using nitrogen pressure to help force the sample out. However, when the pressure was great enough to measurably speed the extraction, an unacceptable amount of the sample leaked around the needle and out of the capsule.

The only improvement to the original needle was to alter the construction of the exterior tube. Initially, for ease of construction, it was made in two pieces, a tip and a shank. The tip was formed by crimping the tube, giving a blade shape to the tip. Failures due to both these features were frequent. I converted to a single exterior piece with the tip closed in a conical dye. With these changes a needle would last for 200 to 500 samples.

Original Still

The original still used in the hydride chemistry is shown in Fig. A1.2. It had two major drawbacks. Sparging was slow because of the size of the still (~150 ml), because the liquid remained in a lump at the bottom of the still and because considerable fraction of the liquid remained in the channels between the valves and the interior of the still. Slow sparging limited the speed of the chemistry and increased the noble gas contamination.

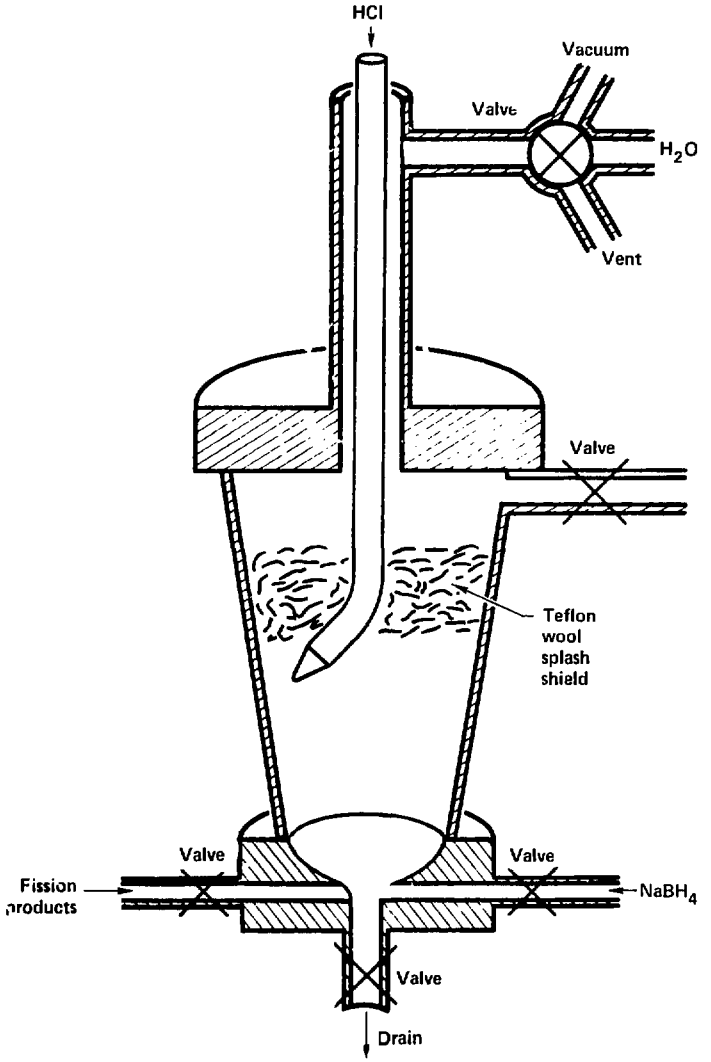

Fig. A1.2. One of the early versions of the hydride still. Total size and gravity separation of the gas-liquid mixture were problems to be overcome.

Further, the gas-liquid separation was achieved by gravity alone. If the hydride formation was not carefully controlled the gas-liquid mixture was blown out the hydride exit before separation. This ruined the current sample and soaked the stripping tube, requiring a replacement. These problems were both overcome with the new still and cyclone, described in Chapter II.

Sample Cell

The sample cell was made from a section of 6 mm polyethylene tubing. The sample cell was formed by heating the tubing and blowing a bubble of approximately 1 cm diameter. The bubble was then filled with a glass wool plug which was held in place by a piece of plastic "Chore-Boy". The sample cell was easy to make and when it failed it could easily be replaced. A more elaborate sample cell would have been more likely to leak, and being larger, would have presented greater difficulties to installation.

Appendix 2. Beta Decay of $^{83}Se^{m}$

In determining the absolute β^- intensity from ^{83}As to $^{83}Se^{m}$ it was necessary to use the absolute gamma-ray intensities following the beta decay of $^{83}Se^{m}$. Use of the tabulated values (NDS75a, TOI78) resulted in an answer that was approximately 5 sigma negative for the β^- intensity of interest. After careful checking of my data and analysis revealed no errors, the source of the absolute gamma intensities were checked. The direct (SCH68) and gamma deduced (MEY78, TOI78, NDS75a) beta intensities did not agree. Since the gamma-ray measurements give more accurate results the results were combined. Further investigation revealed the source of the error and resulted in an improved value for the absolute ground state intensity for the β^- decay of $^{83}Se^{m}$.

The direct β^- intensity measurement (SCH68) yielded relative intensities of 31%, 34%, and 35% to level groups at 0, 1, and 2 MeV. These relative intensities were compared to a decay scheme, showing good agreement. The relative intensities were then taken as absolute intensities. Although the decay scheme for $^{83}Se^{m}$ has changed radically since the β^- measurement was made, the ground state β^- intensity is still cited as 31% absolute. Using this value, the β^- intensities deduced from a current decay scheme are 31%, 48%, and 20% to the levels at 0, 1, and 2 MeV, where levels at 0.356, 1.66, and 2.88 have been ignored. The errors for these intensities are much less than the differences between the two sets of values.

The data sets can be brought into agreement by treating all of the intensities as relative and requiring that the observed β^- intensity supply exactly the β^- intensity deduced from the decay scheme (i.e. 34% = 48%) and disregard the direct β^- intensity measurement to the levels at 2 MeV. This procedure yields an absolute ground state β^- intensity of (39 ± 2)% using the data from Ref. MEY78. The absolute intensity to the level groups at 1 and 2 MeV is then 43% and 18% respectively.

The error is due to failure to correct for the spectral contamination from ^{81}Se decay due to the ^{80}Se component in the enriched ^{82}Se target. Schussler states that he irradiated an 89.1% enriched ^{82}Se target in thermal neutrons for 2 min., waited for 1.5 min for the 17 s activity due to ^{77}Se to decay away, then counted for two periods of 2 min. separated by 1 min., the second counting period to correct for long lived activity. He does not give an isotopic analysis of the target nor an explanation of how he corrected for the ^{81}Se activity. Apparently, no correction was made for long lived contamination. From isotopic analyses of similar targets made at Oak Ridge National Laboratory, a reasonable analysis of Schusslers target would be 89.1% ^{82}Se, 5.5% ^{80}Se, 3.4% ^{78}Se, 0.9% ^{77}Se, 1.1% ^{76}Se, and $< .1\%$ ^{74}Se based on the isotopic analysis of a sample 87.8% enriched ^{82}Se. (Ref. ADA83). Only the ^{80}Se contamination has a significant effect on the β^- spectrum. The expected relative intensities of the 1.585 MeV β^- from ^{81}Se and the 1.87 MeV β^- from ^{83}Se can be calculated from

$$N = \frac{N_0 \phi \sigma}{\lambda}(1 - e^{-\lambda t_i})(e^{-\lambda t_1} - e^{-\lambda t_f})I_\beta \qquad \text{(A2.1)}$$

Where N_0 is the number of target atoms, ϕ is the flux, σ is the capture cross section, λ is the decay constant, t_i is the irradiation time, t_1 and t_f are the times of the beginning and ending of the counting period, and I_β is the absolute β^- intensity. Obtaining values for β^- intensity for ^{81}Se, cross-section and half-life from Ref. TOI78, the intensity ratio of 1.58 MeV β^- from ^{81}Se to the 1.87 MeV β^- from $^{83}Se^{m}$ is 2.1. Comparing Schussler's work and the intensity deduced from the decay scheme, this ration is 1.5.

This good agreement (considering the large uncertainties involved, i.e. 25% in the $^{82}Se(n,\gamma)^{83}Se^{m}$ cross-section) confirms that the method used here gives the best available absolute ground state β^- intensity for the decay of $^{83}Se^{m}$.

Appendix 3. Model Configurations for ^{83}Se

Appendix 3: Theoretical configurations for states in ^{83}Se. Levels up to 3 MeV are included. The abbreviations used are T, theoretical, and X, experimental. Footnotes are at the end of the table.

Level:	$1/2_1^+$	
Energy:	T: 531	X: 540[a]
(2J + 1)S	T: 0.31	X: 0.56[b]

State	C	C^2
[(0,0)1/2$^+$]	−0.395	0.156
[(1,2)5/2$^+$]	−0.620	0.385
[(1,2)3/2$^+$]	+0.261	0.068
[(2,0)1/2$^+$]	+0.310	0.096
[(2,2)5/2$^+$]	+0.396	0.157
[(3,2)5/2$^+$]	−0.234	0.055
	sum =	0.916

Level:	$1/2_2^+$	
Energy:	T: 2671	
(2J + 1)S	T: 0.46	

State	C	C^2
[(2,4)9/2$^+$]	+0.252	0.064
[(0,0)1/2$^+$]	−0.479	0.229
[(1,2)5/2$^+$]	−0.331	0.109
[(2,0)1/2$^+$]	+0.383	0.147
[(2,2)5/2$^+$]	−0.274	0.075
[(3,2)5/2$^+$]	+0.548	0.300
	sum =	0.924

Level:	$1/2_3^+$	
Energy:	T: 2751	
(2J + 1)S	T: 0.04	

State	C	C^2
[(2,4)9/2$^+$]	−0.864	0.746
[(3,4)9/2$^+$]	−0.253	0.064
[(0,0)1/2$^+$]	−0.144	0.021
[(2,0)1/2$^+$]	+0.199	0.039
[(2,2)5/2$^+$]	+0.192	0.037
[(3,2)5/2$^+$]	+0.252	0.063
	sum =	0.971

Level:	$1/2_4^+$	
Energy:	T: 2841	
(2J + 1)S	T: 0.10	

State	C	C^2
[(2,4)9/2$^+$]	+0.247	0.061
[(0,0)1/2$^+$]	+0.227	0.052
[(1,2)5/2$^+$]	−0.187	0.035
[(1,2)3/2$^+$]	0.394	0.155
[(2,0)1/2$^+$]	−0.231	0.054
[(2,2)5/2$^+$]	+0.552	0.304
[(2,2)3/2$^+$]	+0.269	0.073
[(2,4)7/2$^+$]	−0.266	0.071
[(3,0)1/2$^+$]	+0.136	0.019
[(3,2)3/2$^+$]	−0.164	0.027
[(3,3)5/2$^+$]	+0.332	0.110
[(3,4)7/2$^+$]	+0.158	0.025
	sum =	0.984

Level:	$3/2_1^+$	
Energy:	T: 887	X: 1100[a]
(2J + 1)S	T: 0.22	X: 0.60[b]

State	C	C^2
[(0,0)3/2$^+$]	+0.235	0.055
[(1,2)7/2$^+$]	+0.164	0.027
[(1,2)5/2$^+$]	−0.275	0.076
[(1,2)3/2$^+$]	−0.175	0.031
[(1,2)1/2$^+$]	+0.439	0.192
[(2,0)3/2$^+$]	+0.200	0.040
[(2,2)5/2$^+$]	+0.244	0.059
[(2,2)3/2$^+$]	+0.153	0.023
[(2,2)1/2$^+$]	−0.192	0.037
[(2,4)5/2$^+$]	+0.539	0.291
[(3,2)1/2$^+$]	+0.179	0.032
[(3,4)5/2$^+$]	−0.283	0.080
	sum =	0.944

Level:	$3/2_2^+$	
Energy:	T: 1895	X: 1472[a]
(2J + 1)S	T: 0.03	X: d

State	C	C^2
[(2,4)9/2$^+$]	+0.140	0.020
[(0,0)3/2$^+$]	+0.085	0.007
[(1,2)5/2$^+$]	−0.304	0.092
[(1,2)3/2$^+$]	−0.273	0.075
[(1,2)1/2$^+$]	−0.229	0.052
[(2,2)5/2$^+$]	−0.342	0.117
[(2,2)3/2$^+$]	−0.171	0.029
[(2,2)1/2$^+$]	−0.494	0.244
[(2,4)7/2$^+$]	−0.150	0.022
[(2,4)5/2$^+$]	−0.163	0.026
[(3,2)3/2$^+$]	−0.108	0.012
[(3,3)5/2$^+$]	−0.463	0.215
[(3,3)3/2$^+$]	0.137	0.019
[(3,4)5/2$^+$]	0.193	0.037
	sum	0.997

Level:	$3/2_3^+$		
Energy:	T: 2373	X:	1710[a]
(2J+1)S	T: 0.03		
State	C		C^2
[(2,4)9/2+]	+0.326		0.106
[(0,0)3/2+]	−0.063		0.004
[(1,2)5/2+]	−0.649		0.422
[(1,2)3/2+]	+0.190		0.036
[(1,2)1/2+]	+0.128		0.016
[(2,2)5/2+]	+0.421		0.177
[(2,2)3/2+]	−0.189		0.036
[(2,4)7/2+]	+0.181		0.033
[(2,4)5/2+]	−0.248		0.061
[(3,3)5/2+]	+0.175		0.031
[(3,4)7/2+]	−0.125		0.016
[(3,4)5/2+]	+0.172		0.030
	sum =		0.967

Level:	$3/2_4^+$		
Energy:	T: 2861		
(2J+1)S	T: 0.02		
State	C		C^2
[(2,4)9/2+]	+0.887		0.787
[(3,4)9/2+]	+0.225		0.050
[(0,0)3/2+]	−0.071		0.005
[(1,2)5/2+]	+0.200		0.040
[(2,2)5/2+]	−0.201		0.041
[(2,2)1/2+]	+0.115		0.013
[(2,4)5/2+]	+0.159		0.025
	sum =		0.961

Level:	$3/2_5^+$		
Energy:	T: 2985	X:	2536[a]
(2J+1)S	T: 0.78	X:	1.98[b]
State	C		C^2
[(0,0)3/2+]	−0.442		0.196
[(1,2)7/2+]	−0.405		0.164
[(1,2)3/2+]	+0.238		0.057
[(2,0)3/2+]	−0.273		0.074
[(2,2)7/2+]	+0.207		0.043
[(2,2)5/2+]	+0.189		0.036
[(2,2)1/2+]	−0.258		0.067
[(2,4)7/2+]	+0.155		0.024
[(2,4)5/2+]	+0.233		0.054
[(3,2)7/2+]	−0.144		0.021
[(3,4)5/2+]	−0.475		0.226
	sum =		0.960

Level:	$5/2_1^+$		
Energy:	T: 588	X:	562[a]
(2J+1)S	T: 1.59	X:	2.76[b]
State	C		C^2
[(1,2)9/2+]	+0.159		0.025
[(0,0)5/2+]	0.515		0.265
[(1,2)5/2+]	+0.481		0.231
[(1,2)1/2+]	−0.343		0.117
[(2,0)5/2+]	−0.300		0.090
[(2,2)5/2+]	−0.121		0.015
[(2,2)1/2+]	+0.210		0.044
[(2,4)5/2+]	−0.277		0.077
[(2,4)3/2+]	+0.177		0.032
[(3,2)5/2+]	+0.158		0.025
[(3,2)1/2+]	−0.133		0.018
[(3,4)5/2+]	+0.101		0.010
	sum =		0.949

Level:	$5/2_2^+$		
Energy:	T: 1378	X:	1331[a]
(2J+1)S	T: 0.00	X:	0.33[b]
State	C		C^2
[(1,2)9/2+]	+0.909		0.827
[(2,2)9/2+]	+0.234		0.055
[(2,4)9/2+]	+0.114		0.013
[(1,2)5/2+]	−0.208		0.043
[(2,2)5/2]	−0.149		0.022
[(2,2)1/2+]	−0.125		0.016
	sum =		0.975

Level:	$5/2_3^+$		
Energy:	T: 1551	X:	1665[a]
(2J+1)S	T: 0.09	X:	0.38[b]
State	C		C^2
[(1,2)9/2+]	−0.242		0.059
[(0,0)5/2+]	+0.124		0.015
[(1,2)5/2+]	−0.346		0.120
[(1,2)1/2+]	−0.360		0.130
[(2,2)5/2+]	−0.589		0.347
[(2,2)1/2+]	−0.218		0.048
[(2,4)5/2+]	−0.187		0.035
[(2,4)3/2+]	+0.196		0.039
[(3,0)5/2+]	+0.118		0.014
[(3,2)1/2+]	−0.147		0.022
[(3,3)5/2+]	−0.329		0.108
[(3,3)3/2+]	+0.122		0.015
[(3,4)5/2+]	+0.109		0.012
	sum =		0.962

Level:	$5/2_4^+$		
Energy:	T: 2184	X:	2482[a]
(2J+1)S	T: 2.77	X:	0.47[b]
State	C		C^2
[(1,2)9/2+]	−0.115		0.013
[(0,0)5/2+]	−0.700		0.491
[(2,0)5/2+]	+0.431		0.186
[(2,2)1/2+]	−0.203		0.041
[(2,4)5/2+]	+0.235		0.055
[(3,2)7/2+]	0.351		0.123
[(3,2)1/2+]	+0.165		0.027
[(3,4)5/2+]	0.115		0.013
	sum =		0.949

Level: $5/2_5^+$
Energy: T: 2366
$(2J+1)S$ T: 0.00

State	C	C^2
[(1,2)5/2$^+$]	+0.120	0.014
[(1,2)3/2$^+$]	+0.367	0.135
[(2,0)5/2$^+$]	+0.104	0.011
[(2,2)7/2$^+$]	+0.174	0.030
[(2,2)5/2$^+$]	+0.271	0.073
[(2,2)3/2$^+$]	+0.241	0.058
[(2,2)1/2$^+$]	−0.315	0.099
[(2,4)7/2$^+$]	+0.130	0.017
[(2,4)5/2$^+$]	−0.513	0.263
[(2,4)3/2$^+$]	−0.132	0.018
[(3,0)5/2$^+$]	−0.209	0.044
[(3,2)3/2$^+$]	+0.148	0.022
[(2,2)3/2$^+$]	+0.137	0.019
[(3,3)7/2$^+$]	+0.137	0.019
[(3,3)5/2$^+$]	−0.258	0.067
[(3,3)1/2$^+$]	−0.250	0.062
[(3,4)5/2$^+$]	−0.200	0.040
	sum =	0.9906

Level: $5/2_6^+$
Energy: T: 2733 X: 2741[b]
$(2J+1)S$ T: 0.13 X: 0.21[b]

State	C	C^2
[(1,2)9/2$^+$]	−0.154	0.024
[(2,2)9/2$^+$]	+0.201	0.040
[(2,4)9/2$^+$]	+0.331	0.110
[(3,2)9/2$^+$]	+0.111	0.012
[(0,0)5/2$^+$]	−0.149	0.022
[(1,2)7/2$^+$]	+0.115	0.013
[(1,2)5/2$^+$]	−0.194	0.038
[(1,2)3/2$^+$]	−0.125	0.016
[(2,0)5/2$^+$]	−0.524	0.275
[(2,2)5/2$^+$]	+0.156	0.024
[(2,2)1/2$^+$]	−0.287	0.083
[(2,4)5/2$^+$]	+0.269	0.072
[(3,0)5/2$^+$]	−0.211	0.045
[(3,2)5/2$^+$]	+0.219	0.048
[(3,2)1/2$^+$]	+0.120	0.014
[(3,4)5/2$^+$]	−0.326	0.106
	sum =	0.941

Level: $5/2_7^+$
Energy: T: 2847
$(2J+1)S$ T: 0.01

State	C	C^2
[(1,2)9/2$^+$]	0.176	0.031
[(2,2)9/2$^+$]	−0.564	0.318
[(2,4)9/2$^+$]	−0.605	0.366
[(3,3)9/2$^+$]	−0.202	0.041
[(3,4)9/2$^+$]	+0.130	0.017
[(0,0)5/2$^+$]	+0.047	0.002
[(2,0)5/2$^+$]	+0.208	0.043
[(2,2)1/2$^+$]	+0.235	0.055
[(2,4)5/2$^+$]	−0.141	0.020
[(3,2)5/2$^+$]	−0.103	0.011
[(3,3)5/2$^+$]	+0.113	0.013
[(3,4)5/2$^+$]	+0.204	0.041
	sum =	0.958

Level: $5/2_8^+$
Energy: T: 2883
$(2J+1)S$ T: 0.00

State	C	C^2
[(2,4)9/2$^+$]	+0.125	0.016
[(2,2)9/2$^+$]	−0.700	0.489
[(2,4)9/2$^+$]	+0.674	0.454
[(2,4)3/2$^+$]	+0.109	0.012
	sum =	0.972

Level: $7/2_1^+$
Energy: T: 1300 X: 1265[a]
$(2J+1)S$ T: 0.11 X: <0.16[d]

State	C	C^2
[(1,2)9/2$^+$]	+0.221	0.049
[(0,0)7/2$^+$]	−0.118	0.014
[(1,2)5/2$^+$]	−0.550	0.302
[(1,2)3/2$^+$]	−0.292	0.085
[(2,2)5/2$^+$]	−0.267	0.071
[(2,2)3/2$^+$]	+0.126	0.016
[(2,4)5/2$^+$]	+0.477	0.227
[(2,4)1/2$^+$]	−0.301	0.091
[(3,2)5/2$^+$]	−0.163	0.027
[(3,3)1/2$^+$]	−0.146	0.021
[(3,6)5/2$^+$]	−0.289	0.083
	sum =	0.987

Level: $7/2_2^+$
Energy: T: 1440 X: 1822[a]
$(2J+1)S$ T: 0.03

State	C	C^2
[(1,2)9/2$^+$]	+0.934	0.873
[(2,4)9/2$^+$]	+0.138	0.019
[(0,0)7/2$^+$]	+0.060	0.004
[(1,2)3/2$^+$]	+0.116	0.013
[(2,2)5/2$^+$]	−0.100	0.010
[(2,4)5/2$^+$]	−0.132	0.017
[(2,4)1/2$^+$]	+0.140	0.020
[(3,6)5/2$^+$]	−0.131	0.017
	sum =	0.972

Level:	$7/2_3^+$	
Energy:	T: 1793	
(2J+1)S	T: 0.06	
State	C	C^2
[(1,2)9/2+]	+0.224	0.050
[(0,0)7/2+]	−0.085	0.007
[(1,2)5/2+]	+0.311	0.097
[(1,2)3/2+]	−0.313	0.098
[(2,2)7/2+]	−0.110	0.012
[(2,2)5/2+]	+0.507	0.257
[(2,4)7/2+]	−0.142	0.020
[(2,4)3/2+]	+0.220	0.048
[(2,4)1/2+]	−0.359	0.129
[(3,2)3/2+]	−0.176	0.026
[(3,3)1/2+]	+0.191	0.036
[(2,4)1/2+]	−0.284	0.081
[(3,6)5/2+]	−0.314	0.099
	sum =	0.794

Level:	$7/2_4^+$	
Energy:	T: 2728	
(2J+1)S	T: 0.00	
State	C	C^2
[(2,2)9/2+]	+0.730	0.533
[(2,4)9/2+]	+0.513	0.263
[(3,3)9/2+]	−0.239	0.057
[(1,2)5/2+]	−0.146	0.021
[(3,3)7/2+]	+0.198	0.039
[(3,4)5/2+]	−0.147	0.022
[(3,6)5/2+]	+0.128	0.016
	sum =	0.952

Level:	$7/2_5^+$	
Energy:	T: 2843	
(2J+1)S	T: 0.00	
State	C	C^2
[(2,2)9/2+]	−0.595	0.354
[(2,4)9/2+]	+0.680	0.463
[(1,2)7/2+]	+0.142	0.021
[(2,2)3/2+]	+0.162	0.026
[(2,4)1/2+]	+0.112	0.012
[(3,3)5/2+]	−0.177	0.031
[(3,6)5/2+]	+0.138	0.019
	sum =	0.927

Level:	$7/2_6^+$	
Energy:	T: 2978	
(2J+1)S	T: 0.21	
State	C	C^2
[(1,2)9/2+]	+0.105	0.011
[(2,4)9/2+]	−0.391	0.153
[(3,6)9/2+]	0.115	0.013
[(0,0)7/2+]	−0.161	0.026
[(1,2)7/2+]	+0.247	0.061
[(1,2)5/2+]	−0.154	0.024
[(2,2)5/2+]	+0.356	0.127
[(2,2)3/2+]	+0.269	0.072
[(2,4)5/2+]	+0.303	0.092
[(2,4)1/2+]	+0.352	0.124
[(3,4)7/2+]	−0.187	0.035
[(3,4)1/2+]	+0.223	0.050
[(3,6)5/2+]	+0.389	0.151
[(3,6)3/2+]	+0.389	0.151
	sum =	0.938

Level:	$9/2_1^+$	
Energy:	T: 0	X: 0
(2J+1)S	T: 1.87	X: 1.80[b]
State	C	C^2
[(0,0)9/2+]	+0.968	0.938
[(1,2)9/2+]	+0.234	0.055
	sum =	0.992

Level:	$9/2_2^+$	
Energy:	T: 1130	
(2J+1)S	T: 0.00	
State	C	C^2
[(0,0)9/2+]	−0.010	0.000
[(1,2)9/2+]	−0.214	0.046
[(1,2)5/2+]	−0.612	0.375
[(2,2)5/2+]	+0.260	0.067
[(2,4)5/2+]	+0.437	0.191
[(2,4)3/2+]	−0.105	0.011
[(2,4)1/2+]	−0.368	0.136
[(3,2)5/2+]	−0.189	0.036
[(3,4)1/2+]	−0.160	0.026
[(3,6)5/2+]	−0.223	0.050
[(3,6)3/2+]	+0.138	0.019
	sum =	0.956

Level:	$9/2_3^+$	
Energy:	T: 1455	X: 1527[a]
(2J+1)S	T: 0.12	
State	C	C^2
[(0,0)9/2+]	−0.244	0.059
[(1,2)9/2+]	+0.889	0.790
[(2,0)9/2+]	+0.162	0.026
[(2,2)9/2+]	−0.126	0.016
[(2,4)9/2+]	+0.212	0.045
[(1,2)5/2+]	−0.155	0.024
[(2,4)5/2+]	+0.109	0.012
[(2,4)1/2+]	−0.110	0.012
	sum	0.984

Level: $9/2_4^+$
Energy: T: 2290
$(2J+1)S$ T: 0.05

State	C	C^2
[(2,4)9/2$^+$]	+0.153	0.023
[(1,2)7/2$^+$]	−0.123	0.015
[(2,2)5/2$^+$]	+0.705	0.496
[(2,4)5/2$^+$]	+0.301	0.091
[(3,3)5/2$^+$]	−0.337	0.114
[(3,4)5/2$^+$]	+0.376	0.142
[(3,4)1/2$^+$]	+0.157	0.025
[(3,6)5/2$^+$]	+0.201	0.040
	sum =	0.945

Level: $9/2_5^+$
Energy: T: 2671
$(2J+1)S$ T: 0.00

State	C	C^2
[(2,0)9/2$^+$]	+0.129	0.017
[(2,2)9/2$^+$]	+0.682	0.466
[(2,4)9/2$^+$]	+0.195	0.038
[(3,0)9/2$^+$]	+0.123	0.015
[(3,4)9/2$^+$]	+0.138	0.019
[(1,2)5/2$^+$]	−0.120	0.014
[(2,2)5/2$^+$]	+0.134	0.018
[(2,4)5/2$^+$]	−0.394	0.155
[(2,4)1/2$^+$]	−0.229	0.052
[(3,3)5/2$^+$]	+0.253	0.064
[(3,4)5/2$^+$]	−0.248	0.062
[(3,4)1/2$^+$]	−0.149	0.022
[(3,6)5/2$^+$]	+0.131	0.017
	sum =	0.960

Level: $9/2_6^+$
Energy: T: 2803
$(2J+1)S$ T: 0.00

State	C	C^2
[(1,2)9/2$^+$]	−0.134	0.018
[(2,0)9/2$^+$]	+0.923	0.853
[(2,2)9/2$^+$]	−0.119	0.014
[(2,4)9/2$^+$]	−0.192	0.037
[(3,2)9/2$^+$]	+0.241	0.058
	sum =	0.980

Level: $9/2_7^+$
Energy: T: 2888
$(2J+1)S$ T: 0.00

State	C	C^2
[(1,2)9/2$^+$]	+0.236	0.056
[(2,0)9/2$^+$]	0.116	0.014
[(2,4)9/2$^+$]	−0.884	0.781
[(3,2)9/2$^+$]	−0.145	0.021
[(3,6)9/2$^+$]	−0.160	0.026
[(2,4)5/2$^+$]	−0.151	0.023
[(2,4)1/2$^+$]	−0.113	0.013
[(3,4)5/2$^+$]	−0.121	0.015
	sum =	0.947

Level: $9/2_8^+$
Energy: T: 2933
$(2J+1)S$ T: 0.00

State	C	C^2
[(1,2)9/2$^+$]	+0.142	0.020
[(2,2)9/2$^+$]	+0.626	0.392
[(3,0)9/2$^+$]	+0.105	0.011
[(1,2)5/2$^+$]	+0.103	0.011
[(2,2)9/2$^+$]	+0.194	0.038
[(3,0)9/2$^+$]	+0.341	0.116
[(2,4)1/2$^+$]	+0.385	0.148
[(3,3)5/2$^+$]	−0.283	0.080
[(3,4)5/2$^+$]	+0.288	0.083
[(3,4)1/2$^+$]	+0.177	0.031
[(3,6)3/2$^+$]	−0.144	0.021
	sum =	0.951

Level: $11/2_1^+$
Energy: T: 1275 X: 1297[a]

State	C	C^2
[(1,2)9/2$^+$]	+0.863	0.744
[(2,2)9/2$^+$]	−0.247	0.061
[(2,4)9/2$^+$]	+0.397	0.158
[(2,4)5/2$^+$]	−0.111	0.012
	sum =	0.975

Level: $11/2_2^+$
Energy: T: 2292

State	C	C^2
[(2,2)9/2$^+$]	−0.215	0.046
[(3,4)9/2$^+$]	−0.156	0.024
[(1,2)7/2$^+$]	+0.181	0.033
[(2,4)5/2$^+$]	+0.719	0.518
[(2,4)3/2$^+$]	+0.186	0.035
[(3,3)5/2$^+$]	−0.202	0.041
[(3,4)5/2$^+$]	+0.131	0.017
[(3,6)5/2$^+$]	−0.462	0.214
[(3,6)1/2$^+$]	+0.188	0.035
	sum =	0.963

Level: $11/2_3^+$
Energy: T: 2850

State	C	C^2
[(2,2)9/2+]	+0.716	0.513
[(2,4)9/2+]	+0.421	0.177
[(3,4)9/2+]	+0.164	0.027
[(3,6)9/2+]	+0.168	0.028
[(1,2)7/2+]	+0.186	0.035
[(2,4)3/2+]	+0.250	0.062
[(3,3)5/2+]	+0.172	0.030
[(3,4)5/2+]	−0.232	0.054
[(3,6)5/2+]	−0.151	0.023
[(3,6)1/2+]	+0.125	0.016
	sum =	0.965

Level: $11/2_4^+$
Energy: T: 3006

State	C	C^2
[(1,2)9/2+]	−0.477	0.227
[(2,2)9/2+]	−0.271	0.073
[(2,4)9/2+]	+0.649	0.421
[(3,2)9/2+]	+0.204	0.042
[(3,4)9/2+]	−0.256	0.066
[(3,6)9/2+]	+0.316	0.100
[(3,3)5/2+]	−0.133	0.018
	sum =	0.947

Level: $13/2_1^+$
Energy: T: 1306

State	C	C^2
[(2,2)9/2+]	+0.867	0.751
[(2,4)9/2+]	+0.207	0.043
[(3,2)9/2+]	+0.332	0.110
[(3,3)7/2+]	−0.259	0.067
	sum =	0.972

Level: $13/2_2^+$
Energy: T: 2219

State	C	C^2
[(2,2)9/2+]	+0.101	0.010
[(2,4)9/2+]	+0.190	0.036
[(3,2)9/2+]	+0.311	0.097
[(3,4)9/2+]	+0.140	0.020
[(3,3)7/2+]	+0.723	0.523
[(3,6)7/2+]	−0.231	0.054
[(3,6)3/2+]	−0.374	0.140
[(3,6)1/2+]	+0.107	0.011
[(1,2)9/2+]	+0.305	0.093
	sum =	0.984

Level: $13/2_3^+$
Energy: T: 2664

State	C	C^2
[(2,4)9/2+]	+0.748	0.560
[(3,2)9/2+]	−0.481	0.231
[(3,4)9/2+]	+0.226	0.051
[(3,6)9/2+]	+0.317	0.100
[(2,4)7/2+]	−0.205	0.042
[(3,6)7/2+]	−0.111	0.012
	sum =	0.997

Level: $13/2_4^+$
Energy: T: 3030

State	C	C^2
[(2,2)9/2+]	−0.472	0.222
[(2,4)9/2+]	+0.376	0.141
[(3,2)9/2+]	+0.575	0.330
[(3,3)9/2+]	+0.209	0.044
[(3,4)9/2+]	+0.199	0.039
[(2,4)7/2+]	+0.325	0.105
[(3,3)7/2+]	−0.253	0.064
[(3,6)7/2+]	−0.120	0.014
[(3,6)3/2+]	+0.130	0.017
[(1,2)9/2+]	−0.138	0.019
	sum =	0.997

Level: $1/2_1^-$
Energy: T: 229 X: 229
(2J+1)S T: 229 X: 0.11

State	C	C^2
[(0,0)1/2−]	+0.956	0.914
[(1,2)3/2−]	+0.190	0.036
[(1,2)5/2−]	−0.215	0.046
	sum =	0.996

Level: $1/2_2^-$
Energy: T: 2387

State	C	C^2
[(0,0)1/2−]	+0.249	0.062
[(1,2)3/2−]	−0.671	0.450
[(1,2)5/2−]	+0.345	0.119
[(2,0)1/2−]	−0.516	0.266
[(2,2)3/2−]	−0.216	0.047
[(2,2)5/2−]	+0.162	0.026
[(3,2)3/2−]	−0.108	0.012
[(3,2)5/2−]	+0.119	0.014
	sum =	0.937

Level: $1/2_3^-$
Energy: T: 2639

State	C	C^2
[(1,2)3/2−]	+0.609	0.371
[(1,2)5/2−]	+0.727	0.529
[(2,0)1/2−]	0.235	0.055
[(2,2)5/2−]	−0.167	0.028
	sum =	0.982

Level: $3/2_1^-$
Energy: T: 950 X: 963[a]

State	C	C^2
[(0,0)3/2]	+0.877	0.769
[(1,2)1/2]	−0.407	0.166
[(1,2)3/2]	+0.190	0.036
[(1,2)5/2]	+0.111	0.012
	sum =	0.983

Level: $3/2_2$
Energy: T: 1730

State	C	C^2
[(0,0)3/2]	+0.397	0.158
[(1,2)1/2]	+0.857	0.734
[(1,2)3/2]	+0.126	0.016
[(2,2)3/2]	+0.157	0.025
[(2,4)5/2]	−0.207	0.043
	sum =	0.975

Level: $3/2_3$
Energy: T: 2363

State	C	C^2
[(0,0)3/2]	−0.245	0.060
[(1,2)3/2]	+0.747	0.558
[(1,2)5/2]	+0.238	0.057
[(2,0)3/2]	+0.136	0.019
[(2,2)1/2]	−0.519	0.270
[(2,4)5/2]	+0.105	0.011
	sum =	0.974

Level: $3/2_4^-$
Energy: T: 2744

State	C	C^2
[(1,2)3/2]	−0.424	0.180
[(1,2)5/2]	+0.864	0.747
[(2,2)1/2]	−0.179	0.032
[(2,2)3/2]	−0.121	0.015
[(2,2)5/2]	+0.140	0.020
	sum =	0.994

Level: $5/2_1^-$
Energy: T: 1100 X: 1063[a]

State	C	C^2
[(0,0)5/2]	+0.823	0.677
[(1,2)1/2]	−0.500	0.250
[(1,2)3/2]	−0.109	0.012
[(1,2)5/2]	+0.190	0.036
	sum =	0.975

Level: $5/2_2^-$
Energy: T: 1770

State	C	C^2
[(0,0)5/2]	+0.488	0.238
[(1,2)1/2]	+0.805	0.648
[(1,2)5/2]	+0.151	0.023
[(2,2)5/2]	−0.149	0.022
[(2,4)3/2]	+0.171	0.029
[(2,4)5/2]	−0.114	0.013
	sum =	0.973

Level: $5/2_3^-$
Energy: T: 2401

State	C	C^2
[(0,0)5/2]	+0.220	0.049
[(1,2)3/2]	+0.790	0.624
[(1,2)5/2]	−0.258	0.067
[(2,2)1/2]	+0.431	0.186
[(2,2)3/2]	−0.132	0.017
[(2,4)3/2]	+0.162	0.026
	sum =	0.968

Level: $5/2_4^-$
Energy: T: 2520

State	C	C^2
[(0,0)5/2]	−0.143	0.020
[(1,2)3/2]	+0.468	0.219
[(1,2)5/2]	+0.714	0.511
[(2,2)1/2]	−0.401	0.160
[(2,2)3/2]	−0.143	0.021
[(2,4)5/2]	+0.179	0.032
	sum =	0.962

Level: $5/2_5^-$
Energy: T: 3288

State	C	C^2
[(0,0)5/2]	−0.107	0.012
[(1,2)3/2]	−0.208	0.043
[(1,2)5/2]	+0.533	0.284
[(2,0)5/2]	+0.147	0.022
[(2,2)1/2]	+0.740	0.547
[(3,3)3/2]	+0.122	0.015
[(3,3)5/2]	−0.137	0.019
[(3,4)3/2]	+0.137	0.019
	sum =	0.943

Level: $7/2_1$
Energy: T: 1821 X: 2077[a]

State	C	C^2
[(1,2)3/2]	+0.672	0.452
[(1,2)5/2]	+0.158	0.025
[(2,2)3/2]	+0.121	0.015
[(2,4)1/2]	0.579	0.335
[(2,4)3/2]	+0.238	0.057
[(2,4)5/2]	+0.169	0.029
[(3,3)3/2]	+0.103	0.011
[(3,4)5/2]	+0.222	0.049
	sum	0.972

Level:	$7/2_2$		
Energy:	T: 2544	X: 2981[a]	
State	C	C^2	
[(1,2)3/2]	+0.233	0.054	
[(1,2)5/2]	+0.768	0.590	
[(2,2)3/2]	+0.149	0.022	
[(2,2)5/2]	−0.345	0.119	
[(2,4)3/2]	−0.262	0.068	
[(2,4)5/2]	+0.278	0.077	
[(3,3)1/2]	−0.226	0.051	
	sum =	0.982	

Level:	$7/2_3$		
Energy:	T: 3311	X: 2858[a]	
State	C	C^2	
[(1,2)3/2]	+0.305	0.093	
[(1,2)5/2]	+0.119	0.014	
[(2,2)3/2]	+0.406	0.165	
[(2,4)1/2]	+0.597	0.356	
[(2,4)3/2]	+0.285	0.081	
[(2,4)5/2]	+0.237	0.056	
[(3,3)3/2]	+0.195	0.038	
[(3,3)5/2]	+0.110	0.012	
[(3,4)1/2]	−0.346	0.120	
[(3,6)5/2]	−0.208	0.043	
	sum =	0.979	

Level:	$7/2_4$		
Energy:	T: 3685	X: 3243[a]	
State	C	C^2	
[(1,2)3/2]	+0.350	0.122	
[(1,2)5/2]	−0.204	0.042	
[(2,2)3/2]	+0.674	0.454	
[(2,2)5/2]	+0.165	0.027	
[(2,4)1/2]	−0.258	0.067	
[(2,4)3/2]	−0.129	0.017	
[(2,4)5/2]	−0.156	0.024	
[(3,3)3/2]	+0.133	0.018	
[(3,4)1/2]	−0.289	0.084	
[(3,4)3/2]	+0.286	0.082	
[(3,4)5/2]	+0.208	0.043	
	sum =	0.979	

Level:	$9/2_1$	
Energy:	T: 1929	
State	C	C^2
[(1,2)5/2]	+0.644	0.415
[(2,2)5/2]	+0.123	0.015
[(2,4)1/2]	−0.621	0.386
[(2,4)3/2]	−0.166	0.027
[(2,4)5/2]	+0.234	0.055
[(3,2)5/2]	+0.107	0.011
[(3,6)3/2]	−0.220	0.048
[(3,6)5/2]	+0.124	0.016
	sum =	0.974

Level:	$9/2_2$	
Energy:	T: 3380	
State	C	C^2
[(1,2)5/2]	0.370	0.137
[(2,2)5/2]	+0.341	0.116
[(2,4)1/2]	+0.577	0.333
[(2,4)3/2]	−0.291	0.085
[(2,4)5/2]	+0.321	0.103
[(3,3)5/2]	+0.175	0.031
[(3,4)1/2]	−0.353	0.125
[(3,4)5/2]	−0.111	0.012
[(3,6)3/2]	+0.164	0.027
[(3,6)5/2]	−0.123	0.015
	sum =	0.984

Notes:

[a] This work.

[b] MON78.

[c] LIN65.

[d] Estimated from Fig. 18 in Ref. MON78.

References

ADA83 Adair, H., private communication The isotopic analysis of an 87.8% enriched ^{82}Se sample produced at Oak Ridge National Laboratory in 1964.

BAL71 Ball, J. B., Nucl. Phys. **A160**, 225 (1971).
"Studies of ^{95}Ru and ^{94}Ru with the $^{96}Ru(p,d)$ and (p,t) Reactions."

BOH75 Bohr, A. and B. Mottleson, *Nuclear Structure* (Benjamin, New York, 1975), vol. 2, ch. 5.

CHO54 Choudhury, D. C., Dan. Mat. Fys. Medd. **28** (1954).
"Intermediate Coupling Calculations in the Unified Model."

FET82 Fettweis, I., P. del Marmol, M. Degreef, P. Duhamel, and J. Vanhorenbeeck, Z. Phys. **A305**, 57 (1982).
"Excited States in ^{97}Pd."

FOL69 Folger, H., J.-V. Kratz and G. Herrmann, Radiochem. Radioanal. Lett. 1, 185 (1969).
"Rapid Volatilization of Arsenic, Selenium, Antimony, and Tellurium in Form of Their Hydrides."

FRI65 Friedlander, G., J. W. Kennedy, and J. M. Miller, *Nuclear and Radiochemistry*, 2nd Ed., John Wiley and Sons, Inc., New York, 1965. p. 76.

GLA79 Glascock, M. D., E. W. Schneider, W. B. Walters, S. V. Jackson, and R. A. Meyer, Phys. Rev. **C20**, 2370 (1979).
"Level structure of odd-mass I i and the unified model. II. ^{117}In levels populated in the decay of ^{117}Cd isot

GRO68 Groshev, L. V., A. M. Demidov, V. I. Pelekhov, L. L. Sokolooskii, G. A. Bartholomew, A. Doveika, K. M. Eastwood, and S. Monaro, Atomic Data and Nuclear Data Tables **5**, 1 (1968).
"Compendium of Thermal-Neutron-Capture γ-Ray Measurements."

GUN72 Cunnink, R., and J. B. Niday, UCRL-51061, 1972. Especially Vol. 1., pp. 4-35, "Data Reduction."
"Computerized Quantitative Analysis by Gamma-ray Spectroscopy."

GUS81 Gustafsson, H.-A, T. Bjornstad, B. Jonson, O. C. Jonsson, V. Lindfors, S. Mattsson, A. M. Poskanzer, H. L. Ravn and D. Schardt, *Proceedings of the 4th Conference on Nuclei Far from Stability, Helsingor*, 704 (1981).
"Comparative Yields of Alkali Metals and Thallium from Uranium Irradiated with High-energy Protons, ^{3}He and ^{12}C."

HAR72 Harar, S., and R. N. Horoshko, Nucl. Phys. **A183**, 161 (1972).
"Study of the Level Scheme of ^{117}In via Proton Transfer Reactions."

HER69 Herrmann, G. and H. O. Denschlag, Ann. Rev. Nucl. Sci., **19**, 12 (1969).
"Rapid Chemical Separation."

HEY78 Heyde, K., M. Waroquier, and R. A. Meyer, Phys. Rev. C17, 1219 (1978).
"Unified description of odd-mass indium nuclei: I. General theory and comparison to ^{113}In and ^{115}In levels populated in the decay of ^{113}Sn and $^{115}Sn^{m,g}$."

HEY80 Heyde, K., M. Waroquier and P. Van Isacker, Phys. Rev. **C22**, 1267 (1980).
"Unified description of odd-mass indium nuclei: III. Application to $^{117-121}In$."

HEY82 Private communication the results of K. Heyde's model calculations for $^{83}Se_{49}$ and other $N = 49$ isotones

HOF81 Hoff, P., K. Aleklett, B. Folgelberg, E. Lund and G. Rudstam, *Proceedings of the 4th Conference on Nuclei Far from Stability, Helsingor*, 704 (1981).
"Decay properties of ^{81}Ga and ^{81}Ge and Observation of Abnormal Energy Shift in the P1/2 State."

HOF82 Hoff, P., private communication.

KON66 Konopinski, E. J., *The Theory of Beta Radioactivity*, Oxford University Press, 1966, p. 157.

KRA70 Kratz, J.-V. and G. Herrmann, J. Inorg. Nucl. Chem. **32**, 3713 (1970).
"Halflives, Fission Yields and Neutron Emission Probabilities of ^{87}Se, ^{88}Se and Evidence for ^{87}As."

KRA75 Kratz, J. V., H. Franz, N. Kaffrell, and G. Herrmann, Nucl. Phys. **A250**, 13 (1975).
"Gamma-ray Emission from $^{80-86}$As Isotopes."

LAN79 Lane, S. M., Thesis, Univ. of Calif. at Davis (1979).
"The Nuclear Structure of Tellurium 133 via Beta Decay and Shell Model Calculations in the Doubly Magic Tin 132 Region."

LED71 Lederer, C. M., J. M. Jaklevic, and J. M. Hollander, Nucl. Phys. **A169**, 489 (1971).
"In-beam Gamma-Ray Spectroscopy of Odd Neutron Mo and Ru Isotopes."

LIE79 Lien, III, O. G., High speed motion picture of the LLNL still and cyclone separator.

LIE80 Lien, III, O. G., P. C. Stephenson, E. A. Henry, R. P. Yaffe, and R. A. Meyer, Nucl. Instrum. Meth. **185**, 351 (1981).
"AUTOBATCH: I. System Description for the Automated Batchwise Isolation and Study of Short-Lived Fission Products."

LIN65 Lin, E. K., Phys. Rev. **139**, B340 (1965).
"Nuclear Structure Studies in the Selenium Isotopes with (d,p) and (d,t) Reactions."

LIN80 Lin, J., E. A. Henry and R. A. Meyer, UCRL-84536, submitted to the Sixth Conference on Application of Accelerators in Research and Industry, Denton, Texas, 1980.
"Detection Efficiency of Ge(Li) and HPGe Detectors for Gamma rays up to 10-MeV."

MAR74 Markham, R. G. and H. W. Fulbright, Phys. Rev. **C9**, 1633 (1974).
"Structure of ^{113}In Studied by the Reactions ^{115}In(p,t)^{113}In, ^{112}Cd(^{3}He,d)^{113}In, and ^{112}Cd(^{4}He t)^{113}In."

MAS80 Private communication, T. N. Massey.

MAT77 Matsuki S., N. Sakamoto, K. Ogino, Y. Kadota, Y. Saito, T. Tanabe, M. Yasue, and Y. Okuma, Phys. Lett. **72B**, 310 (1978).
"Systematics of Low Lying Octupole States in the Doubly-Even Nuclei from Ge to Sr."

MEY78 Meyer, R.A., LLNL publication M-100 (1978).
"Multigamma-ray Calibration Standards."

MEY79a Meyer, R. A., Lawrence Livermore National Laboratory, Livermore, California, Preprint UCRL-81069 (1979); presented at the Workshop on Nuclear Spectroscopy of Fission Products, Grenoble, France, May 1979.
"Rapid Automated Nuclear Chemistry."

MEY79b Meyer, R. A., E. A. Henry, O. G. Lien, III, H. C. Griffin, S. M. Lane, R. P. Yaffe, P. C. Stevenson, and G. Skarnemark, *Proceedings of the Conference on Future Directions in Studies of Nuclei Far From Stability, Nashville* (1979)
Properties of Neutron-Rich Nuclei Studied by Fission Product Nuclear Chemistry

MEY81 Private communication from R. A. Meyer, the results of gamma spectroscopy following the beta decay of $^{83}Se^{m}$ from $^{82}Se(n,\gamma)$.

MON78 Montestruque, L. A., M. C. Cobian-Rozak, G. Szaloky, J. D. Zumbro, and S. E. Darden, Nucl. Phys. **A305**, 29 (1978).
"Study of the $^{77,79,81,83}Se$ Level Structure with the $^{76,78,80,82}Se(\vec{d},p)$ Reaction."

NDS75 Nuclea Data Sheets, **16**, 445 (1975). A = 89.

NDS79 Nuclear Data Sheets, **27**, 389 (1979). A = 87.

NDS80a Nuclear Data Sheets, **30**, 413 (1980). A = 115.

NDS80b Nuclear Data Sheets, **34**, v (1981).

REE70 Reehal, B. S., and R. A. Sorenson, Phys. Rev. **C2**, 819 (1970).
"Electric Quadrupole Transitions in Odd-Mass Spherical Nuclei."

ROS78 Rosel, F., H. M. Fries, K. Alder, and H. C. Pauli, Atomic and Nuclear Data Tables, **21**, 385 (1985).
"Internal Conversion Coefficients for all Atomic Shells."

SCH68 Schussler, F., Le Journal de Physique, **29**, 385 (1968).
"Measurement of the beta transition intensities in the $^{83}Se^{m}$ by magnetic spectrometer."

STE77 Stevenson, P. C., private communication, program written for a Data General, Inc. NOVA 1200 mini computer.

STO80 Private communication, description of computer code FITEK.

SYM81 Symons, T. J. M., *Proceedings of the 4th Conference on Nuclei Far from Stability, Helsingor*, 668 (1981).
"Production of Nuclei Far from Stability by Fragmentation of High Energy Heavy Ions."

THU70 Thuriere, E., Thesis, University of Paris, as cited in Ref. NDS80a.

TIT77 Tittel, G., N. Kaffrell, N. Trautmann, and G. Herrmann, J. Inorg. Nucl. Chem. **39**, 2115 (1977).
"Direct Identification of $^{103-107}Mo$ by a Rapid Chemical Separation Procedure"

TRA78 N. Trautmann on a review of fast chemistry, in *Proceedings of the American Chemical Society, Miami* (1978).

TOI78 *Table of Isotopes*, 7th Ed., C. M. Lederer and V. S. Shirley, Eds., John Wiley and Sons., 1978.

VIN82 Vincent, C. H., NIMS **203**, 307 (1982).
"The Estimation of Differential Counting Measurements of Positive Quantities with Relatively Large Statistical Errors."

WEI75 Weiffenbach, C., S. C. Gujrathi, and J. K. P. Lee, Can. J. Phys. **53**, 101 (1975).
"The Decay of ^{95R}Rh to levels of ^{95R}Ru."

WOO80 Wood, J. L., *Proceedings of the Conference on Future Directions in Studies of Nuclei Far from Stability, Nashville*, **37** (1979).
"The Use of Systematics in the Interpretation of Nuclear Structure Far from the Beta-Stable Region

ZEN78 Zendel, M., Thesis, Johannes Gutenberg Universität, Mainz.
"Entwicklung von schnellen, kontinuierlichen, chemischen Trennerverfahren in der Gasphase fur Spaltproduct."

ZGA80 Zgangar, E. F., *Proceedings of the Conference on Future Directions in Studies of Nuclei Far from Stability, Nashville*, **49** (1979).
"The Structure of Neutron Deficient Odd-Proton Nuclei Near the Shell Closure at Z=82.

Acknowledgments

I would like to thank all of the people who contributed to my thesis. In a project of this scope one person could not do it alone. The following people made special contributions to this thesis. Discussions with the late P. C. Stevenson on nuclear chemistry were instrumental in the final form of AUTOBATCH. R. A. Meyer had the concept that nuclear chemistry could compete with isotope separation, and I also thank him for his continued support throughout my thesis project. Discussions with E. A. Henry greatly enlarged my understanding of gamma-ray spectroscopy. R. P. Yaffe for introducing me to radio chemistry and showing me the discipline necessary for completing this thesis. For facilities and financial support, I am grateful to C. Gatrousis of the Nuclear Chemistry Division of Lawrence Livermore National Laboratory and to G. L. Struble head of the Nuclear Properties Group. I would like to thank S. D. Bloom for introducing me to theoretical nuclear physics and K. Heyde for making the model calculations for ^{83}Se. I greatly appreciate the long hours worked by the reactor personnel which made this experiment possible. Finally, I must thank H. S. Chesnutt for his indispensable help in turning the AUTOBATCH concept into reality.